

POLITECNICO DI MILANO  
SCUOLA DI INGEGNERIA INDUSTRIALE E DELL'INFORMAZIONE  
LAUREA MAGISTRALE IN INGEGNERIA MATEMATICA



# Development of a 3D-Solver Oriented to Numerical Simulations for Semiconductor Devices

Relatore: Prof. Riccardo SACCO  
Correlatore: Dott. Aurelio MAURI

Tesi di Laurea di:  
Andrea BORTOLOSSI  
Matr. n. 783023

Anno Accademico 2013–2014



# Contents

<b>Introduction</b>	<b>ix</b>
<b>1 Semiconductor model</b>	<b>1</b>
1.1 Basic Device Physics . . . . .	1
1.1.1 Intrinsic semiconductor . . . . .	1
1.1.2 Extrinsic semiconductor . . . . .	4
1.1.3 Densities at nonequilibrium condition . . . . .	6
1.1.4 Carrier transport in semiconductor . . . . .	7
1.2 Drift Diffusion Model for semiconductor . . . . .	10
1.2.1 Drift Diffusion formulation . . . . .	10
1.2.2 Generation and Recombination phenomenon . . . . .	13
1.2.3 Mobility models . . . . .	17
<b>2 Resolution of the system</b>	<b>21</b>
2.1 Geometry and boundary conditions . . . . .	21
2.2 Iteration algorithms . . . . .	24
2.2.1 Abstract Newton's method . . . . .	25
2.2.2 Fully coupled Newton's method . . . . .	27
2.2.3 Gummel map algorithm . . . . .	27
<b>3 Finite element discretization</b>	<b>33</b>
3.1 Non Linear Poisson Equation weak form . . . . .	33
3.2 Continuity Equations weak form . . . . .	35
3.3 Numerical approximation . . . . .	36
3.3.1 Geometrical discretization . . . . .	37
3.3.2 Linearized Non Linear Poisson equation . . . . .	38
3.3.3 Continuity equations . . . . .	42
<b>4 Simulation results</b>	<b>47</b>
4.1 Test cases . . . . .	47
4.1.1 p-n junction . . . . .	47

4.1.2	p-n junction in oxide . . . . .	54
4.1.3	MOSFET n-channel . . . . .	60
4.2	Calculation of the current at contacts . . . . .	68
4.2.1	Results . . . . .	71
<b>5</b>	<b>The current calculation problem</b>	<b>83</b>
5.1	Standard approaches . . . . .	84
5.2	Modified approaches . . . . .	86
5.3	Scharfetter-Gummel formula . . . . .	86
5.4	Extension for the 3D case . . . . .	88
	<b>Conclusions and future work</b>	<b>91</b>
	<b>Bibliografia</b>	<b>91</b>
	<b>Ringraziamenti</b>	<b>95</b>

# List of Figures

1.1	Two typical examples of state density occupation ( $g(E)$ ) and probability distribution ( $f(E)$ ). . . . .	2
1.2	Construction of the band diagram. . . . .	4
1.3	Band diagrams of extrinsic silicon. . . . .	6
2.1	(a) Mos device with net dopant concentration distributed according to a gaussian profile and $\Gamma_D$ colored in black. The oxide layer is colored in light blue. (b) Outline of the Mos device with $\Gamma_{int}$ in light gray. . . . .	22
2.2	Gummel map algorithm . . . . .	30
3.1	(a) Number of iteration against residual for different voltages in a diode test case. (b) Magnitude of the damping parameter $t_k$ . . . . .	41
3.2	Evaluation of the Zikatanov condition over a simple partition. Red elements doesn't satisfy condition (3.48) over four edges while blue elements fully accomplished the criterion. . . . .	46
4.1	p-n junction. . . . .	48
4.2	1D plots of the solutions and the quasi fermi potential levels along the line parallel to the Z-axis and placed at the center of the device. On the left is presented the test case at $V_A = 0.3[V]$ while on the right at $V_A = 1.0[V]$ .. . . .	49
4.3	p-n junction 0.3[V] - Potential. . . . .	50
4.4	p-n junction 0.3[V] - Electron density. . . . .	50
4.5	p-n junction 0.3[V] - Hole density. . . . .	50
4.6	p-n junction 1.0[V] - Potential. . . . .	51
4.7	p-n junction 1.0[V] - Electron density. . . . .	51
4.8	p-n junction 1.0[V] - Hole density. . . . .	51
4.9	Total time Gummel Map. . . . .	52
4.10	Time NLP and DD, iteration GM. . . . .	53

4.11	Initial step for different bias. . . . .	53
4.12	Test case p-n junction in oxide. . . . .	54
4.13	Plots of the solutions and the quasi fermi potential levels along the line parallel to the Z-axis and placed at the center of the device. On the left is presented the test case at $V_A = 0.3[V]$ while on the left at $V_A = 1.0[V]$ . . . . .	55
4.14	p-n junction in oxide 0.3[V] - Potential. . . . .	56
4.15	p-n junction in oxide 0.3[V] - Electron density. . . . .	56
4.16	p-n junction in oxide 0.3[V] - Hole density. . . . .	56
4.17	p-n junction in oxide 1.0[V] - Potential. . . . .	57
4.18	p-n junction in oxide 1.0[V] - Electron density. . . . .	57
4.19	p-n junction in oxide 1.0[V] - Hole density. . . . .	57
4.20	Test case dide p-n in oxide 0.3[V] - Electric field. . . . .	58
4.21	$E_y$ along a line parallel to Y-axis, $z = 0.22[\mu m]$ and $x = 0.1[\mu m]$ . . . . .	59
4.22	Geometry of the test case MOS n-channel. . . . .	60
4.23	Energy band levels for nMOSFET along channel. . . . .	61
4.24	Channel of the nMOSFET. . . . .	62
4.25	Electric field density - $V_G = 2.0[V]$ . . . . .	62
4.26	Electrostatic potential - $V_G = 0.0[V]$ . . . . .	63
4.27	Electron density - $V_G = 0.0[V]$ . . . . .	63
4.28	Electron density - $V_G = 0.0[V]$ . . . . .	63
4.29	Electrostatic potential - $V_G = 2.0[V]$ . . . . .	64
4.30	Electron density - $V_G = 2.0[V]$ . . . . .	64
4.31	Electron density - $V_G = 2.0[V]$ . . . . .	64
4.32	Negative carriers for the electron density solution. . . . .	66
4.33	Electron density with finer mesh. . . . .	66
4.34	Satisfaction of the Zikatanov condition. . . . .	66
4.35	Electrostatic potential - Inverse polarization. . . . .	67
4.36	Hole density - Inverse polarization. . . . .	67
4.37	Diode characteristic. . . . .	71
4.38	SRH and Auger RG contribution. . . . .	72
4.39	Current at contact p-n in oxide - Direct polarization. . . . .	73
4.40	pMOSFET. . . . .	74
4.41	$I_D - V_G$ nMOSFET characteristic - mobility models. . . . .	75
4.42	$I_S - V_G$ pMOSFET characteristic - mobility models. . . . .	76
4.43	$I_D - V_G$ nMOSFET. . . . .	78
4.44	$I_S - V_G$ pMOSFET. . . . .	78
4.45	pMOSFET mesh. . . . .	79
4.46	Contribution of the impact ionization with the Van Over- straeten - de Man model inside the pMOSFET $V_S = 1.2[V]$ . . . . .	80

4.47	Contribution of the impact ionization with the Van Over- straeten - de Man model inside the nMOSFET $V_D = 0.5[V]$ . . .	81
4.48	Inverse polarization of the nMOSFET. . . . .	81
4.49	Contribution of the impact ionization with the Van Over- straeten - de Man model inside the pMOSFET $V_S = 0.5[V]$ . . .	82
4.50	Inverse polarization of the pMOSFET. . . . .	82
5.1	Electron current density $V_{gate} = 2.0 [V]$ . . . . .	90





# List of Tables

1.1	List of parameters for the electron and hole mobility models including scattering from lattice thermal vibrations. . . . .	14
1.2	List of parameters for the electron and hole Auger generation/recombination model. . . . .	15
1.3	List of parameters of the electron and hole of van Overstraeten-de Man model . . . . .	16
1.4	List of parameters for the electron and hole mobility models including scattering from lattice thermal vibrations . . . . .	17
1.5	List of parameters in the electron and hole mobility models including scattering from ionized dopant impurities. . . . .	18
1.6	List of parameters for the electron and hole mobility models including scattering from velocity saturation. . . . .	19
4.1	p-n junction - list of settings, parameters and models. . . . .	49
4.2	List of parameters. . . . .	54
4.3	List of parameters. . . . .	61
4.4	List of parameters. . . . .	65
4.5	List of parameters. . . . .	71
4.6	List of parameters. . . . .	73
4.7	List of parameters for nMOSFET. . . . .	75
4.8	List of parameters for pMOSFET. . . . .	76
4.9	List of parameters - nMOSFET. . . . .	77
4.10	List of parameters - pMOSFET. . . . .	77
4.11	List of parameters - nMOSFET. . . . .	81
4.12	List of parameters - pMOSFET. . . . .	82



# Introduction

In 1947 John Bardeen, William Shockley and Walter Brattain (three scientists of Bell Telephone Labs) invented the bipolar transistor and since that crucial point there has been a growth of the semiconductor industry never known before, with serious impact on the way people work and live today.

Before reach the functionality and the miniaturization of modern devices, some fundamental steps has been made. In 1958 the first integrated circuits (IC) was produced, followed by the introduction of the first MOSFET(1960) and CMOS(1963). Into these inventions the first micro-processor(1971) sank his roots and since that time until present, an ever-increasing progress has continued, according to the indication of *Moore's Law* (formulated by Gordon Moore in 1965).

These events led microelectronic industry at the doors of the VLSI era (Very-Large-Scale-Integration). Indeed in the last thirty years the benefits of miniaturization have been the key in the evolutionary progress leading to today's computers, wireless units, and communication systems that offer superior performance, dramatically reduced cost per function, and much reduced physical size.

The large worldwide investment in VLSI technology constitutes a formidable driving force that guarantee the continued progress in IC integration density and speed, for as long as physical principles will allow.

From this point we want start and remark that the aim of numerical simulations is the comprehension of the physical phenomenon which lies behind the function of modern device.

Even if many commercial software are able to resolve different physic situations, they are often specialized on precise physic branch: obviously this strategic choice guarantees more efficiency but it implies a lost in generality. The consequence is that the work of the model analyst became harder when he have to afford problems located in the middle of different phenomenon.

Consider, as example, the functionality of a new device, which its electric behaviour is strong influeced by its mechanical response. Basically you are interested to the resolution of Maxwell's law (which is well performed by SDE-

VICE simulator) and the Navier-Lamè equations (which is well performed by COMSOL simulator). Now the question is: how to put in communication the different outputs? Take into account that it's not possible known precisely how the above programs resolves the equations, which implies a relevant risk when you decide to combine the solutions. In other words the development of an own code is at least desirable and possibly helpful: the main advantage is the total control on simulation procedure and the possibility of fully customize, the major drawback is that the improvement of a personal code needs time and human resources, which in many cases are not available.

The FEMOS project (*Finite Element Method Oriented Solver*) tries to overcome the above limitations. Even if modern devices present innovative and unexpected behaviour, we can't avoid the treatment of the classical semiconductor devices from the simulation possibilities of FEMOS. This thesis found its origin in the development of this achievement, but subjects cover a spread wide area in terms of models and kind of devices. Therefore this work intends to effort some specific points in order to give the basic support and tools to improve then more models and features.

In the first chapter we recall briefly the semiconductor material properties providing necessary informations about physical behaviours and relations between the fundamental quantity (e.g. electrostatic potential, electric field, carrier densities and current densities). Finally, we arrive at the classical Drift-Diffusion model for semiconductor and present several physical models about carrier mobility and generation/recombination phenomena.

The second chapter consists of two main sections. The first one present the geometry framework where we operate and introduce some useful notations. In the second one is exposed the algorithm used in order to effort the equations treated in the first chapter: we chose a decoupled Gummel map approach.

In the third chapter are treated the well-posedness analysis and the numerical approximation of the equations.

The fourth chapter contains the results of the performed simulations. The validation tests are accomplished comparing the results obtained with the FEMOS code with a commercial code (SDEVICE). Moreover we deal with the delicate issue of the calculation of the current at contacts over several semiconductor devices, extending to the 3D case the *residual method* [GS74].

In the fifth chapter **capitolo ancora in fase di costruzione**.

# Chapter 1

## Semiconductor model

In this chapter we shall present the basic physical properties of semiconductor material accordingly with the quantum mechanics theory [YT09]. The Drift-Diffusion model is then presented.

### 1.1 Basic Device Physics

This section covers the basic concepts of semiconductor device physics. As the most used material in the fabrication of VLSI devices is silicon, in the follow we will focus on it.

#### 1.1.1 Intrinsic semiconductor

In a silicon crystal each atom has four valence electrons to share with its four nearest neighboring atoms. The valence electrons are shared in a paired configuration called a covalent bond. The most important result of the application of quantum mechanics to the description of electrons in a solid is that the allowed energy levels of electrons are grouped into bands. The bands are separated by regions of energy that the electrons in the solid cannot possess: forbidden gaps. The highest energy band that is completely filled by electron at 0[K] is called the *valence band* ( $E_V$ ). The next higher energy band, separated by a forbidden gap from the valence band, is called the *conduction band* ( $E_C$ ).

Because in silicon the band gap is on the order of 1 [eV], at room temperature a small fraction of the electrons are excited into the conduction band, leaving behind vacancies (called *holes*) in the valence band. In contrast, an insulator has a much larger forbidden gap making room-temperature conduction virtually impossible, while metals have partially filled conduction bands

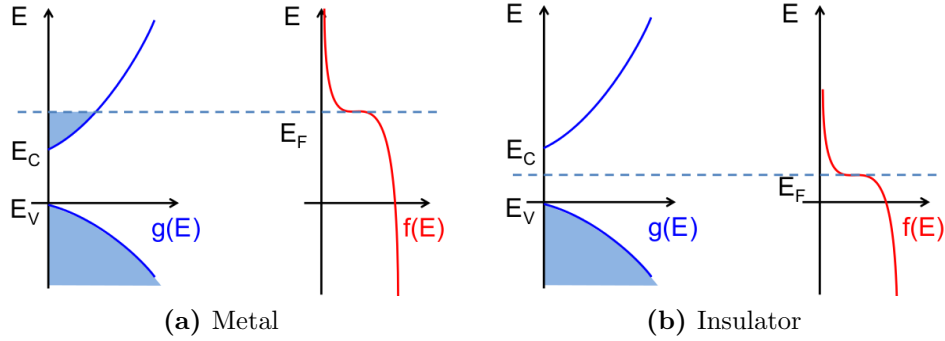


**Figure 1.1:** Two typical examples of state density occupation ( $g(E)$ ) and probability distribution ( $f(E)$ ).

even at absolute zero temperature, this make them good conductors at any temperature.

A suitable formulation of the carrier concentration is given, for electrons, by the follow integral:

$$n = \int_{E_c}^{\infty} g(E)f(E) dE \quad (1.1)$$

With  $g(E)dE$  we indicate the number of electronic states per unit volume with an energy between  $E$  and  $E + dE$  in the conduction band and  $f(E)$  is a suitable probability distribution.

The energy distribution of electrons in a solid is governed by the laws of Fermi-Dirac statistics. For a system in thermal equilibrium, the principal result of these statistics is the *Fermi-Dirac distribution function*, which gives the probability that an electronic state at energy  $E$  is occupied by an electron,

$$f_D(E) = \frac{1}{1 + \exp\left(\frac{E - E_f}{k_B T}\right)} \quad (1.2)$$

here  $k_B = 1.38 \times 10^{-23} [J/K]$  is Boltzmann's constant,  $T$  is the absolute temperature and  $E_f$  is the *Fermi level*.

**Definition 1.1.** The Fermi level ( $E_f$ ) is the energy at which the probability of occupation of an energy state by an electron is exactly one-half.

In most cases when the energy is at least several  $k_B T$  above or below the Fermi level, equation (1.2) can be approximated with the Maxwell-Boltzmann statistics for classical particles, which reads as follows:

$$f_D(E) \simeq f_{MB}(E) = \begin{cases} \exp\left(-\frac{E - E_f}{KT}\right) & E \gg E_f \\ 1 - \exp\left(-\frac{E_f - E}{KT}\right) & E \ll E_f \end{cases} \quad (1.3)$$

Fermi level plays an essential role in characterizing the equilibrium state of a system, it is important to keep in mind the sequent observation.

*Observation 1.1.* When two systems are in thermal equilibrium with no current flow between them, their Fermi levels must be equal, in other words for a continuous region of metals and/or semiconductors in contact, the Fermi level at thermal equilibrium is flat (spatially constant throughout the region).

In general (1.1) is a Fermi integral of the order  $1/2$  and must be evaluated numerically. In the case of non-degenerate semiconductor, Fermi levels stay at least  $3KT/q$  below the edge of the conduction band (for holes we consider the same approximation above the valence band). The Fermi-Dirac distribution can be approximated by the Maxwell-Boltzmann distribution and (1.1) can be solved in the analytically way, obtaining,

$$n = N_c \exp\left(-\frac{E_c - E_f}{KT}\right) \quad (1.4)$$

$$p = N_v \exp\left(-\frac{E_f - E_v}{KT}\right) \quad (1.5)$$

where  $N_c$  and  $N_v$  are the *effective density of states*. In intrinsic semiconductor  $n = p$  and the *intrinsic Fermi level*  $E_i$  can be calculated using equations (1.4) and (1.5) as:

$$E_i = E_f = \frac{E_c + E_v}{2} - \frac{KT}{2} \ln\left(\frac{N_c}{N_v}\right) \quad (1.6)$$

By replacing (1.6) in (1.4) we have the expression of the intrinsic carrier concentration  $n_i = n = p$ :

$$n_i = \sqrt{N_c N_v} \exp\left(-\frac{E_g}{2KT}\right) \quad (1.7)$$

*Observation 1.2.* Since the thermal energy,  $k_B T$  is much smaller than the usual semiconductor bandgap  $E_g$ , the intrinsic Fermi level is very close to the midpoint between the conduction band and the valence band.

Equations (1.4) and (1.5) can be rewritten in terms of the intrinsic carrier density ( $n_i$ ) and energy ( $E_i$ ):

$$n = n_i \exp\left(\frac{E_f - E_i}{KT}\right) \quad (1.8)$$

$$p = n_i \exp\left(\frac{E_i - E_f}{KT}\right) \quad (1.9)$$

Finally we remark a fundamental and useful relation holds at the thermal equilibrium

$$np = n_i^2 \quad (1.10)$$

this relation is usually note as *mass action law*.

One of the most used graphical tool for the anlysis of the functionality of devices is the band diagram Fig.1.2, which summarizes the informations presented above.

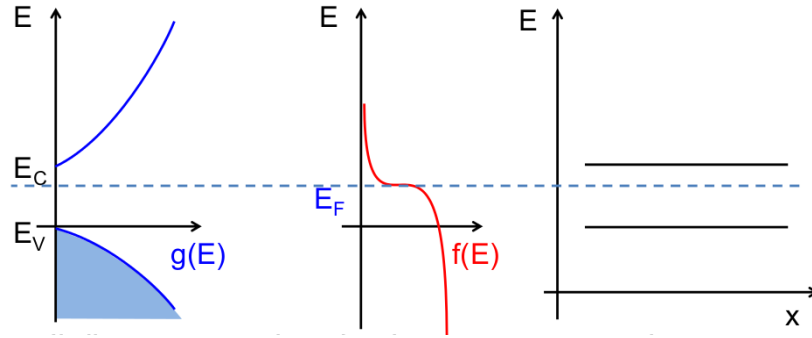


**Figure 1.2:** Construction of the band diagram.

### 1.1.2 Extrinsic semiconductor

At room temperature intrinsic semiconductor has an extremely low free-carrier concentration, therefore, its resistivity is very high. In order to make semiconductor a better conductor it's usual add impurities atoms which introduce additional energy levels in the forbidden gap: these impurities are easily ionized adding either electrons to the conduction band or holes to the valence band. Here the electrical conductivity is dominated by the type and concentration of the impurity atoms.

In the case of silicon two are the types of impurities which are electrically active: those from column V such as arsenic or phosphorus, and those from column III such as boron or indium.



A column-V atom in a silicon lattice tends to have one extra electron loosely bonded after forming covalent bonds with other silicon atoms. In most cases, the thermal energy at room temperature is sufficient to ionize the impurity atom and free the extra electron to the conduction band. Such type of impurities are called *donors*; they become positively charged when ionized. Silicon material doped with column-V impurities or donors is called *n-type* silicon.

A column-III impurity atom in a silicon lattice tends to be deficient by one electron when forming covalent bonds with other silicon atoms. Such an impurity atom can also be ionized by accepting an electron from the valence band, which leaves a free-moving hole that contributes to electrical conduction. These impurities are called *acceptors*: they become negatively charged when ionized. Silicon material doped with column-III impurities or acceptors is called *p-type* silicon.

A p-type or an n-type is named as *extrinsic* silicon. In terms of the energy-band diagrams, donors add allowed electron states in the bandgap close to the conduction-band edge, while acceptors add allowed states just above the valence-band edge.

In contrast to intrinsic silicon, the Fermi level in an extrinsic silicon is not located at the midgap. The Fermi level in n-type silicon moves up towards the conduction band while in p-type silicon moves down towards the valence band. The exact position of the Fermi level depends on both the ionization energy and the concentration of dopants. For example, for an n-type material with a donor impurity concentration,  $N_d$ , the charge neutrality condition requires that

$$n = N_d^+ + p \quad (1.11)$$

where  $N_d^+$  is the density of ionized donors. Similarly for a p-type material with acceptor impurity concentration  $N_a$  we have

$$p = N_a^- + n \quad (1.12)$$

For the sake of simplicity we consider in this work that at room temperature all impurities are ionized ( $N_d = N_d^+$  and  $N_a = N_a^-$ ). Typically the magnitude of impurities is between  $10^{16} \div 10^{20} [cm^{-3}]$ , while the usual intrinsic carrier concentration is almost  $10^{10} [cm^{-3}]$ , for this reason we can approximate the equilibrium densities concentration:

$$\begin{aligned} n &\simeq N_d & p &\simeq \frac{n_i^2}{N_d} \\ p &\simeq N_a & n &\simeq \frac{n_i^2}{N_a} \end{aligned} \quad (1.13)$$

Take into account this approximation and substituting (1.4) and (1.5) in (1.11) and (1.12), solving the algebraic equation have

$$E_c - E_f = KT \ln \left( \frac{N_c}{N_d} \right) \quad (1.14)$$

$$E_f - E_v = KT \ln \left( \frac{N_v}{N_a} \right) \quad (1.15)$$

Equation (1.10) is independent of the dopant type and Fermi level position. Instead of using  $N_c$ ,  $N_v$  and referring to  $E_c$  and  $E_v$  equation (1.14) and (1.15) can be written in a more useful form in terms of  $n_i$  and  $E_i$  defined by equations (1.7) and (1.6):

$$E_f - E_i = KT \ln \left( \frac{N_d}{n_i} \right) \quad (1.16)$$

$$E_i - E_f = KT \ln \left( \frac{N_a}{n_i} \right) \quad (1.17)$$

*Observation 1.3.* The distance between the Fermi level and the intrinsic Fermi level near the midgap is a logarithmic function of doping concentration.

The main consequence of the observation is that densities are related with potential by high non linear relations.

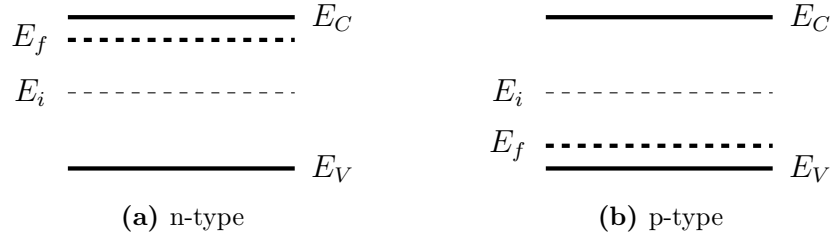


**Figure 1.3:** Band diagrams of intrinsic silicon.

### 1.1.3 Densities at nonequilibrium condition

In VLSI device operation a nonequilibrium situations is often possible: the densities of one or both types of carriers depart from their equilibrium values given by (1.8) and (1.9). In particular, the minority carrier concentration can be easily overwhelmed by injection from neighboring regions. Under these circumstances, while the electrons and holes are in local equilibrium with

themselves, they are not in equilibrium with each other. In order to extend the relationship between Fermi level and densities discussed above, we can introduce separate Fermi levels for electrons and holes. They are called *quasi Fermi levels* defined as  $E_{fn}$  and  $E_{fp}$  replacing equation (1.8) and (1.9):

$$n = n_i \exp\left(\frac{E_{fn} - E_i}{k_B T}\right) \quad (1.18)$$

$$p = n_i \exp\left(\frac{E_i - E_{fp}}{k_B T}\right) \quad (1.19)$$

In non equilibrium condition quasi Fermi levels have a similar physical interpretation in terms of the state occupancy as the Fermi level.

*Observation 1.4.* The electron density in the conduction band can be calculated using  $E_{fn}$ , and the hole density in the valence band using  $E_{fp}$ .

### 1.1.4 Carrier transport in semiconductor

Carrier transport or current flow in silicon is driven by two different mechanisms:

- the **drift** of carriers, which is caused by the presence of an electric field;
- the **diffusion** of carriers, which is caused by an electron or hole concentration gradient.

#### Drift current - Ohm's law

When an electric field is applied to a media, the free carriers are accelerated and acquire a drift velocity superimposed upon their random thermal motion.

*Observation 1.5.* The drift velocity of holes ( $h$ ) is in the direction of the applied field, and the drift velocity of electrons ( $e$ ) is opposite to the field.

The velocity of the carriers does not increase indefinitely under field acceleration, since they are scattered frequently and lose their acquired momentum after each collision. During their motion throughout the lattice structure, carriers travel at an average speed defined as

$$\mathbf{v}_d^e = -\frac{q\mathbf{E}\tau_e}{m_e} \quad \mathbf{v}_d^h = +\frac{q\mathbf{E}\tau_h}{m_h} \quad (1.20)$$

where  $q = 1.602e^{-19}[C]$  is the elementary charge,  $\mathbf{E}$  the electric field,  $\tau_\eta$  the average time of flight of the carrier between two consecutive interactions

with the atoms of the lattice and  $m_\eta$  is the effective mass. The coefficient  $q\tau_\eta/m_\eta$  characterizes how quickly a carrier can move through the lattice and it's well known as carrier mobility [ $m^2V^{-1}s^{-1}$ ]. In general, to include different contributions to the mobility *Matthiessen's rule* is used:

$$\frac{1}{\mu} = \frac{1}{\mu_L} + \frac{1}{\mu_I} + \dots \quad (1.21)$$

where  $\mu_L$  and  $\mu_I$  correspond to the lattice and impurity scattering limited components of mobility (for a more detailed description of mobility models see [YT09]).

Therefore the drift electron, hole, current density, reads as follows:

$$\mathbf{J}_n = -qn\mathbf{v}_d^n = qn\mu_n\mathbf{E} = \sigma_n\mathbf{E} \quad (1.22)$$

$$\mathbf{J}_p = +qp\mathbf{v}_d^p = qp\mu_p\mathbf{E} = \sigma_p\mathbf{E} \quad (1.23)$$

The scalar coefficient  $qn\mu_n(qp\mu_p)$  is often summerized by the electron (hole) conductivity  $\sigma_n(\sigma_p)$ .

Relations (1.22) and (1.23) expresses the well known *Ohm' law* stating that the current density is directly proportional to the applied electric field.

### Diffusion current - Fick's law

In semiconductor devices it's usual have different profiles of dopant in order to allow particular behaviors, this implies a not uniform concentration of carriers which they also diffuse as a result of the concentration gradient. This leads to an additional current contribution accordingly to the *Fick's law*:

$$\mathbf{J}_n = -D_n(-q\nabla n) \quad (1.24)$$

$$\mathbf{J}_p = -D_p(+q\nabla p) \quad (1.25)$$

The proportionally constants  $D_n$  and  $D_p$  are called the electron and hole diffusion coefficients and have units of [ $cm^2s^{-1}$ ]. Physically, both drift and diffusion are closely associated with the random thermal motion of carriers and their collisions with the silicon lattice in thermal equilibrium. A simple relationship between the diffusion coefficient and the mobility is the well known *Einstein relation*:

$$D_\eta = \frac{k_B T}{q} \mu_\eta \quad (1.26)$$

### Drift-Diffusion transport equations

By considering (1.22), (1.23), (1.24) and (1.25), the total electron and hole current densities are:

$$\mathbf{J}_n = qn\mu_n\mathbf{E} + qD_n\nabla n \quad (1.27)$$

$$\mathbf{J}_p = qp\mu_p\mathbf{E} - qD_p\nabla p \quad (1.28)$$

The total conduction current density is  $\mathbf{J} = \mathbf{J}_n + \mathbf{J}_p$ .

We remark that these constitutive laws can be rewritten in two other ways highlighting different physical explanations of the same phenomenon. Moreover these reinterpretations give different start points for the discrete solver algorithm.

Considering that electric field is related to the scalar potential as:

$$\mathbf{E} = -\nabla\varphi \quad (1.29)$$

the current densities can be :

$$\mathbf{J}_n = -qn\mu_n \left( \nabla\varphi - \frac{k_B T}{qn} \nabla n \right) \quad (1.30)$$

$$\mathbf{J}_p = -qp\mu_p \left( \nabla\varphi + \frac{k_B T}{qp} \nabla p \right) \quad (1.31)$$

Considering equations (1.18) and (1.19) the above can be written as:

$$\mathbf{J}_n = -qn\mu_n \nabla\varphi_n \quad (1.32)$$

$$\mathbf{J}_p = -qp\mu_p \nabla\varphi_p \quad (1.33)$$

With these equations we underlying an important aspect which occur in semiconductor material:

*Observation 1.6.* The current density is proportional to the gradient of the quasi Fermi potential.

The third way to represent the current density is based on *Slotboom variables*. In 1973 Jan Slotboom proposed this change in variables for the two-dimensional numerical simulation of a bipolar transistor:

$$u_n = n_i \exp \left( -\frac{\varphi_n}{V_{th}} \right) \quad (1.34)$$

$$u_p = n_i \exp \left( \frac{\varphi_p}{V_{th}} \right) \quad (1.35)$$

where  $V_{th} = k_B T / q$ . Using the above equations into (1.27) and (1.28) we obtain:

$$\mathbf{J}_n = qD_n \exp\left(\frac{\varphi}{V_{th}}\right) \nabla u_n \quad (1.36)$$

$$\mathbf{J}_p = -qD_p \exp\left(-\frac{\varphi}{V_{th}}\right) \nabla u_p \quad (1.37)$$

This interpretation results is:

*Observation 1.7.* The drift-diffusion current density in a semiconductor, is a totally diffusive flux of a new kind of carrier and diffusivity coefficient.

## 1.2 Drift Diffusion Model for semiconductor

Simulations on integrated devices works on several different scale, the *Drift Diffusion model* (DD) is the most widely used mathematical tool for industrial simulation of semiconductor devices. In this section we'll show how is possible to deduce the DD model.

### 1.2.1 Drift Diffusion formulation

The system of Maxwell equations describes the propagation of electromagnetic signal in a medium:

$$\nabla \times \mathbf{H} = \mathbf{J} + \frac{\partial \mathbf{D}}{\partial t} \quad (1.38)$$

$$\nabla \times \mathbf{E} = -\frac{\partial \mathbf{B}}{\partial t} \quad (1.39)$$

$$\nabla \cdot \mathbf{D} = \rho \quad (1.40)$$

$$\nabla \cdot \mathbf{B} = 0 \quad (1.41)$$

we complete the system with the following set of constitutive laws that characterize the electromagnetic properties of the medium:

$$\begin{aligned} \mathbf{D} &= \epsilon \mathbf{E} \\ \mathbf{B} &= \mu_m \mathbf{H} \end{aligned} \quad (1.42)$$

where  $\epsilon$  is the material dielectric permittivity [ $Fcm^{-1}$ ] and  $\mu_m$  is the magnetic permeability [ $Hcm^{-1}$ ]. Since  $\nabla \cdot (\nabla \times \mathbf{A}) = 0$  for any vector  $\mathbf{A}$ ,

(1.41) is satisfied by introducing a vector potential  $\mathbf{A}$  such that  $\mathbf{B} = \nabla \cdot \mathbf{A}$ . We replace it in (1.39) and we obtain

$$\nabla \times \left( \mathbf{E} + \frac{\partial \mathbf{A}}{\partial t} \right) = 0. \quad (1.43)$$

From this we can state that exist a scalar potential  $\varphi$  such that

$$\mathbf{E} + \frac{\partial \mathbf{A}}{\partial t} = -\nabla \varphi \quad (1.44)$$

We multiply (1.44) by  $\epsilon$ , we apply the divergence operator and we obtain using (1.29), (1.42) and (1.40)

$$\rho + \frac{\partial \mathbf{A}}{\partial t} = -\nabla \cdot (\epsilon \nabla \varphi) \quad (1.45)$$

We now assume that  $\frac{\partial \mathbf{A}}{\partial t} = 0$  (quasi static approximation) and we obtain the *Poisson Equation*

$$\nabla \cdot (\epsilon \nabla \varphi) = \rho. \quad (1.46)$$

We apply the divergence operator on the equation [1.38] and we get the *Continuity Equation*

$$\frac{\partial \rho}{\partial t} + \nabla \cdot \mathbf{J} = 0 \quad (1.47)$$

To close the above system we need to specify the mathematical form of the electric charge density ( $\rho$ ) and the electric conduction current density ( $\mathbf{J}$ ). As we introduced in the preview section, devices are usually formed by extrinsic semiconductor and this causes the presence in the lattice of two kind of charge:

- free charge ( $\rho_{free}$ ) (free electron and holes carriers),
- fixed charge ( $\rho_{fixed}$ ) (ionoized dopant impurities).

$$\rho = \underbrace{q(p - n)}_{\rho_{free}} + \underbrace{q(N_D^+ - N_A^-)}_{\rho_{fixed}} \quad (1.48)$$

Notice that we assume  $N_D^+$  and  $N_A^-$  time invariant ( $\partial N_D^+ / \partial t = \partial N_A^- / \partial t = 0$ ).

Accordingly with the preview hypotesis and replacing (1.48), (1.27) and (1.28), we can split the continuity equation into the contribute of electrons and holes, the DD model formulation looks as follows:

$$\left\{ \begin{array}{l} \nabla \cdot (-\epsilon \nabla \varphi) = q(p - n + N_D^+ - N_A^-) \\ -q \frac{\partial n}{\partial t} + \nabla \cdot (-q \mu_n n \nabla \varphi + q D_n \nabla n) = qR \\ q \frac{\partial p}{\partial t} + \nabla \cdot (-q \mu_p p \nabla \varphi - q D_p \nabla p) = -qR \end{array} \right. \quad (1.49)$$

The system is an incompletely parabolic initial value/boundary problem in three scalar unknown dependent variables  $\varphi(\mathbf{x}, t)$ ,  $n(\mathbf{x}, t)$  and  $p(\mathbf{x}, t)$ . Notice that the problem is a nonlinearly coupled system of PDE's, because of the presence of the drift terms ( $n \nabla \varphi$  and  $p \nabla \varphi$ ).

From Maxwell equations we are able to guarantee only that  $\mathbf{J}$  is a solenoidal field, we can't say nothing about the properties of  $\mathbf{J}_n$  and  $\mathbf{J}_p$ . We can interpret  $R(\mathbf{x}, t)$  as the net rate of generation and recombination.

The stationary form can be easily derivate from (1.49) by not considering the temporal derivative.



### 1.2.2 Generation and Recombination phenomenon

The modelling of  $R(\mathbf{x}, t)$  is one of the most important feature due to the important role in determining the current-voltage characteristic of devices.

It's important to keep in mind that electrons and holes are in continuous fluctuation due to their thermal energy, but the macroscopic result of such a process at equilibrium is that the net recombination rate is identically zero at each point and at each time level. Therefore our interest is to analyze the deviations from this condition.

In every moment the system try to maintain the equilibrium, so it's important underlying that the response with a recombination event happens in order to neutralize an excess of charge, while generation event are usually due to thermal agitation or an external input source.

The phenomenological model for the net recombination rate  $R$  is often given by the sequent formulation:

$$R(n, p) = (pn - n_i^2)F(n, p) \quad (1.50)$$

where  $F$  is a function modelling the specific recombination/generation (R/G) event.

In the following we present the classical theory about three kind of contribute.

#### Shockley-Read-Hall recombination (SRH)

Electron and hole generation and recombination can take place directly between the valence band and the conduction band, or indirectly via trap centers in the energy gap (we indicate with  $E_T$  the energy level at where these traps live). The latter category includes Shockley-Read-Hall phenomena (SRH), more precisely SRH rate is a two-particle process which mathematically expresses the probability that:

$R_{SRH}$  an electron in the conduction band neutralizes a hole at the valence band through the mediation of an unoccupied trapping level located in the energy gap,

$G_{SRH}$  an electron is emitted from the valence band to the conduction band, through the mediation of an unoccupied trapping level located in the energy gap.

The following expression is usually employed for the modulating function  $F$ :

$$F_{SRH}(n, p) = \frac{1}{\tau_n \left( p + n_i \cosh \left( \frac{E_T}{k_B T} \right) \right) + \tau_p \left( n + n_i \cosh \left( \frac{E_T}{k_B T} \right) \right)} \quad (1.51)$$

the quantities  $\tau_n$  and  $\tau_p$  are called *carrier lifetimes* and are physically defined as the reciprocals of the capture rates per single carrier associated with the energy trap distribution within the semiconductor energy gap. Their typical order of magnitude lies in the range  $10^{-3} \mu s \div 1 \mu s$ .

Parameter	Unit	Electrons	Holes
$\tau$	s	$1.0 \times 10^{-5}$	$3.0 \times 10^{-6}$
$E_T$	eV	0.0	0.0

**Table 1.1:** List of parameters for the electron and hole mobility models including scattering from lattice thermal vibrations.

### Auger recombination (AU)

Auger R/G is a three-particle process and take place directly between the valence band and the conduction band. We distinguish four cases which depend to the kind of carriers involved in the phenomena:

$R_{AU}^{2n,1p}$  a high-energy electron in the conduction band moves to the valence band where it neutralizes a hole, transmitting the excess energy to another electron in the conduction band;

$G_{AU}^{2n,1p}$  an electron in the valence band moves to the conduction band by taking the energy from a high energy electron in the conduction band and leaves a hole in the valence band;

$R_{AU}^{2p,1n}$  an electron in the conduction band moves to the valence band where it neutralizes a hole, transmitting the excess energy to another hole in the valence band;

$G_{AU}^{2p,1n}$  an electron in the valence band moves to the conduction band by taking the energy from a high energy hole in the valence band and leaves a hole in the valence band.

The following expression is usually employed for the modulating function  $F$ :

$$F_{AU}(n, p) = C_n n + C_p p \quad (1.52)$$

where the quantities  $C_n$  and  $C_p$  are the so called Auger capture coefficients typically of the order of magnitude of  $10^{-25}[cm^6s^{-1}]$ . Note that Auger R/G is relevant only when both carrier densities attain high values.

Parameter	Unit	Magnitude
$C_n$	$cm^6s^{-1}$	$2.9 \times 10^{-31}$
$C_p$	$cm^6s^{-1}$	$1.028 \times 10^{-31}$

**Table 1.2:** List of parameters for the electron and hole Auger generation/recombination model.

### Impact ionization (II)

The impact ionization mechanism is a three-particle generation process and it is dissimilar from the previously phenomenon because we can't express its contribute with a relation like (1.50). The high energy carrier generation is triggered by the presence of very high electric fields. Due to these fields an electron could gains enough energy to excite an electron-hole pair out of a silicon lattice bond. Then the process can be repeated until an avalanche of generated carriers is produced within the region. There are several different models for the II generation, inside our code we implemented the van Overstraeten - de Man model based on the Chynoweth law [Sde13]:

$$G_{II}(n, p) = \alpha_n n |\mathbf{v}_n| + \alpha_p p |\mathbf{v}_p| \quad (1.53)$$

where:

$$\alpha(E_{ava}) = \gamma \exp\left(-\frac{\gamma b}{E_{ava}}\right) \quad (1.54)$$

$$\gamma = \frac{\tanh\left(\frac{\hbar\omega_{op}}{2k_B T_0}\right)}{\tanh\left(\frac{\hbar\omega_{op}}{2k_B T}\right)} \quad (1.55)$$

The factor  $\gamma$  with the optical phonon energy  $\hbar\omega_{op}$  expresses the temperature dependence of the phonon gas against which carriers are accelerated.  $E_{ava}$  is the driving force which takes into account how the electric field influence the generation event. There are two possibilities to compute this quantity:

- compute the component of the electrostatic field in the direction of the current

$$E_{ava}^{n,p} = \frac{\mathbf{E} \cdot \mathbf{J}_{n,p}}{||\mathbf{J}_{n,p}||} \quad (1.56)$$

- consider the module of the quasi fermi gradient

$$E_{ava}^{n,p} = |\nabla \varphi_{n,p}| \quad (1.57)$$

Parameter	Unit	Electrons	Holes	Valid range of electric field
$E_0$	$V\ cm^{-1}$	$4.0 \times 10^5$	$4.0 \times 10^5$	
$a_{high}$	1	$7.03 \times 10^5$	$6.71 \times 10^5$	$E_0$ to $6.0 \times 10^5$
$a_{low}$	1	$7.03 \times 10^5$	$1.582 \times 10^6$	$1.75 \times 10^5$ to $E_0$
$b_{high}$	1	$1.231 \times 10^6$	$1.693 \times 10^6$	$E_0$ to $6.0 \times 10^5$
$b_{low}$	1	$1.231 \times 10^6$	$2.036 \times 10^6$	$1.75 \times 10^5$ to $E_0$
$\hbar\omega_{op}$	eV	0.063	0.063	

**Table 1.3:** List of parameters of the electron and hole of van Overstraeten-de Man model

### 1.2.3 Mobility models

In the following section we illustrate the most commonly used phenomenological models to describe carrier mobilities. More precisely we want describe the several mechanisms that characterize the average time of flight (1.20). Scattering phenomenon slow down the motion of carriers throughout the lattice and the three main physical principles governing these events are:

- interaction with the thermally generated vibrations of the silicon atoms;
- presence of ionized dopant impurities in the crystal;
- reduction to the velocity saturation at high electric fields.

#### Scattering from thermal vibrations

Intuitively, carrier mobility is to be a decreasing function of temperature, as we expect collisions to become more and more frequent as  $T$  gets higher. This idea is commonly represented using a simple power law of the form

$$\mu_\nu^L = \mu_\nu^0 \left( \frac{T}{T_0} \right)^{-\beta_\nu} \quad \nu = n, p \quad (1.58)$$

where  $\mu_\nu^0$  is the low-field mobility,  $\beta_\nu$  are positive numbers and  $T_0$  is a reference temperature typically  $T_0 = 300[K]$ .

Parameter	Unit	Electrons	Holes
$\mu^0$	$cm^2V^{-1}s^{-1}$	1417.0	470.5
$\beta$	1	2.5	2.2

**Table 1.4:** List of parameters for the electron and hole mobility models including scattering from lattice thermal vibrations

#### Scattering from Ionized Impurities

Dopant ionized impurities represent local perturbations of the periodic distribution of silicon atoms. They strongly influence the carrier motion through electrostatic interaction, reducing the mobility of electrons and holes. The model used to simulate doping-dependent mobility in silicon was proposed by *Masetti*:

$$\mu = \mu_{min1} \exp\left(-\frac{P_c}{N_{tot}}\right) + \frac{\mu^L - \mu_{min2}}{1 + \left(\frac{N_{tot}}{C_r}\right)^\alpha} - \frac{\mu_1}{1 + \left(\frac{C_s}{N_{tot}}\right)^\beta} \quad (1.59)$$

where  $N_{tot} = N_D^+ + N_A^-$ ,  $\mu_v^L$  is given by (1.58),  $\mu_{min1}$  and  $\mu_{min2}$  are a positive quantities representing the minimum value of  $\mu$ ,  $P_c$ ,  $C_r$  and  $C_s$  are reference doping values.

Parameter	Unit	Electrons	Holes
$\mu_{min1}$	$cm^2V^{-1}s^{-1}$	52.2	44.9
$\mu_{min2}$	$cm^2V^{-1}s^{-1}$	52.2	0
$\mu_1$	$cm^2V^{-1}s^{-1}$	43.4	29.0
$P_c$	$cm^{-3}$	0	$9.23 \times 10^{16}$
$C_r$	$cm^{-3}$	$9.68 \times 10^{16}$	$2.23 \times 10^{17}$
$C_s$	$cm^{-3}$	$3.43 \times 10^{20}$	$6.10 \times 10^{20}$
$\alpha$	1	0.680	0.719
$\beta$	1	2.0	2.0

**Table 1.5:** List of parameters in the electron and hole mobility models including scattering from ionized dopant impurities.

### Veclocity saturation at high electric field

Under the assumption of low electric field, mobilities are reasonably constant and the carrier drift velocity is proportional to the electric field. As the applied field strength increases, the above assumption is completely wrong as it would predict an unbounded carrier velocity in the material as  $|\mathbf{E}| \rightarrow \infty$ . On the contrary, carrier scattering with lattice phonos produces a limitation to carrier velocity according to the following mathematical expression

$$\lim_{|\vec{E}| \rightarrow \infty} \mu|\mathbf{E}| = v_{sat} \quad (1.60)$$

A common adopted formula is the *Canali model* with temperature dependent parameters

$$\mu = \frac{\mu_L}{\left[1 + \left(\frac{\mu_L |\mathbf{E}|}{v_{sat}}\right)^\beta\right]^{1/\beta}} \quad (1.61)$$

$$v_{sat} = v_0 \exp\left(\frac{300}{T}\right)^{v_{exp}} \quad \beta = \beta_0 \left(\frac{T}{300}\right)^{\beta_{exp}}. \quad (1.62)$$

Parameter	Unit	Electrons	Holes
$v_0$	$cm\ s^{-1}$	$1.07 \times 10^7$	$8.37 \times 10^6$
$v_{exp}$	1	0.87	0.52
$\beta_0$	1	1.109	1.213
$\beta_{exp}$	1	0.66	0.17

**Table 1.6:** List of parameters for the electron and hole mobility models including scattering from velocity saturation.





# Chapter 2

## Resolution of the system

The aim of this chapter is to introduce notation and to present the physical model exposed in the previous chapter, in a more precisely and mathematical form. A briefly overview on the available and used iteration algorithms is then treated.

### 2.1 Geometry and boundary conditions

Consider the stationary form of problem (1.49), in order to proceed we have to close the *Poisson equation* and the *Drift Diffusion equation* for electrons and holes with suitable boundary conditions over the domain.

Let us consider the device domain as the union of two open disjoint subsets,  $\Omega_{Si}$  (doped silicon part), and  $\Omega_{ox}$  (oxide part), such that their intersection  $\partial\Omega_{Si} \cap \partial\Omega_{ox} = \Gamma_{int}$  is the interface. The oxide region  $\Omega_{ox}$  is assumed to be a perfect insulator so that:

$$\begin{aligned} n &= p = 0 \\ \mathbf{J}_n &= \mathbf{J}_p = \mathbf{0} \end{aligned} \tag{2.1}$$

The device boundary  $\partial\Omega$  is divided into two disjoint subsets:  $\partial\Omega_c$  and  $\partial\Omega_a$ . The subset  $\partial\Omega_c$  includes the so called *ohmic contacts*. With ohmic contacts we define every electrical terminal of the device on which the external input voltages are applied. Moreover ohmic contacts are assumed to be *ideal*, they are equipotential surfaces and no voltage drop occurs at the interface between the contact and the neighbouring material. This event is well performed by suitable Dirichlet boundary conditions, therefore in the follow we indicate  $\partial\Omega_c = \Gamma_D$ .

$$\begin{aligned}
\varphi &= \varphi_D \\
n &= n_D \\
p &= p_D
\end{aligned}
\quad \text{on } \Gamma_D. \tag{2.2}$$

In the case where the neighbouring material is a perfect insulator, hypothesis (2.1) takes in place and therefore no Drift-Diffusion equations are solved, this implies that (2.2) reduces to the sole condition on the potential.

Artificial boundaries ( $\partial\Omega_a$ ) are needed in order to obtain a self-contained simulation domain. On these boundaries no electric and current flux is exchanged with the surrounding environment, this fact is well performed by homogeneous Neumann boundary condition ( $\partial\Omega_a = \Gamma_N$ )

$$\begin{aligned}
\mathbf{D} \cdot \mathbf{n} &= 0 \\
\mathbf{J}_n \cdot \mathbf{n} &= 0 \\
\mathbf{J}_p \cdot \mathbf{n} &= 0
\end{aligned}
\quad \text{on } \Gamma_N \tag{2.3}$$

where  $\mathbf{n}$  is the outward unit normal vector defined over  $\partial\Omega$ . As we noted before on  $\partial\Omega_{ox} \cap \Gamma_N$  condition (2.3) reduces to the sole one related with the Poisson equation.

Finally when we solve a Drift-Diffusion equation, if  $\Omega_{ox} \neq \emptyset$  boundary shape could be change. Although the treatment of boundaries doesn't change

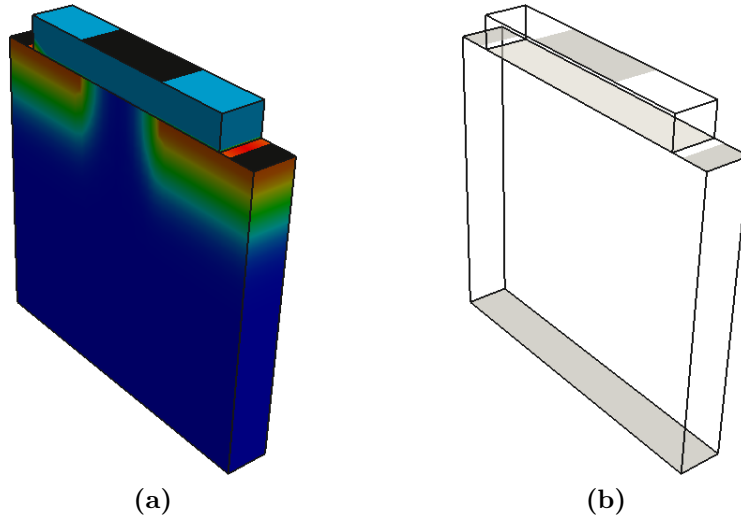


**Figure 2.1:** (a) Mos device with net dopant concentration distributed accordingly to a gaussian profile and  $\Gamma_D$  colored in black. The oxide layer is colored in light blue. (b) Outline of the Mos device with  $\Gamma_{int}$  in light gray.

if you consider the suitable restrictions and extensions

$$\begin{aligned}\Gamma_{D,Si} &= \Gamma_D \cap \partial\Omega_{Si} \\ \Gamma_{N,Si} &= \Gamma_N \cap \partial\Omega_{Si} \cup \Gamma_{int}.\end{aligned}\tag{2.4}$$

In silicon material the ideal condition on contacts is accomplished if both thermodynamical equilibrium and charge neutrality are reached. These two conditions correspond to the following algebraic system for  $n_D$  and  $p_D$

$$\begin{cases} p_D n_D &= n_i^2 \\ p_D - n_D + N_D - N_A &= 0 \end{cases}.\tag{2.5}$$

Solving (2.5) on  $\Gamma_{D,Si}$  we obtain:

$$n_D = \frac{D + \sqrt{D^2 + 4n_i^2}}{2}\tag{2.6}$$

$$p_D = \frac{-D + \sqrt{D^2 + 4n_i^2}}{2}\tag{2.7}$$

where  $D := N_D - N_A$  is the net doping concentration. Furthermore we can approximate that the quasi fermi potential level of silicon at contact is aligned with the external applied voltage. As a consequence we can easily calculate potential condition on  $\Gamma_{D,Si}$  using (1.8) and (1.9)

$$\varphi_D = \varphi_f + V_{th} \ln\left(\frac{n_D}{n_i}\right) = \varphi_f - V_{th} \ln\left(\frac{p_D}{n_i}\right)\tag{2.8}$$

where  $\varphi_f = -E_f/q$  is the unique quasi fermi potential level defined on contacts. When  $\Omega_{ox} \neq \emptyset$  we set  $\varphi_D$  equal to the external applied voltage on  $\Gamma_D/\Gamma_{D,Si}$ .

As we conveyed the boundary conditions, we are able to write in the closed way the stationary form of problem (1.49) as follows:

$$\begin{aligned}-\Delta\epsilon\varphi - q(p - n) &= qD & \text{in } \Omega = \Omega_{ox} \cup \Omega_{Si} \\ \varphi &= \varphi_D & \text{on } \Gamma_D \\ \nabla\varphi \cdot \mathbf{n} &= 0 & \text{on } \Gamma_N \\ \nabla \cdot (q\mu_n n \nabla\varphi - qD_n \nabla n) &= -qR & \text{in } \Omega_{Si} \\ n &= n_D & \text{on } \Gamma_{D,Si} \\ \nabla n \cdot \mathbf{n} &= 0 & \text{on } \Gamma_{N,Si} \\ \nabla \cdot (-q\mu_p p \nabla\varphi - qD_p \nabla p) &= -qR & \text{in } \Omega_{Si} \\ p &= p_D & \text{on } \Gamma_{D,Si} \\ \nabla p \cdot \mathbf{n} &= 0 & \text{on } \Gamma_{N,Si}\end{aligned}\tag{2.9}$$

The high coupled nonlinear nature of system (2.9) makes an analytical treatment very difficult, if not even impossible. For this reason, numerical schemes must be used to compute an approximate solution.

## 2.2 Iteration algorithms

The most used algorithms are *the fully coupled Newton's method* and *the decoupled Gummel map*. First of all we introduce a more compact form of (2.9):

$$\mathbf{F}(\mathbf{U}) = \mathbf{0} \quad (2.10)$$

where:

$$\mathbf{U} := [\varphi, n, p]^T \quad \mathbf{F}(\mathbf{U}) := \begin{bmatrix} F_1(\mathbf{U}) \\ F_2(\mathbf{U}) \\ F_3(\mathbf{U}) \end{bmatrix} \quad (2.11)$$

and having set:

$$\begin{aligned} F_1(\mathbf{U}) &= \nabla \cdot (-\epsilon \nabla \varphi) - q(p - n + D) \\ F_2(\mathbf{U}) &= \nabla \cdot (q\mu_n n \nabla \varphi - qD_n \nabla n) + qR \\ F_3(\mathbf{U}) &= \nabla \cdot (-q\mu_p p \nabla \varphi - qD_p \nabla p) + qR \end{aligned}$$

The non linear problem (2.10) is the abstract generalization of the search of a zero for a real function  $f : \mathbb{R} \rightarrow \mathbb{R}$ . Although the vector function  $\mathbf{F}$  is a nonlinear differential operator and the associated problem which we intend to resolve is: given a functional space  $V$  and the operator  $\mathbf{F} : V \rightarrow V$ , find  $\mathbf{U} \in V$  such that (2.10) is satisfied.

In our application, the function space  $V$  is tipycally a subset of the Sobolev space  $[H^1(\Omega)]^d$  (in this case with  $d$  we intend the number of component of  $\mathbf{F}$ ). Sobolev spaces are based on the space of square integrable functions on  $\Omega$  which reads as follows

$$L^2(\Omega) := \left\{ v : \int_{\Omega} |v|^2 d\Omega = \|v\|_{L^2(\Omega)}^2 < +\infty \right\}. \quad (2.12)$$

The general form of a Sobolev space for an integer  $m \geq 0$  is

$$H^m(\Omega) := \{ v : D^\alpha v \in L^2(\Omega), \forall |\alpha| \leq m \}. \quad (2.13)$$

On this space, we shall use the semi-norm

$$|v|_{m,\Omega}^2 = \sum_{|\alpha|=m} \|D^\alpha v\|_{L^2(\Omega)}^2 \quad (2.14)$$

and the norm

$$\|v\|_{m,\Omega}^2 = \sum_{k \leq m} |D^k v|_{k,\Omega}^2 \quad (2.15)$$

We shall also need to consider functions that vanish on either the entire or a part of the boundary

$$H_0^1 := \{v : v \in H^1(\Omega), v|_{\partial\Omega} = 0\} \quad (2.16)$$

$$H_{0,\Gamma_D}^1 := \{v : v \in H^1(\Omega), v|_{\Gamma_D} = 0\} \quad (2.17)$$

For  $v \in H_0^1(\Omega)$  we have the *Poincaré inequality*

$$|v|_{0,\Omega} \leq C(\Omega)|v|_{1,\Omega} \quad (2.18)$$

and the seminorm  $|\cdot|_\Omega$  is therefore a norm in  $H^1(\Omega)$ , equivalent to  $\|\cdot\|_{1,\Omega}$ .

The above setting of function spaces are used widely in the proceeding of this work, especially during the well-posedness analysis of the equations in chapter 3.

### 2.2.1 Abstract Newton's method

Before introducing the abstract Newton's method we have to define some useful concept.

**Definition 2.1** (Frechét differentiable). Let be  $X$  and  $Y$  two vector spaces. Given  $f, g \in X$  and a functional  $F : X \rightarrow Y$ , the functional  $F$  is Frechét differentiable if it exists a linear bounded operator  $A_f : X \rightarrow Y$  such that:

$$\lim_{\|g\| \rightarrow 0} \frac{\|F(f+g) - F(f) - A_f(g)\|_Y}{\|g\|_X} = 0 \quad (2.19)$$

If the limit exists, we write  $DF(f) = A_f$  and call it the Frechét derivative of  $F$  at  $f$ .

Considering the functional operator (2.11) we can easily compute the relative *Jacobian matrix*  $\mathbf{F}'$ , whose  $(i, j)$  - *th* entry represents the Frechét derivative of the  $i$  - *th* row of the non linear operator with respect to the  $j$  - *th* variable.

$$\mathbf{F}'_{ij}(\mathbf{U})[\mathbf{V}]_j := \lim_{\eta \rightarrow 0} \frac{F_i(\mathbf{U} + \eta[\mathbf{V}]_j) - F_i(\mathbf{U})}{\eta} \quad \mathbf{V} \in V \quad (2.20)$$

where  $[\mathbf{V}]_j \in V$  is the projection of  $\mathbf{V}$  in the  $j$ -th direction.

$\mathbf{F}'_{ij}(\cdot)$  is a linear operator from  $V$  into  $L(V, V)$ , while  $\mathbf{F}'_{ij}(\mathbf{U})$  is the Frechét derivative of the functional  $F_i$  respect the variable  $[\mathbf{U}]_j$ .

Accordingly with the above definitions the abstract Newton's method reads as follows:

#### Newton's method

Let be  $\mathbf{F}$  a function operator, given  $\mathbf{U}^0 \in V$ , for all  $k \geq 0$  until convergence, solve the following linear problem:

$$\begin{aligned} \mathbf{F}'(\mathbf{U}^k)\delta\mathbf{U}^k &= -\mathbf{F}(\mathbf{U}^k) \\ \mathbf{U}^{k+1} &= \mathbf{U}^k + \delta\mathbf{U}^k \end{aligned} \quad (2.21)$$

The application of Newton's method has transformed the original problem (2.10) into the *fixed-point problem* of finding  $\mathbf{U} \in V$  such that

$$\mathbf{U} = T_{\mathbf{F}}(\mathbf{U}) \quad (2.22)$$

where

$$T_{\mathbf{F}}(\mathbf{U}) = \mathbf{F}'(\mathbf{U})^{-1}(\mathbf{F}'(\mathbf{U})\mathbf{U} - \mathbf{F}(\mathbf{U})) \quad (2.23)$$

is the *iteration function* associated with the Newton method. Here we present the main result about the convergence of this method.

**Theorem 2.1.** *Let  $\mathbf{U} \in V$  be a solution of problem (2.10). Assume that  $\mathbf{F}'$  is Lipschitz continuous in the ball  $\mathcal{B}(\mathbf{U}, \delta)$ , i.e., that there exists  $K > 0$  such that:*

$$\|\mathbf{F}'(\mathbf{v}) - \mathbf{F}'(\mathbf{z})\|_{L(V,V)} \leq K\|\mathbf{v} - \mathbf{z}\|_V \quad \forall \mathbf{v}, \mathbf{z} \in \mathcal{B}(\mathbf{U}, \delta), \mathbf{v} \neq \mathbf{z} \quad (2.24)$$

*Then there exists in correspondence  $\delta' > 0$ , with  $\delta' \leq \delta$ , such that for all  $\mathbf{U}^0 \in \mathcal{B}(\mathbf{U}, \delta')$  the sequence  $\{\mathbf{U}^k\}$  generated by (2.21) converges quadratically to  $\mathbf{U}$ , i.e., there exists  $C > 0$  such that, for a suitable  $k_0 \geq 0$  we have:*

$$\|\mathbf{U} - \mathbf{U}^{k+1}\|_V \leq C\|\mathbf{U} - \mathbf{U}^k\|_V^2 \quad \forall k \geq k_0 \quad (2.25)$$

### 2.2.2 Fully coupled Newton's method

If we consider the linearization of the entire system (2.9) the relative Jacobian matrix is a 3x3 matrix and the problem reads as

$$\begin{bmatrix} F_{1,\varphi} & F_{1,n} & F_{1,p} \\ F_{2,\varphi} & F_{2,n} & F_{2,p} \\ F_{3,\varphi} & F_{3,n} & F_{3,p} \end{bmatrix} \begin{bmatrix} \delta\varphi \\ \delta n \\ \delta p \end{bmatrix} = \begin{bmatrix} -F_1(\varphi, n, p) \\ -F_2(\varphi, n, p) \\ -F_3(\varphi, n, p) \end{bmatrix}. \quad (2.26)$$

Every row of the above matrix is a PDE's equation which we can discretize with suitable numerical proceedings (i.e. finite element method). If we spent for example  $N_{dof}$  degrees of freedom to represent  $\delta\varphi$ ,  $\delta n$  and  $\delta p$  we note that the structure of the relative discretized matrix is a 3x3 block matrix system where every block is a  $N_{dof} \times N_{dof}$  matrix:

$$\begin{bmatrix} \mathbf{K}_{1,\varphi} & \mathbf{K}_{1,n} & \mathbf{K}_{1,p} \\ \mathbf{K}_{2,\varphi} & \mathbf{K}_{2,n} & \mathbf{K}_{2,p} \\ \mathbf{K}_{3,\varphi} & \mathbf{K}_{3,n} & \mathbf{K}_{3,p} \end{bmatrix} \begin{bmatrix} \delta\varphi \\ \delta n \\ \delta p \end{bmatrix} = \begin{bmatrix} -\mathbf{F}_1(\varphi, n, p) \\ -\mathbf{F}_2(\varphi, n, p) \\ -\mathbf{F}_3(\varphi, n, p) \end{bmatrix}. \quad (2.27)$$

This implies that at every iteration step we have to solve a linear problem of  $3 \times N_{dof}$  variables.

Moreover to ensure convergence of the Newton iterative process, it is particularly important to provide a very good initial guess vector  $[\varphi_0, n_0, p_0]$ , therefore we have to know for every equation a possibly shape of the solution.

Finally variable in play have different order of magnitude and the jacobian matrix is often quite ill-conditioned and needs appropriate scaling and balancing in order to avoid problems associated with round-off error.

This method is widely used in commercial software especially for the strong result of convergence, although we chose an alternative algorithm known as *Decoupled Gummel Map*.

### 2.2.3 Gummel map algorithm

In 1964 H. K. Gummel proposed an original and alternative iterative algorithm in order to solve the system (2.9) in a semiconductor device in one spatial dimension.

The main idea of the algorithm is to move the nonlinearity to the Poisson equation only, and once obtained the electric potential profile, both continuity equations are linearized. This is possible if we consider the Maxwell-Boltzmann approximation for electrons (1.8) and holes (1.9)

$$F_1(\varphi) = \nabla \cdot (-\epsilon \nabla \varphi) - q(n_i(e^{((\varphi_p - \varphi)/V_{th})} - e^{((\varphi - \varphi_n)/V_{th})}) + D). \quad (2.28)$$

We have decoupled the system and the new algorithm reads as



**Decoupled Gummel map.**

- (Step 0) Give a suitable initial condition for  $\varphi^0$  and set a positive parameter  $toll_{GM} > 0$  (Gummel Map tolerance)
- (Step 1) Fix a positive parameter  $toll_{NLP} > 0$  (Non Linear Poisson tolerance), solve the linearized Non Linear Poisson equation (NLP) in  $\Omega$  using the Newton's method until  $\|F_1(\varphi^{k+1})\| > toll_{NLP}$ :

$$\begin{cases} \nabla \cdot (-\epsilon_{Si} \nabla \delta \varphi^k) + \frac{1}{V_{th}} \sigma_{Si}^k \delta \varphi^k = f_{Si}^k & \text{in } \Omega_{Si} \\ \nabla \cdot (-\epsilon_{ox} \nabla \delta \varphi^k) = f_{ox}^k & \text{in } \Omega_{ox} \\ \delta \varphi^k = 0 & \text{on } \Gamma_D \\ \nabla \delta \varphi^k \cdot \mathbf{n} = 0 & \text{on } \Gamma_N \\ \varphi^{k+1} = \varphi^k + \delta \varphi^k \end{cases} \quad (2.29)$$

having set,

$$\begin{aligned} \sigma_{Si}^k(\varphi^k) &= qn_i \left[ e^{((\varphi_p - \varphi^k)/V_{th})} - e^{((\varphi^k - \varphi_n)/V_{th})} \right] \\ f_{Si}^k(\varphi^k) &= \nabla \cdot (-\epsilon \nabla \varphi^k) + qn_i \left[ e^{((\varphi_p - \varphi^k)/V_{th})} - e^{((\varphi^k - \varphi_n)/V_{th})} + D \right] \\ f_{ox}^k(\varphi^k) &= \nabla \cdot (-\epsilon \nabla \varphi^k) \end{aligned}$$

computed accordingly to the definition of the Frechét derivate.

- (Step 2) Solve the Linear Electron Continuity Equation (LEC):

$$\begin{cases} \nabla \cdot (q\mu_n n \nabla \varphi^i - qD_n \nabla n) = -qR(n^{i-1}, p^{i-1}) & \text{in } \Omega_{Si} \\ n = n_D & \text{on } \Gamma_{D,Si} \\ \nabla n \cdot \mathbf{n} = 0 & \text{on } \Gamma_{N,Si} \end{cases} \quad (2.30)$$

- (Step 3) Solve the Linear Hole Continuity Equation (LHC):

$$\begin{cases} \nabla \cdot (-q\mu_p p \nabla \varphi^i - qD_p \nabla p) = -qR(n^{i-1}, p^{i-1}) & \text{in } \Omega_{Si} \\ p = p_D & \text{on } \Gamma_{D,Si} \\ \nabla p \cdot \mathbf{n} = 0 & \text{on } \Gamma_{N,Si} \end{cases} \quad (2.31)$$

- (Step 4) If  $\max\{\|\varphi^i - \varphi^{i-1}\|_{L^\infty}, \|p^i - p^{i-1}\|_{L^\infty}, \|n^i - n^{i-1}\|_{L^\infty}\} > toll_{GM}$  restart from step (1).

We shall note with  $k$  the iteration step of the inner loop, while with  $i$  the iteration step of the Gummel Map. A concisely scheme is presented in Fig.2.2. Unfortunately there isn't any convergence result for this method like (2.1), although there are several advantages which make Gummel map algorithm preferable to the Fully Coupled Newton's Method. In fact simulations experience shows that the Gummel process is much more insensitive to the choice of the initial guess than Newton's method. This is particularly important in multidimensional problems where it is far from trivial to design a good starting point for initializing.

Another attractive feature is the reduced computational and memory stage cost: at each iteration step the Gummel algorithm requires the successive solution of three problems, each one of size equal to  $N_{dof} \times N_{dof}$ .

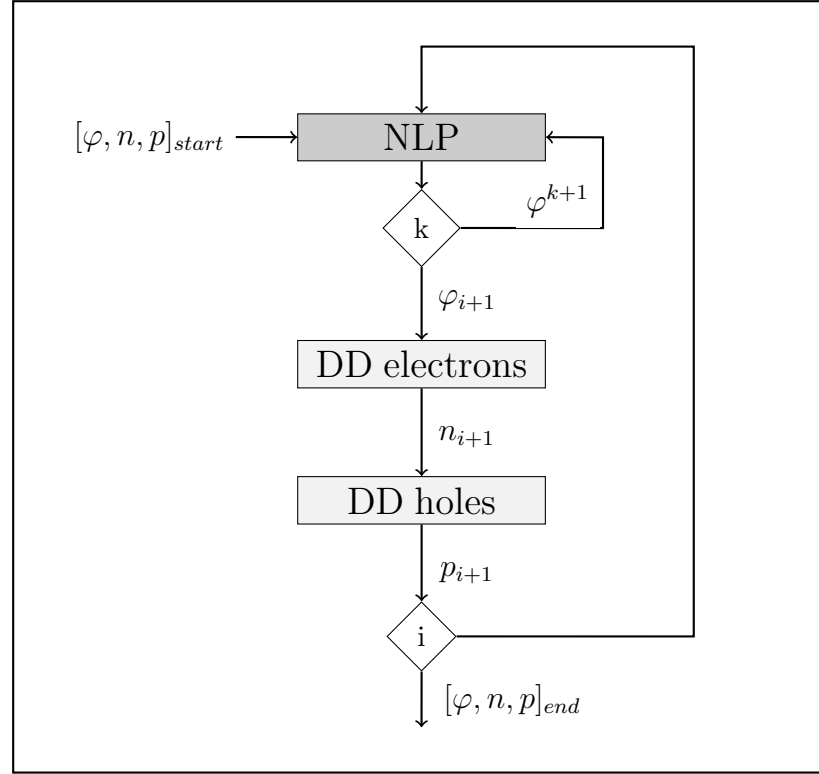


**Figure 2.2:** Gummel map algorithm

We spent some considerations over step 2 and step 3. Accordingly with (1.50) the general R/G phenomenon can be separated in a reaction term and a force term (except for the II which is only a force term contribution). In fact we can denote the general R/G term as follows:

$$\begin{aligned} R_n^{i-1}(n) &= \sigma_n^{i-1}n - f^{i-1} \\ R_p^{i-1}(p) &= \sigma_p^{i-1}p - f^{i-1} \end{aligned} \quad (2.32)$$

where

$$\begin{aligned} \sigma_n &= \frac{p^{i-1}}{F(p^{i-1}, n^{i-1})} & \sigma_p &= \frac{n^{i-1}}{F(p^{i-1}, n^{i-1})} \\ f &= \frac{n_i^2}{F(p^{i-1}, n^{i-1})}. \end{aligned} \quad (2.33)$$

We can rewrite systems (2.30) and (2.31)

$$\begin{cases} \nabla \cdot (q\mu_n n \nabla \varphi^i - qD_n \nabla n) + q\sigma_n^{i-1}n = qf^{i-1} & \text{in } \Omega_{Si} \\ n = n_D & \text{on } \Gamma_{D,Si} \\ \nabla n \cdot \mathbf{n} = 0 & \text{on } \Gamma_{N,Si} \end{cases} \quad (2.34)$$

$$\begin{cases} \nabla \cdot (-q\mu_p p \nabla \varphi^i - qD_p \nabla p) + q\sigma_p^{i-1}p = qf^{i-1} & \text{in } \Omega_{Si} \\ p = p_D & \text{on } \Gamma_{D,Si} \\ \nabla p \cdot \mathbf{n} = 0 & \text{on } \Gamma_{N,Si} \end{cases} \quad (2.35)$$

Systems (2.34) and (2.35) are just a special treatment of the continuity equations in the Gummel Decoupled Algorithm. This splitting of R/G term is called *lagging approach* and corresponds to extending to the non-linear case the classical *Jacobi* method for the iterative solution of linear algebraic systems. Thus equations are sequentially solved, it's possible take advantage of the knowing a solution. Indeed an alternative approach would be use the solution of the first solved equation to compute the R/G contribute in the second equation. In such case the lagging method corresponds to extending to the nonlinear case the classical *Gauss-Seidel* method for the iterative solution in linear algebraic systems.



# Chapter 3

## Finite element discretization

In this section we shall present the classical variational formulation of problems (2.29), (2.34) and (2.35). For each kind of PDE problem we give a briefly presentation of the well-posedness analysis. Finally we describe the finite element discretization.

### 3.1 Non Linear Poisson Equation weak form

Let us write problem (2.29) in a more compact form

$$\left\{ \begin{array}{ll} \nabla \cdot (-\epsilon \nabla \delta \varphi^k) + \sigma^k \delta \varphi^k &= f^k & \text{in } \Omega \\ \delta \varphi^k &= 0 & \text{on } \Gamma_D \\ \nabla \delta \varphi^k \cdot \mathbf{n} &= 0 & \text{on } \Gamma_N \\ \varphi^{k+1} &= \varphi^k + \delta \varphi^k \end{array} \right. \quad (3.1)$$

having set

$$\begin{aligned} \epsilon &= \epsilon_s \mathcal{I}_{\Omega_{Si}} + \epsilon_{ox} \mathcal{I}_{\Omega_{ox}} \\ f &= f_s \mathcal{I}_{\Omega_{Si}} + f_{ox} \mathcal{I}_{\Omega_{ox}} \\ \sigma &= \sigma_s \mathcal{I}_{\Omega_{Si}} \end{aligned}$$

where  $\mathcal{I}_A(\mathbf{x})$  is equal to 1 if  $\mathbf{x} \in A$  and 0 otherwise. System (3.1) constitutes a classical Diffusion-Reaction (DR) problem in  $\Omega$ , respect the variable  $\delta \varphi^k$ . Now we multiply the equation with a test function  $v \in H_{\Gamma_D}^1$  and we integrate over all the domain

$$- \int_{\Omega} \epsilon \Delta \delta \varphi^k v \, d\Omega + \int_{\Omega} \sigma^k \delta \varphi^k v \, d\Omega = \int_{\Omega} f^k v \, d\Omega \quad \forall v \in H_{\Gamma_D}^1(\Omega). \quad (3.2)$$

Applying the Green-formula on (3.2) and then considering the boundary conditions, we get the weak formulation which reads as: find  $\delta\varphi^k \in H_{\Gamma_D}^1(\Omega)$  such that

$$\int_{\Omega} \epsilon \nabla \delta\varphi^k \nabla v \, d\Omega + \int_{\Omega} \sigma^k \delta\varphi^k v \, d\Omega = \int_{\Omega} f^k v \, d\Omega \quad \forall v \in H_{\Gamma_D}^1(\Omega) \quad (3.3)$$

We are able to define the following bilinear form

$$a : H_{\Gamma_D}^1(\Omega) \times H_{\Gamma_D}^1(\Omega) \rightarrow \mathbb{R}, \quad a(u, v) = \int_{\Omega} \epsilon \nabla u \nabla v \, d\Omega + \int_{\Omega} \sigma^k uv \, d\Omega \quad (3.4)$$

and the linear and bounded functional

$$F : H_{\Gamma_D}^1(\Omega) \rightarrow \mathbb{R}, \quad F(v) = \int_{\Omega} f^k v \, d\Omega \quad (3.5)$$

In order to prove the existence and uniqueness of the solution, we apply the *Lax-Millgram theorem* [Sal10] to the weak formulation (3.3). The well-posedness is ensured by several and physical hypotesis:

- $\epsilon \in L^\infty(\Omega)$  and  $\exists m$  s.t.  $0 < m \leq \epsilon$  (a.e.) in  $\Omega$ ;
- $\forall k \geq 0$   $\sigma^k \in L^\infty(\Omega)$  and  $\exists m$  s.t.  $0 < m \leq \sigma^k$  (a.e.) in  $\Omega_{Si}$ .

We define some useful quantities:

$$\begin{aligned} \epsilon_M &= \max_{\Omega} \epsilon & \epsilon_m &= \min_{\Omega} \epsilon \\ \sigma_M &= \max_{\Omega} \sigma & \sigma_m &= \max_{\Omega} \sigma = 0 \end{aligned}$$

Take into account the above hypotesis one can demonstrate:

- **Continuity of the bilinear form,**

$$\forall u, v \in H_{\Gamma_D}^1$$

$$\begin{aligned} \left| \int_{\Omega} \epsilon \nabla u \nabla v + \int_{\Omega} \sigma^k uv \right| &\leq \epsilon_M \|\nabla u\|_{L^2} \|\nabla v\|_{L^2} + \sigma_M \|u\|_{L^2} \|v\|_{L^2} \\ &\leq \max\{\epsilon_M, \sigma_M\} (\|\nabla u\|_{L^2} \|\nabla v\|_{L^2} + \|u\|_{L^2} \|v\|_{L^2}) \\ &\leq \max\{\epsilon_M, \sigma_M\} \|u\|_{H_{\Gamma_D}^1} \|v\|_{H_{\Gamma_D}^1} \end{aligned}$$

- **Coercivity of the bilinear form,**

$$\forall u \in H_{\Gamma_D}^1$$

$$\begin{aligned} \left| \int_{\Omega} \epsilon \nabla u \nabla u + \int_{\Omega} \sigma^k u^2 \right| &\geq \epsilon_m \|\nabla u\|_{L^2}^2 + \sigma_m \|u\|_{L^2}^2 \\ &= \epsilon_m \|\nabla u\|_{L^2}^2 \\ &= \epsilon_m \|\nabla u\|_{H_{\Gamma_D}^1}^2 \end{aligned}$$

- **Continuity of the functional,**

$$|\int_{\Omega} f^k v| \leq \|f^{(k)}\|_{L^2} \|v\|_{L^2} \quad \forall v \in H_{\Gamma_D}^1$$

Then we can state that  $\forall k \geq 0$  there exists a unique solution of the linearized Non Linear Poisson equation.

## 3.2 Continuity Equations weak form

Without loss of generality we can consider only the electron continuity equation. System (2.34) is a classical diffusion-advection-reaction (DAR) problem written in conservative form. With a suitable change of variables we are able to treat these PDE's equations likewise the linearized Non Linear Poisson equation in the previous section. Consider the Slotboom variable (1.34), we can rewrite system (2.34)

$$\begin{cases} \nabla \cdot (-qD_n e^{(\varphi^i/V_{th})} \nabla u_n) + \sigma_n^{i-1} e^{(\varphi^i/V_{th})} u_n = f^{i-1} & \text{in } \Omega_{Si} \\ u_n = n_D e^{(-\varphi^i/V_{th})} & \text{on } \Gamma_{D,Si} \\ \nabla u_n \cdot \mathbf{n} = 0 & \text{on } \Gamma_{N,Si} \end{cases} \quad (3.6)$$

We can easily obtain the weak formulation repeating the same steps made for the linearized Non Linear Poisson problem. Therefore the weak formulation of the Electron Continuity equation is: find  $u_n \in H_{\Gamma_{D,Si}}^1(\Omega)$  such that:

$$\int_{\Omega_{Si}} qD_n e^{(\varphi^i/V_{th})} \nabla u_n \nabla v \, d\Omega + \int_{\Omega_{Si}} \sigma_n^{i-1} e^{(\varphi^i/V_{th})} u_n v \, d\Omega = \int_{\Omega_{Si}} f^{i-1} v \, d\Omega \quad \forall v \in H_{\Gamma_{D,Si}}^1 \quad (3.7)$$

The existence and uniqueness of the unknown variable  $u_n$  ensures the same properties on  $n$ , thanks to the univocal relation between  $u_n$  and  $n$ . We have to make some hypotheses on the coefficients  $\forall i \geq 0$ :

- $qD_n e^{(\varphi^i/V_{th})} \in L^\infty(\Omega_{Si})$  and  $\exists m$  s.t.  $0 < m \leq qD_n e^{(\varphi^i/V_{th})}$  (a.e.) in  $\Omega_{Si}$ ;
- $\sigma_n^{i-1} e^{(\varphi^i/V_{th})} \in L^\infty(\Omega_{Si})$  and  $\exists m$  s.t.  $0 < m \leq \sigma_n^{i-1} e^{(\varphi^i/V_{th})}$  (a.e.) in  $\Omega_{Si}$ .

As we made before, we define the relative bilinear form

$$a(u, v) = \int_{\Omega_{Si}} qD_n e^{(\varphi^i/V_{th})} \nabla u_n \nabla v \, d\Omega + \int_{\Omega_{Si}} \sigma_n^{i-1} e^{(\varphi^i/V_{th})} u_n v \, d\Omega \quad (3.8)$$

and the linear and bounded functional

$$F(v) = \int_{\Omega_{Si}} f^{i-1} v \, d\Omega \quad (3.9)$$

Now the well-posedness of this problem is ensured repeating the same passages showed in the previous section.

### 3.3 Numerical approximation

In this section we shall introduce briefly the classical Galerkin's method for the approximation of a weak formulation on  $\Omega$ . Every weak formulation could be represented in a more compact and generic form as, find  $u \in V$  such that

$$a(u, v) = F(v) \quad \forall v \in V \quad (3.10)$$

where  $V$  is the space of admissible functions, e.g.  $H_{\Gamma_D}^1(\Omega)$ ,  $H_{\Gamma_D, Si}^1(\Omega_{Si})$ . Let us introduce  $V_h$  which it is a family of finite-dimensional subspace of  $V$ , depending by a positive parameter  $h$ , such that

$$V_h \subset V, \quad \dim V_h < \infty \quad \forall h > 0 \quad (3.11)$$

The *Galerkin's problem* reads as, find  $u_h \in V_h$  such that:

$$a(u_h, v_h) = F(v_h) \quad \forall v_h \in V_h \quad (3.12)$$

Let be  $\mathcal{T}_h$ , a finite partition of  $\Omega$ , and  $K$  a generic element of  $\mathcal{T}_h$  such that  $\bar{\Omega} = \bigcup \bar{K}$ . In this case the parameter  $h$  refers to the characteristic dimension of the elements  $K$ . Let us introduce the general finite element spaces of the polynomial element-wise defined functions:

$$X_h^r(\Omega) := \{v_h \in C^0(\bar{\Omega}) : v_h|_K \in \mathbb{P}_r, \forall K \in \mathcal{T}_h\} \quad (3.13)$$

and the relative space where functions vanish on boundaries

$$X_{h, \Gamma_D}^r(\Omega) := \{v_h \in X_h^r : v_h|_{\Gamma_D} = 0\}. \quad (3.14)$$

If  $\Omega \in \mathbb{R}^3$  we have:

$$\dim \mathbb{P}_r := \frac{(r+1)^3}{2} + \frac{(r+1)^2}{2} + \frac{r(r+1)(2r+1)}{12} - \frac{r(r+1)^2}{2} - \frac{r(r+1)}{4} \quad (3.15)$$

More precisely we approximate  $H_{\Gamma_D}^1(\Omega)$  with  $X_{h, \Gamma_D}^1(\Omega)$  and  $H_{\Gamma_D, Si}^1(\Omega_{Si})$  with  $X_{h, \Gamma_D, Si}^1(\Omega_{Si})$ . Therefore accordingly with (3.15) we have



$$\begin{aligned}
\dim \mathbb{P}_1 &= 4 \\
\dim X_h^1 &= N_h \\
\dim X_{h,\Gamma_D}^1 &= N_h - N_g
\end{aligned}$$

where  $N_h$  is the number of vertices of the partition  $\mathcal{T}_h$  and  $N_g$  are the number of vertices lie on Dirichlet boundaries.

We denote by  $\{\psi_j\}_{j=1}^{N_h}$  the Lagrangian basis of the space  $X_h^1$ . Naturally as  $u_h \in X_h^1$  there are  $u_j \in \mathbb{R}$  with  $j = 1, \dots, N_h$  such that:

$$u_h = \sum_{j=1}^{N_h} u_j \psi_j \quad (3.16)$$

Because every functions of  $V_h$  is a linear combination of  $\psi_i$ , we can test equation (3.12) only for each basis function rather than  $\forall v_h \in V_h$ . The result of the complete discretization is find  $u_j$ , with  $j = 1, \dots, N_h$  such that:

$$\sum_{j=1}^{N_h} u_j a(\psi_j, \psi_i) = F(\psi_i) \quad \forall i = 1, \dots, N_h \quad (3.17)$$

In order to implement this routine it's useful make explicit the subdivision of the bilinear form on the element of the partition  $\mathcal{T}_h$ :

$$\sum_{j=1}^{N_h} u_j \sum_{K \in \mathcal{T}_h} a_K(\psi_j, \psi_i) = \sum_{K \in \mathcal{T}_h} F_K(\psi_i) \quad \forall i = 1, \dots, N_h \quad (3.18)$$

### 3.3.1 Geometrical discretization

We set every elements  $K \in \mathcal{T}_h$  as a tetrahedral of volume  $|K|$ ; we suppose that there exists a constant  $\delta > 0$  such that:

$$\frac{h_K}{\rho_K} \leq \delta \quad \forall K \in \mathcal{T}_h \quad (3.19)$$

where  $h_K = \text{diam}(K) = \max_{x,y \in K} |x - y|$  and  $\rho_K$  is the diameter of the sphere inscribed in the tetrahedral  $K$ . Condition (3.19) is the so called *mesh regularity condition* [Qua08] and it ensures an isotropic partition. We denote with  $\mathcal{E}_h$ ,  $\mathcal{V}_h$  and  $\mathcal{F}_h$  the set of all the edges, verteces and faces of  $\mathcal{T}_h$  respectively, and for each  $K \in \mathcal{T}_h$  we denote by  $\partial K$  and  $\mathbf{n}_{\partial K}$  the boundary of the element and its outward unit normal.

### 3.3.2 Linearized Non Linear Poisson equation

As regards the linearized NLP equation we have:

$$a(\psi_j, \psi_i) = \int_{\Omega} \epsilon \nabla \psi_j \nabla \psi_i d\Omega + \int_{\Omega} \sigma^k \psi_j \psi_i d\Omega \quad (3.20)$$

and the relative restriction on the element is

$$a_K(\psi_j, \psi_i) = \int_K \epsilon \nabla \psi_j \nabla \psi_i dK + \int_K \sigma^k \psi_j \psi_i dK \quad (3.21)$$

Equation (3.21) it's formed by two distinct contributions, the former identifies the diffusive contribution and generates the so called *stiffness matrix*, while the latter refers to the reaction and generates the *mass matrix*.

The coefficient  $\epsilon$  is a piece-wise constant function, which changes on different material regions.  $\mathcal{T}_h$  is built such that every  $K$  belongs to a single region, while it is possible that vertices belong to different regions. Therefore  $\epsilon$  is constant over each elements and integral in (3.21) become easier.

As a consequence of choose the discrete space  $X_h^1$ , we can't expect a better priori estimation error on the solution, than the first order in  $\|\cdot\|_{1,\Omega}$  respect the characteristic discretization step  $h_K$  [Qua08]. This implies that is not necessary and useful the use of an high order quadrature, and the trapezoidal rule is enough accurate. The main consequence of using trapezoidal quadrature rule is that extra-diagonal elements of the mass-matrix disappear. This technique is well known as *lumping procedure* applied on the mass-matrix.

Finally we obtain the contributions of the local system matrix  $A_K^k$ :

$$[A_K^k]_{ij} = \epsilon_K L_{ij} + \frac{|K|}{4} \sigma_i^k \quad (3.22)$$

having set

$$\begin{aligned} L_{ij} &\simeq \int_K \nabla \psi_i \nabla \psi_j d\Omega \\ \sigma_i^k &= \sigma^k(\mathbf{x}_i) \end{aligned} \quad (3.23)$$

Here follows the construction of the right hand side, based on the local contribution approximated with trapezoidal rule:

$$[F_K]_i^k = f_i^k |K|/4 \simeq \int_{\Omega} f^k \psi_i d\Omega \quad (3.24)$$

The local contributions of each element  $K$  can be assembled in the global matrix  $A$ : let  $I$  be the global index of a generic vertex belonging to the

partition  $\mathcal{T}_h$ , we denote by  $\mathcal{J}_K : \mathcal{V}_{\mathcal{T}_h} \rightarrow \mathcal{V}_K$  the map which connects  $I$  to its corresponding local index  $i = 1, \dots, 4$  in the element  $K$ . Then we have

$$A_{IJ}^k = \sum_{\substack{\forall K \in \mathcal{T}_h \text{ s.t.} \\ \mathcal{J}_K(I), \mathcal{J}_K(J) \subset \mathcal{V}_K}} [A_K]_{ij}^k \quad (3.25)$$

analogously for the force term  $\mathbf{b}^{(k)}$ :

$$b_I^k = \sum_{\substack{\forall K \in \mathcal{T}_h \text{ s.t.} \\ \mathcal{J}_K(I) \subset \mathcal{V}_K}} [F_K]_i^k \quad (3.26)$$

Once we have built the global matrix  $A^k$  and the global vector  $\mathbf{b}^k$  we need to take into account the essential boundary conditions. In fact the displacement formulation is a primal formulation which forces Dirichlet boundary condition in a strong way. Therefore we have to modify the algebraic system. We choose the *diagonalization* technique which does not alter the matrix pattern nor introduce ill-conditioning for the system. Let  $i_D$  be the generic index of a Dirichlet node, we denote by  $[\delta\varphi_D]_i$  (which in this case is equal to zero) the known value of the solution  $\delta\varphi$  at the node. We consider the Dirichlet condition as an equation of the form  $a[\delta\varphi]_i = a[\delta\varphi_D]_i$ , where  $a \neq 0$  is a suitable coefficient. In order to avoid degrading of the global matrix condition number, we take  $a$  equal to the diagonal element of the matrix at the row  $i_D$ .

Finally we have completed the discretization of (Step 1), which reads as follows:

$$\begin{cases} A^k \delta\varphi^k &= \mathbf{b}^k \\ \varphi^{k+1} &= \varphi^k + \delta\varphi^k \end{cases} \quad (3.27)$$

As every iteration procedure, problem (3.27) needs a suitable convergence break criterion. A good method is based on checking the satisfaction of the fixed point equation (2.10) by the  $k$ -th solution, then the inner loop of the Gummel Map reads as: given a tolerance  $toll > 0$  solve problem (3.27) until:

$$\|\mathbf{b}(\varphi^{k+1})\|_2 > toll \quad (3.28)$$

where  $\|\cdot\|_2$  is the usual Euclidean norm for a vector.

### Damping

Nevertheless the theorem (2.1), the system (3.27) may be affected by difficulties on the convergence velocity. The main problem associated with the

classical Newton method is the tendency to overestimate the length of the present correction step. This phenomenon is frequently termed as *overshoot*. In the case of the semiconductor equations this overshoot problem has often been treated by simply limiting the size of the correction vector ( $\delta\varphi$ ) determined by Newton's method. The usual established modifications to avoid overshoot are given by the follow formulations:

$$\tilde{A}(\varphi_k) = \frac{1}{t_k} A(\varphi_k) \quad (3.29)$$

$t_k$  is a properly chosen positive parameter: for  $t_k = 1$  the modified Newton method reduces to the classical Newton method. We have now to deal with the question how to choose  $t_k$  or  $s_k$  such that the modified Newton method exhibits superior convergence properties compared to the classical Newton method. For the case (3.29) there's a simple criterion suggested by Deuffhard [Deu74].  $t_k$  is taken from the interval  $(0, 1]$  in such a manner that for any norm,

$$\|A(\varphi_k)^{-1} \mathbf{b}(\varphi_k - t_k A(\varphi_k)^{-1} \mathbf{b}(\varphi_k))\| < \|A(\varphi_k)^{-1} \mathbf{b}(\varphi_k)\| \quad (3.30)$$

Condition (3.30) guarantees that the correction of the  $k$ -th iterate is an improved approximation to the final solution, in other words the residual norm can only descents. This condition can be easily evaluated only if the Jacobian matrix is factored into triangular matrices because the evaluation of the argument of the norm on the left hand side of (3.30) is then reduced to a forward and backward substitution and the evaluation of  $\mathbf{b}(\varphi)$ . Although we use an iterative method (BCG solver based on [PTVF07]) which implies serious difficulties to the application of the above criterion. Another valid possibility is to use the main diagonal of  $A(\varphi_k)$ , denoted as  $D(\varphi_k)$ :

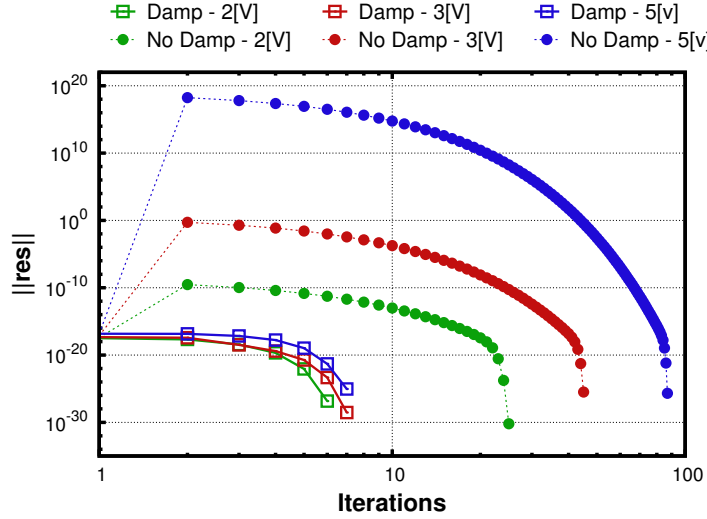
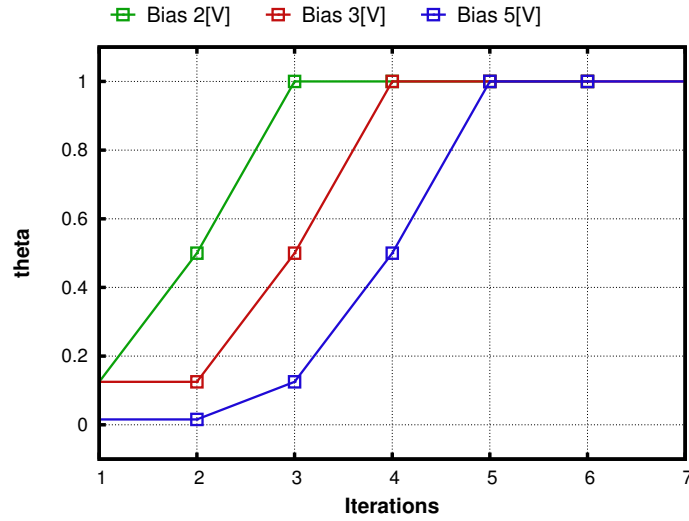
$$\|D(\varphi_k)^{-1} \mathbf{b}(\varphi_k - t_k D(\varphi_k)^{-1} \mathbf{b}(\varphi_k))\| < \|D(\varphi_k)^{-1} \mathbf{b}(\varphi_k)\| \quad (3.31)$$

This is the criterion developed in our code. However the value to use for  $t_k$  is a question of trial and error. Frequently one chooses the following sequences:

$$t_k = \frac{1}{2^i} \quad (3.32)$$

$$t_k = \frac{1}{\frac{i(i+1)}{2} \cdot 2} \quad (3.33)$$

obviously  $i$  is the subiterations of damping reached when satisfied (3.31). Sufficiently close to the solution (3.30) (and so (3.31)) will be satisfied with  $t_k = 1$  so that the convergence properties of the classical Newton method are recovered.

(a) *Non Linear Poisson residual*(b)  $t_k$  parameter.

**Figure 3.1:** (a) Number of iteration against residual for different voltages in a diode test case. (b) Magnitude of the damping parameter  $t_k$ .

### 3.3.3 Continuity equations

As regards the LEC equation we have:

$$a(u, v) = \int_{\Omega_{Si}} q D_n e^{(\varphi^i/V_{th})} \nabla \psi_j \nabla \psi_i d\Omega + \int_{\Omega_{Si}} \sigma_n^{i-1} e^{(\varphi^i/V_{th})} \psi_j \psi_i d\Omega \quad (3.34)$$

Even if this form guarantees an easily analysis of well-posedness, the choice of using Slotboom variables  $u_n$  and  $u_p$  causes the onset of overflow problems due to the evaluation of  $\exp(\varphi/V_{th})$ , which can be a rapidly varying function according to the behaviour of the potential  $\varphi$ .

Therefore special care has to be taken in the treatment of the diffusion coefficient. In view of further discussions of this issue, we introduce some useful notation. For each set  $S \subset \Omega$  having measure  $|S|$ , we introduce the following averages of a given function  $g$  that is integrable on  $S$ :

$$\mathcal{M}_S(g) = \frac{\int_S g dS}{|S|} \quad \mathcal{H}_S = (\mathcal{M}_S(g^{-1}))^{-1}$$

Notice that  $\mathcal{M}_S$  is the usual average, while  $\mathcal{H}_S$  is the *harmonic average*. It is well-known that the use of the harmonic average provides a superior approximation performance than the usual average [IE83].

The weak form (3.34) is the result of a displacement approach which is the most classical way of setting these problems. Although different variational formulations and therefore different finite element approximations may be used, like a primal mixed approach (PM), for a more complete treatment see [DF05]. First of all it's convenient to reformulate problem (2.34) by using the relation (1.34) and (1.36) in a more generic form. This yields the following equivalent form of the strong ADR model problem

$$\begin{cases} \nabla \cdot (\mathbf{J}_n(n)) + \sigma n = f & \text{in } \Omega_{Si} \\ \mathbf{J}_n = q D_n e^{(\varphi/V_{th})} \nabla (e^{(-\varphi/V_{th})} n) & \text{in } \Omega_{Si} \\ n = n_D & \text{on } \Gamma_{D,Si} \\ \mathbf{J}_n \cdot \mathbf{n} = 0 & \text{on } \Gamma_{N,Si} \end{cases} \quad (3.35)$$

We report here the weak formulation of (3.35) which is well investigated in [DF05], find  $\mathbf{J}_n \in [L^2(\Omega)]^d$  and  $n \in H_{\Gamma_{D,Si}}^1(\Omega)$  such that

$$-\int_{\Omega_{Si}} \mathbf{J}_n \cdot \nabla v \, d\Omega + \int_{\Omega_{Si}} \sigma n v \, d\Omega = \int_{\Omega_{Si}} f v \, d\Omega \quad \forall v \in H_{\Gamma_{D, Si}}^1(\Omega) \quad (3.36)$$

$$\int_{\Omega_{Si}} (q D_n e^{(\varphi/V_{th})})^{-1} \mathbf{J}_n \cdot \mathbf{q} \, d\Omega + \int_{\Omega_{Si}} \nabla(e^{(\varphi/V_{th})} n) \cdot \mathbf{q} \, d\Omega = 0 \quad \forall \mathbf{q} \in [L^2(\Omega)]^d \quad (3.37)$$

In order to approximate  $[L^2(\Omega)]^d$  we introduce a new discrete space

$$\Sigma_h := \{\mathbf{q}_h \in [L^2(\Omega)]^d : \mathbf{q}|_K \in [\mathbb{P}_0]^d \forall K \in \mathcal{T}_h\} \quad (3.38)$$

As usual  $d$  is the dimension of  $\Omega$  and if  $d = 3$ ,  $\mathbf{q}_h$  is characterized for every  $K \in \mathcal{T}_h$  by the triplet

$$\mathbf{q}_{1,2,3}^h = \left\{ \begin{bmatrix} 1 \\ 0 \\ 0 \end{bmatrix} \begin{bmatrix} 0 \\ 1 \\ 0 \end{bmatrix} \begin{bmatrix} 0 \\ 0 \\ 1 \end{bmatrix} \right\} \quad (3.39)$$

Therefore we can easily deduced the restriction on a generic element of (3.36) and (3.37) and write the relative discretized bilinear form

$$\begin{cases} a_h^K(n_h, v_h) &= \int_K \mathbf{J}_{n,h}^K(n_h) \nabla v_h \, dK + \int_K \sigma n_h v_h \, dK \\ F(v_h)^K &= \int_K f v_h \, dK \\ \mathbf{J}_{n,h}^K &= D_K(q D_n e^{(\varphi/V_{th})}) \nabla(e^{(-\varphi/V_{th})} n_h) \end{cases} \quad (3.40)$$

where  $D_K \in \mathbb{R}^{3 \times 3}$  is the element stiffness matrix. Several treatments may be performed on this matrix

$$D_K(q D_n e^{(\varphi/V_{th})}) = \begin{cases} \mathcal{M}_K(q D_n e^{(\varphi/V_{th})}) \\ \mathcal{H}_K(q D_n e^{(\varphi/V_{th})}) \\ \frac{1}{|K|} \sum_{i=1}^6 \mathcal{H}_{e_i}(q D_n e^{(\varphi/V_{th})}) |e_i| s_i \mathbf{t}_i \mathbf{t}_i^T \end{cases} \quad (3.41)$$

Occorre aprire un discorso più ampio? Descrizione degli elementi geometrici 3D? Il significato di  $s_i$  in 3D a quanto pare è complesso.

These different approaches in the computation of the average of the diffusion coefficient are responsible for the quite different numerical performance

of the relative methods. We already presented the standard average and the harmonic average and we discussed briefly the advantages of them. The latter equation in (3.41) introduces an exponential treatment of the diffusion coefficient along each edge of the boundary  $\partial K$  of the subdomain  $K$ .

In fact considering that along the edges of  $\partial K$  the approximate flux density computation can be written as a function of its tangential components, then basing on the classical one dimensional *Sharfetter-Gummel* method [ref](#), for each edge  $e_i$ , the tangential component of  $J_h^K(n_h)$  may be defined as:

$$\begin{aligned} j_{e_i} &= \mathcal{H}_{e_i} \frac{\delta_i(e^{-\varphi/V_{th}} n_h)}{|e_i|} = \mathcal{H}_{e_i} \nabla(e^{-\varphi/V_{th}} n_h) \mathbf{t}_i \\ &= \mathcal{H}_{e_i} (qD_n e^{(\varphi/V_{th})}) \frac{\mathcal{B}(\delta_i(\varphi/V_{th})) n_{h,k} - \mathcal{B}(-\delta_i(\varphi/V_{th})) n_{h,j}}{|e_i|} \end{aligned}$$

where

$$\delta_i(\varphi/V_{th}) = \frac{\varphi_k - \varphi_j}{V_{th}} = 2 \frac{(\mathbf{E}_K \cdot \mathbf{t}_{e_i}) |e_i|}{2\mathcal{H}_{e_i} (qD_n e^{(\varphi/V_{th})})} = 2\gamma_i \quad (3.42)$$

$$\mathcal{B}(z) = \begin{cases} \frac{z}{e^z - 1} & z \neq 0 \\ 1 & z = 0 \end{cases} \quad (3.43)$$

being  $\mathbf{E}_K$  the relative electric field on  $K$  and  $|\gamma_i|$  the Péclet number associated with the edge  $e_i$ . From (3.40) we immediately obtain:

$$\mathbf{J}_h^K = \frac{1}{|K|} \sum_{i=1}^6 |e_i| s_i j_{e_i} \mathbf{t}_i \quad (3.44)$$

Furthermore having defined the flux vector over  $K$  in the form (3.44), it is possible to construct a family of Galerkin finite element approximations for the continuity equations by a proper choice of the quantities  $j_{e_i}$  (e.g. upwind techniques).

### The discretization scheme

Given the choice for  $j_{e_i}$  and substituting the equation for  $\mathbf{J}_h^K$  in the bilinear form (3.40), we can compute the local system matrix over each element which reads as follows:



$$\Phi_K = \begin{bmatrix} -\begin{pmatrix} a_{e12}\mathcal{B}_{12}L_{21}^K + \\ a_{e13}\mathcal{B}_{13}L_{31}^K + \\ a_{e14}\mathcal{B}_{14}L_{41}^K \end{pmatrix} & a_{e12}\mathcal{B}_{12}L_{21}^K & a_{e13}\mathcal{B}_{13}L_{31}^K & a_{e14}\mathcal{B}_{14}L_{41}^K \\ a_{e21}\mathcal{B}_{21}L_{12}^K & -\begin{pmatrix} a_{e21}\mathcal{B}_{21}L_{12}^K + \\ a_{e23}\mathcal{B}_{23}L_{32}^K + \\ a_{e24}\mathcal{B}_{24}L_{42}^K \end{pmatrix} & a_{e23}\mathcal{B}_{12}L_{32}^K & a_{e24}\mathcal{B}_{12}L_{42}^K \\ a_{e31}\mathcal{B}_{31}L_{31}^K & a_{e31}\mathcal{B}_{32}L_{32}^K & -\begin{pmatrix} a_{e31}\mathcal{B}_{31}L_{31}^K + \\ a_{e32}\mathcal{B}_{32}L_{32}^K + \\ a_{e34}\mathcal{B}_{34}L_{34}^K \end{pmatrix} & a_{e34}\mathcal{B}_{34}L_{34}^K \\ a_{e41}\mathcal{B}_{41}L_{41}^K & a_{e42}\mathcal{B}_{42}L_{42}^K & a_{e43}\mathcal{B}_{43}L_{43}^K & -\begin{pmatrix} a_{e41}\mathcal{B}_{41}L_{41}^K + \\ a_{e42}\mathcal{B}_{42}L_{42}^K + \\ a_{e43}\mathcal{B}_{43}L_{43}^K \end{pmatrix} \end{bmatrix} \quad (3.45)$$

$$A_K = \Phi_K + \frac{|K|}{4} \text{diag}(\sigma) \quad (3.46)$$

$$\mathbf{F}_K = \frac{|K|}{4} (f_1, f_2, f_3, f_4)^T \quad (3.47)$$

denoting by  $\mathcal{B}_{ij}$  the Bernoulli function applied to the potential difference between node  $j$  and node  $i$ . For the assembling of the system matrix and the imposition of the essential boundary conditions we refer to the previous section.

The discretization scheme just presented is well known as *Edge Averaged Finite Elements* (EAFE) and it's particularly suitable for problems with coefficient highly variable. Furthermore this approach has several good properties, e.i. in 2D simulation if  $\mathcal{T}_h$  is a Delauny partition the system matrix is an *M-matrix* [BCC98]. The main consequence of this statement is that the solution could satisfy the *Discrete Maximum Principle*. This is a notable property which implies that no negative concentrations may occur. Unfortunately this property is not more valid in 3D simulations, indeed the Delauny condition of the mesh is not sufficiently to guarantee that the system matrix of the method is an M-matrix. A more general condition is presented in [XZ99].

**Theorem 3.1** (Zikatanov condition). *The system matrix of the EAFE scheme is an M-matrix if and only if for any fixed edge  $E$  of the partition  $\mathcal{T}_h$  the following inequality holds:*

$$\omega_E = \frac{1}{n(n-1)} \sum_{T \supset E} |k_E^T| \cot \theta_E^T \geq 0, \quad (3.48)$$

where  $n$  is the dimension,  $\sum_{T \supset E}$  means summation over all simplexes  $T$  containing  $E$ ,  $\theta_E^T$  is the angle between the faces  $f_i, f_j \in \mathcal{T}_h$  such that  $f_i \cap f_j = E$  and  $k_E^T$  is the edge in  $T$  which doesn't share any vertices with  $E$ .

*Observation 3.1.* For  $n = 2$  the condition (3.48) means that the sum of the angles opposite to any edge is less than or equal to  $\pi$ , this condition implies that the partition is a Delaunay triangulation.

*Observation 3.2.* Condition (3.48) highlights that in order to satisfy the discrete maximum principle, a partition without obtuse angles is preferable.

We remark that presently meshing software are oriented to care about the minimum angle of the elements, rather than the maximum, resulting that obtain a mesh which satisfied the condition (3.48) it's a really difficult task.

As example in Fig.3.2 we present a simple partition of a cube performed with the Synopsis tool SNMESH. For every element we evaluated how many edges don't satisfy the condition (3.48). It's clear that there are a lot of edges which don't fulfil the condition and moreover we can't recognize a precise pattern. When several bad edges belong to a single element we can indentify the presence of many obtuse angles.

In order to avoid this problem some alternative solutions are proposed in the literature, like the *Orthogonal Subdomain Collocation method* [PC98], but also this approach is not definitely.

Therefore in presence of negative concentration the most used technique during 3D numerical simulation is the increasing of the degree of freedom spent over the problematic regions, which often are the ones where the carrier density decrease.

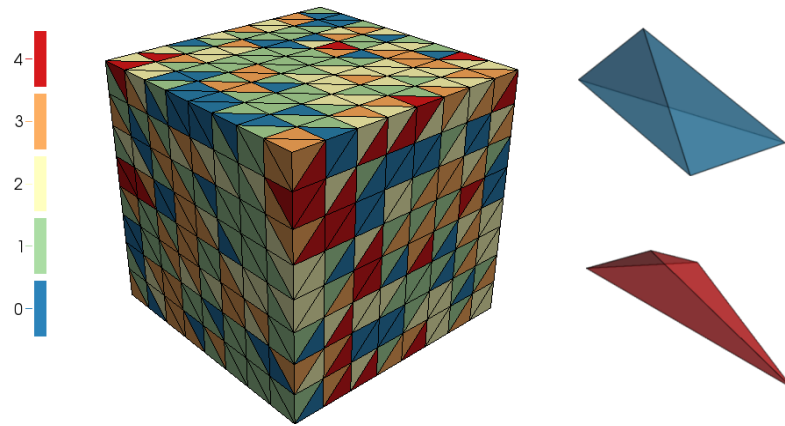


**Figure 3.2:** Evaluation of the Zikatanov condition over a simple partition. Red elements doesn't satisfy condition (3.48) over four edges while blue elements fully accomplished the criterion.

# Chapter 4

## Simulation results

In this chapter we present the work done in order to validate the numerical implementation of the discretization method illustrated in chapter 3 compared with a reference simulation tool (SDEVICE ? by [Sde13]).

In particular we illustrate (and compare) the algorithm used to calculate current at the contacts.

### 4.1 Test cases

We consider three kind of semiconductor devices:

- **p-n junction**
- **p-n junction in oxide**
- **MOSFET n-channel / p-channel**

#### 4.1.1 p-n junction

In this example we consider a simple p-n junction. Fig.4.1 presents the partition and the doping profile used in this test case. The section of the parallelepiped is a  $0.05 \times 0.05[\mu m^2]$  square while the device is  $0.1[\mu m]$  long. The number of vertices are 4933, while the elements are 24576. The doping concentration is obtained setting a constant profile of acceptors over all the domain ( $N_A = 1.0 \times 10^{17}$ ) overwhelmed by a doping profile of donors ( $N_D = 1.0 \times 10^{18}$ ) bounded on one side of the device resulting in an almost abrupt junction. Two contacts are defined: (A) contact is placed at  $Z = 0.1[\mu m]$  and (B) contact is placed at  $Z = 0.0[\mu m]$ .

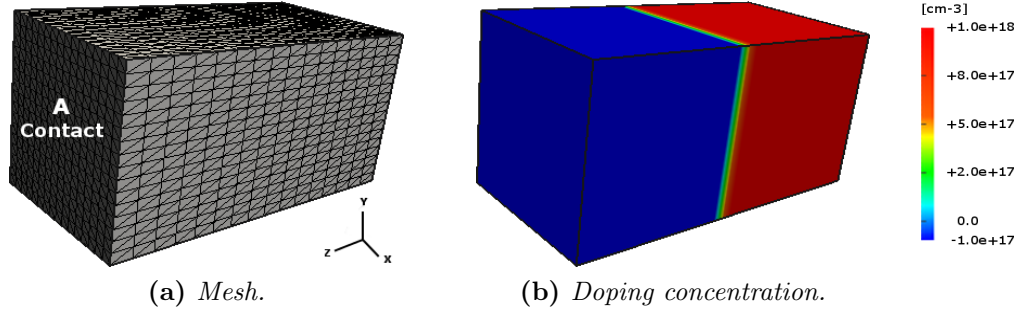


**Figure 4.1:** p-n junction.

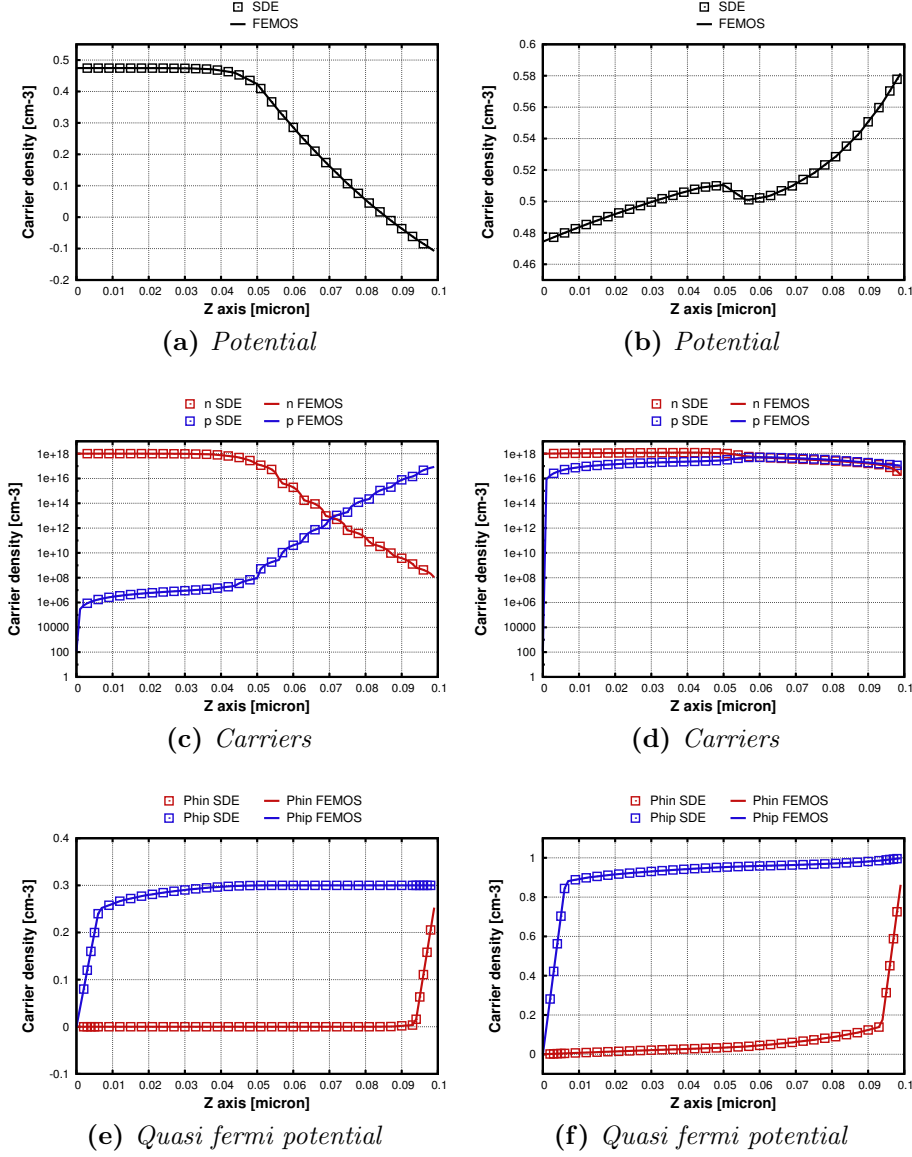
In order to analyze the operating function of the diode, two cases of direct polarization are performed. The setting values and the parameters are summarized in Tab.4.1.

Fig.4.2 reports the solutions for  $V_A = 0.3[V]$  and  $V_A = 1.0[V]$ , along a line parallel to the Z-axis and placed at the center of the device.

Because the built-in voltage is around  $0.7 \div 0.8[V]$  the behaviour of the device is different when the applied bias is below or above this threshold. At  $0.3[V]$  of polarization, potential drop is almost bounded around the junction, and due to the asymmetric doping, is major extended in the p-side. The carriers can't cross the potential barrier and this will cause a low current flux inside the device. At  $1.0[V]$  the minority carriers density becomes almost ten order bigger, resulting in a large amount of current toward the contacts: the device turns from exponential to linear resistive. This is clear in Fig.4.2b where the potential shape becomes similar to a resistance voltage profile (linear potential profile).

Comparing the quasi-fermi potential of Fig.4.2e and Fig.4.2f the boundary layers at contacts increase with the polarization. This effect is related to the ohmic contact hypothesis, and can be avoided with different boundary condition: this occurs also for the carrier concentration because at the contacts the charge neutrality and the thermodynamic equilibrium are imposed.

Fig.4.3÷4.5 shows the comparison between SDEVICE and FEMOS in 3D plots for electrostatic potential, electron and hole densities for bias at  $0.3[V]$ , while Fig.4.6÷4.8 show the same comparison for bias at  $1.0[V]$ . In both of the condition the agreement is very good.



**Figure 4.2:** 1D plots of the solutions and the quasi fermi potential levels along the line parallel to the Z-axis and placed at the center of the device. On the left is presented the test case at  $V_A = 0.3[V]$  while on the right at  $V_A = 1.0[V]$ .

Test case [V]	Mobility model [ $cm^2V^{-1}s^{-1}$ ]	R/G model	$\epsilon_{Si}$
$V_A = 0.3$	$\mu_n = 1417, \mu_p = 470.5$	SRH, Auger	11.6
$V_A = 1.0$	$\mu_n = 1417, \mu_p = 470.5$	SRH, Auger	11.6

**Table 4.1:** p-n junction - list of settings, parameters and models.

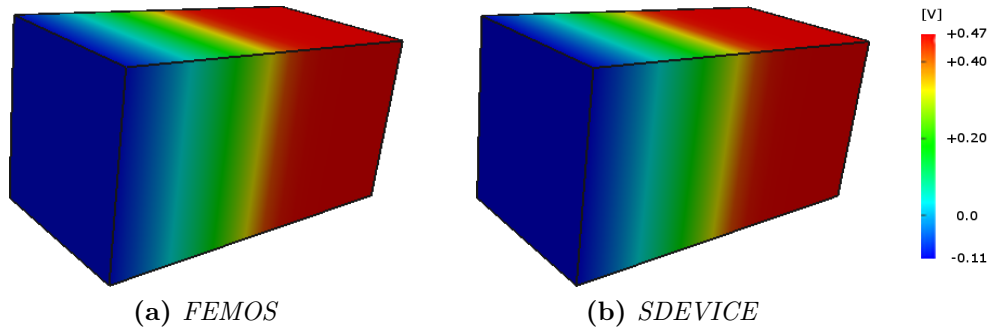


**Figure 4.3:** p-n junction 0.3[V] - Potential.

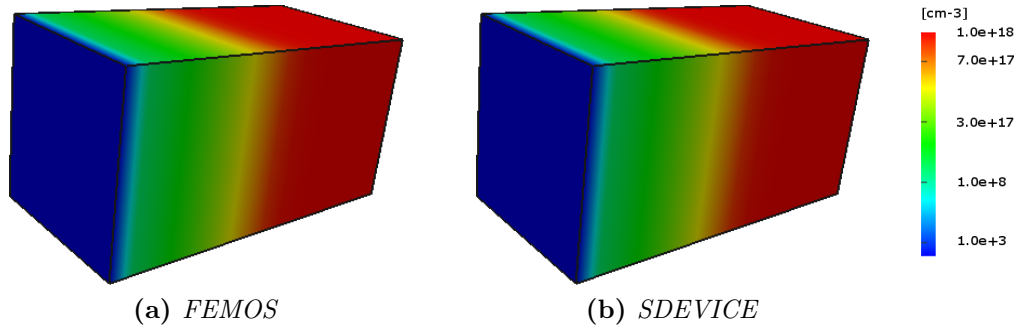


**Figure 4.4:** p-n junction 0.3[V] - Electron density.

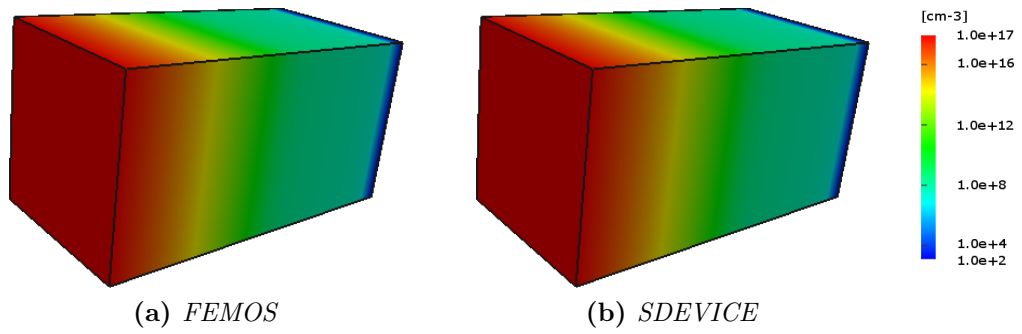


**Figure 4.5:** p-n junction 0.3[V] - Hole density.

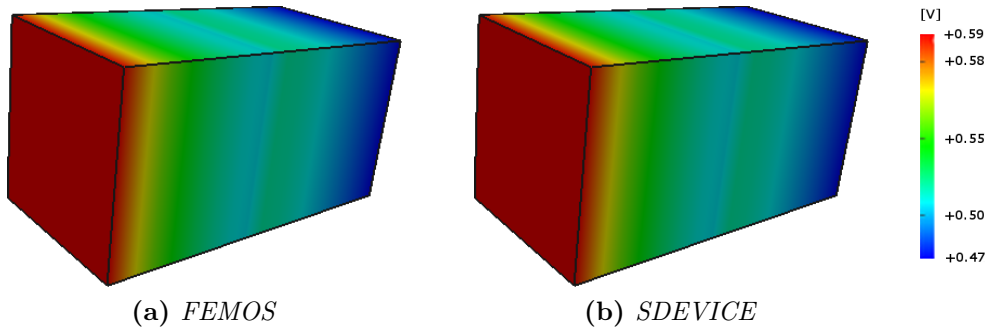


**Figure 4.6:** p-n junction 1.0[V] - Potential.

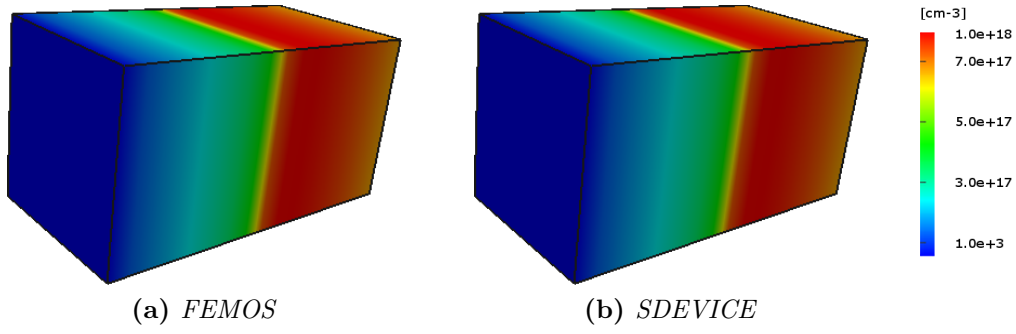


**Figure 4.7:** p-n junction 1.0[V] - Electron density.

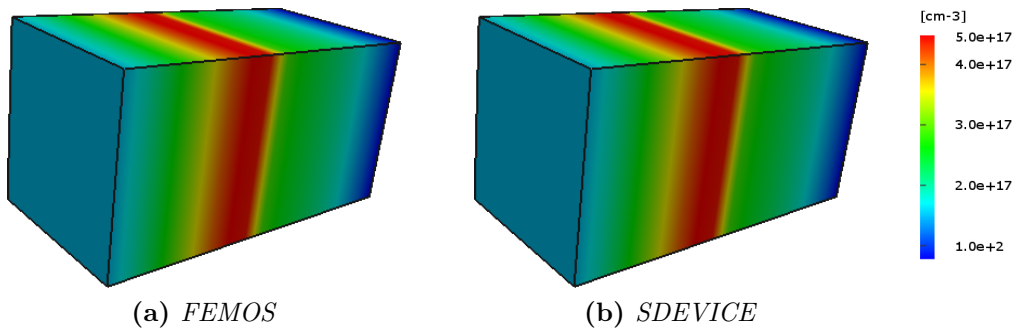


**Figure 4.8:** p-n junction 1.0[V] - Hole density.

### Computational cost and initial condition

It's well known that the convergence time is strictly related to the kind of chosen initial condition: closest to the final solution better it is, however predict in every situations the possible shape of the solutions is hard (if not even impossible). For this reason we have adopted a common and general approach splitting the domain in several regions accordingly to their doping concentration: each of the semiconductor regions are treated as they are in equilibrium with the nearest contact, then the guess value for  $\varphi$  is obtained thanks to the relations (1.18) or (1.19); this choice can be understood for a case close to the equilibrium: this method guarantees good converging performances.

In order to analyze the response of the system at different bias an additional test case is proposed: in the range between 0.0[V] and 3.0[V] several voltages are applied on the previous device and for each bias point the initial guess is computed with the above mentioned way.

Fig.4.9 shows how the computational cost increases with the increasing of the applied bias. Moreover as expected if the mesh is finer, the time needed to find the solution increases, resulting in a rigid shift of the curve toward high time value.

Let us consider the case with coarse mesh. In Fig.4.10 it's evident how the average time spent to solve the NLP and the DD equations remains almost unchanged. On the contrary the number of GM iterations needed by the system to reach the solution, increases for voltages above  $\approx 1.5[V]$ .

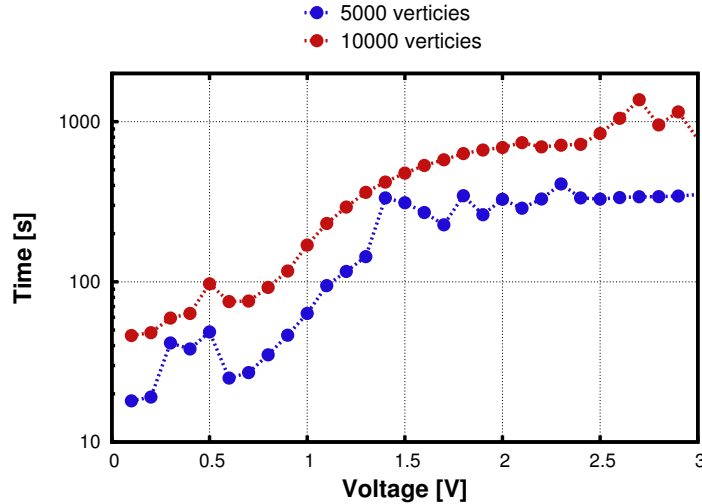


**Figure 4.9:** Total time Gummel Map.



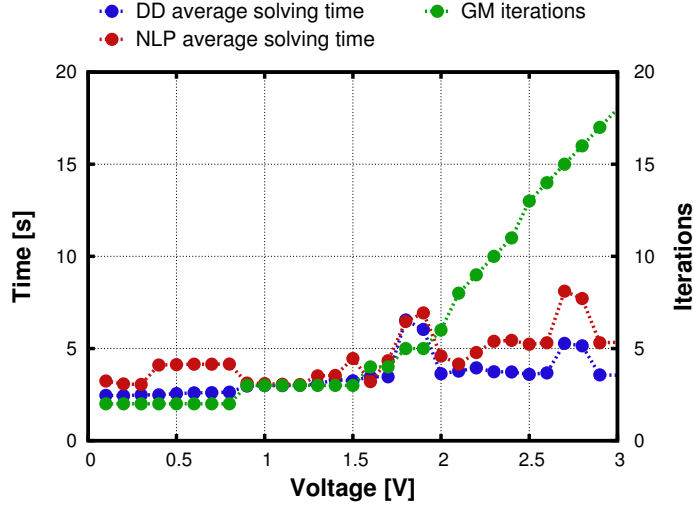


**Figure 4.10:** Time NLP and DD, iteration GM.

A possible explanation of this could be found comparing solution and initial guess for a bias below and above 1.5[V] (similar considerations may be done for carrier densities). When voltage is low, like in Fig.4.11a ( $V_A = 0.1[V]$ ), the potential shape is well predicted by the initial guess, resulting a better convergence for the Gummel map algorithm. On the contrary in Fig.4.11b ( $V_A = 1.6[V]$ ) the device operates as a resistance and the potential profile is close to a linear function: this implies that the solution is far from the initial condition of equilibrium and the algorithm needs more steps.

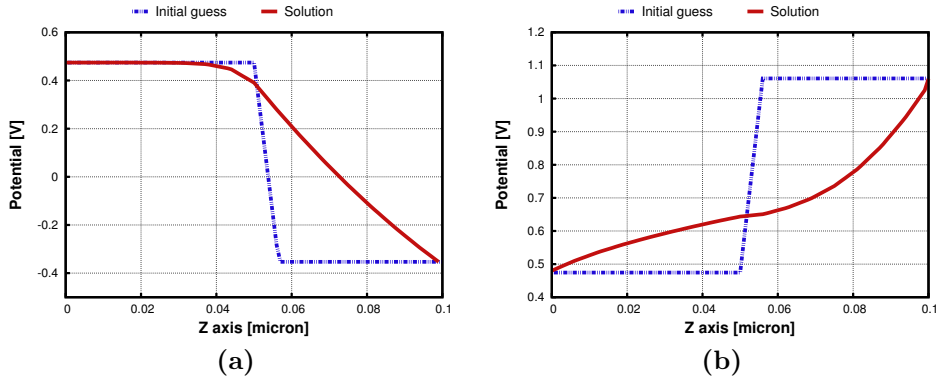


**Figure 4.11:** Initial step for different bias.

### 4.1.2 p-n junction in oxide

In this test case a silicon p-n junction of  $0.3[\mu m]$  long has been surrounded by an oxide layer of  $0.025[\mu m]$  thick. The section of the silicon part is a  $0.1 \times 0.1[\mu m^2]$  square. We spent 6334 vertices overall the domain and 33121 elements. The structure and the doping are well defined in Fig.4.12. The setting of the electrodes is similar to the previously test case and contacts are defined only on silicon surface. Tab.4.2 reports the models and parameters used during the simulations.

Fig.4.13 reports the behaviour of the solutions and the quasi fermi potential levels along a line parallel to the Z-axis and placed at the center of the device. The main features are similar to the previous device, indeed notice the boundary layers at contact for the carrier densities and the quasi fermi potential levels. Fig.4.14 ÷ 4.16 show the 3D solutions for the case at  $0.3[V]$ , while Fig.4.17÷4.19 refer to the case at  $1.0[V]$ . Both in 1D and 3D comparison charts the agreement with the commercial software is good.

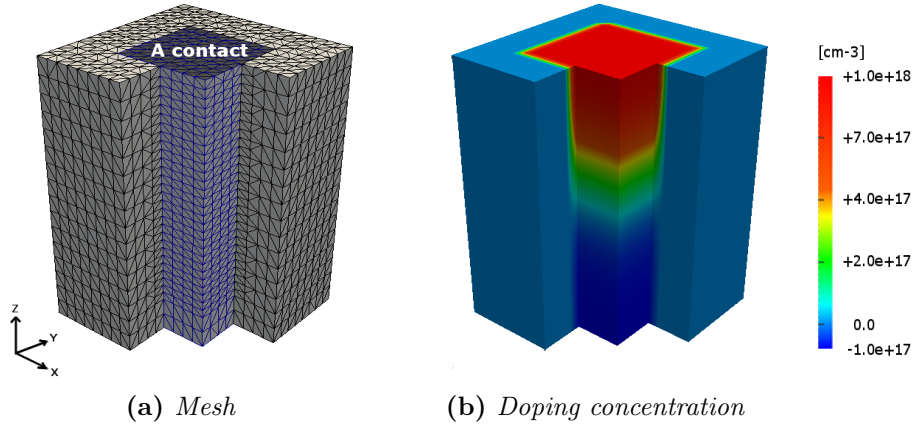


**Figure 4.12:** Test case p-n junction in oxide.

Test case	Mobility model	R/G model	$\epsilon_{Si}$	$\epsilon_{Ox}$
$V_A = 0.3[V]$	$\mu_n = 1417, \mu_p = 470.5$	SRH, Auger	11.6	3.9
$V_A = 1.0[V]$	$\mu_n = 1417, \mu_p = 470.5$	SRH, Auger	11.6	3.9

**Table 4.2:** List of parameters.

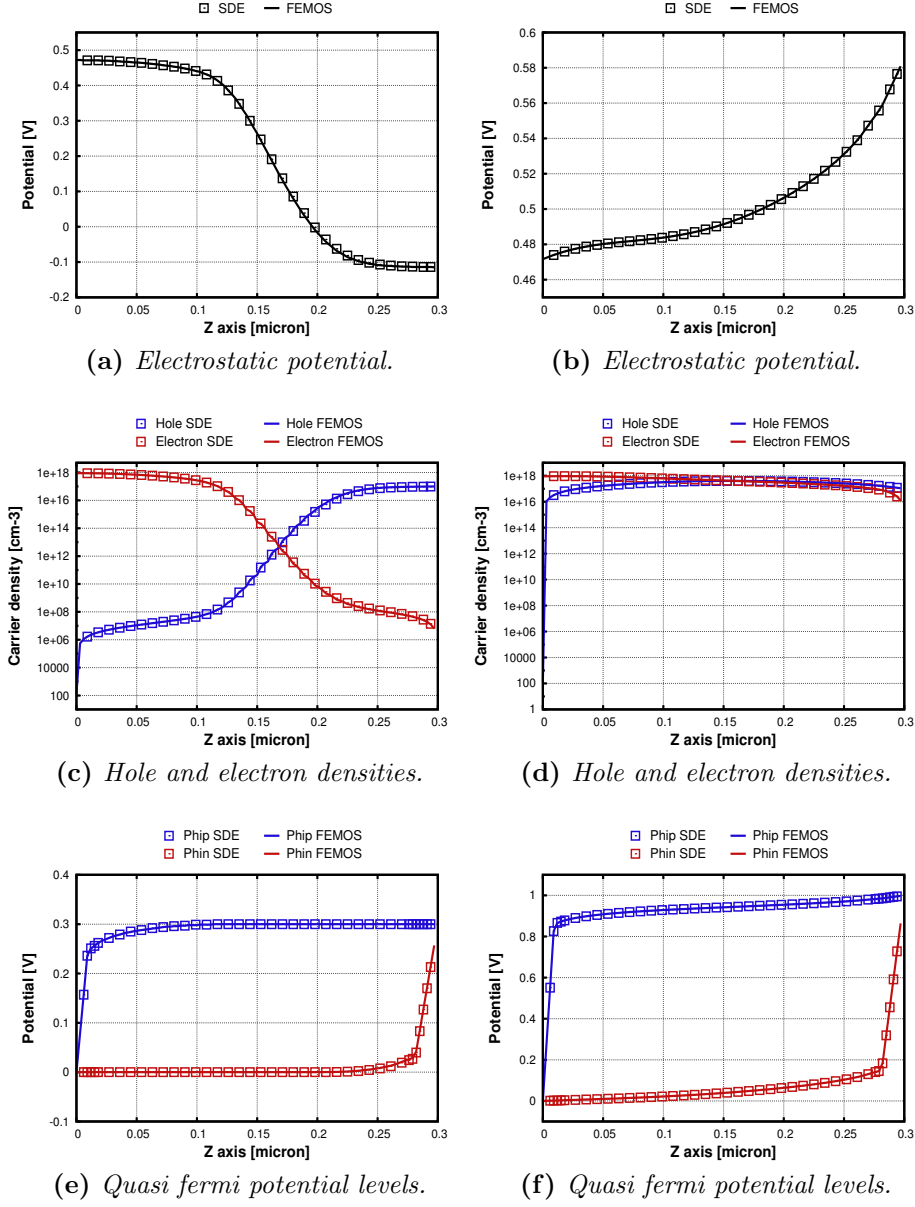


**Figure 4.13:** Plots of the solutions and the quasi fermi potential levels along the line parallel to the Z-axis and placed at the center of the device. On the left is presented the test case at  $V_A = 0.3[V]$  while on the right at  $V_A = 1.0[V]$ .

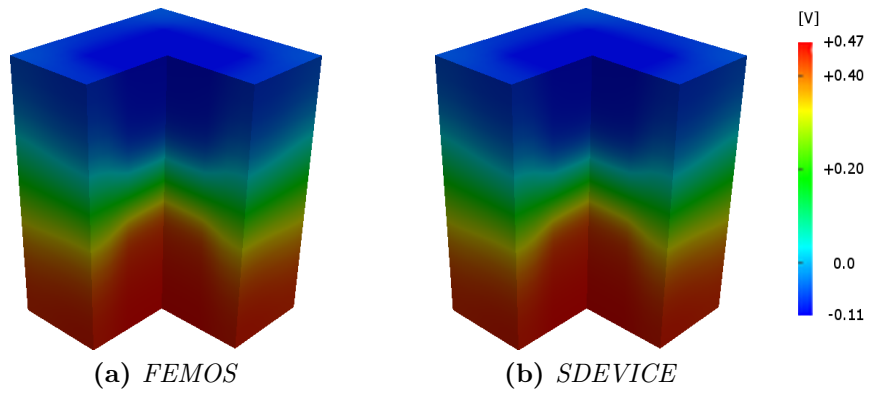


**Figure 4.14:** p-n junction in oxide 0.3[V] - Potential.

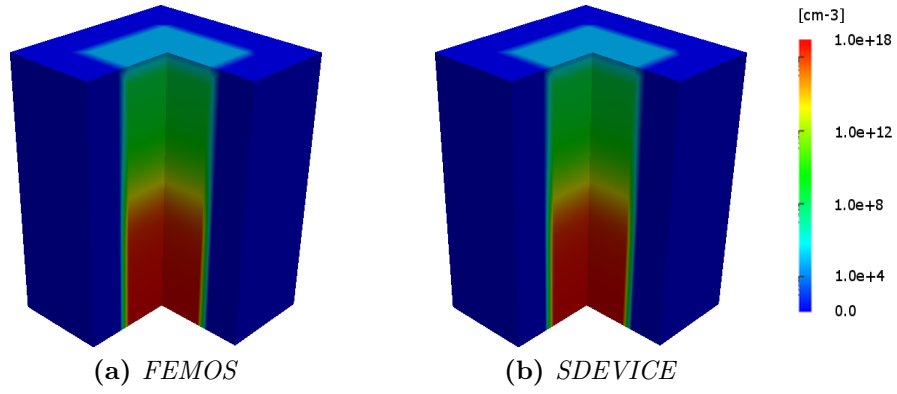


**Figure 4.15:** p-n junction in oxide 0.3[V] - Electron density.

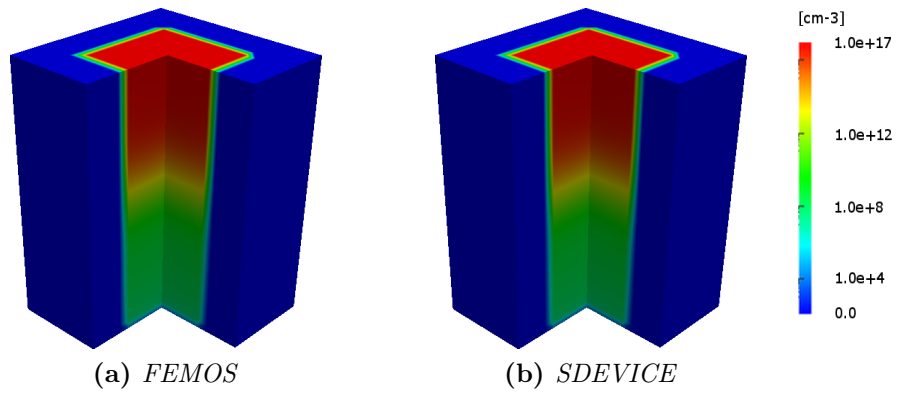


**Figure 4.16:** p-n junction in oxide 0.3[V] - Hole density.

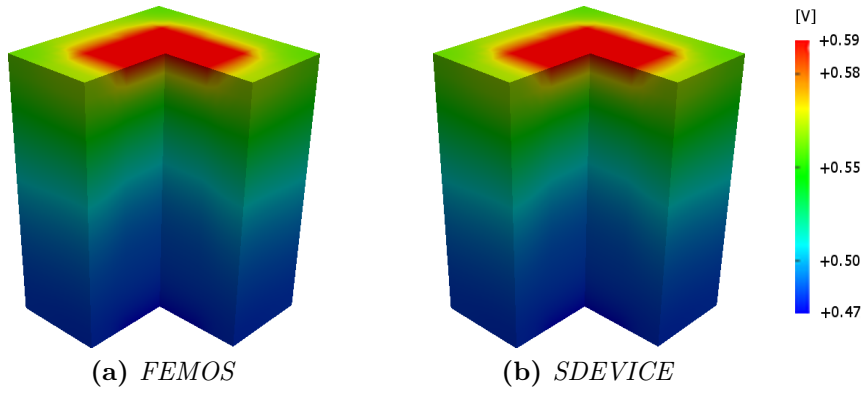


**Figure 4.17:** p-n junction in oxide 1.0[V] - Potential.

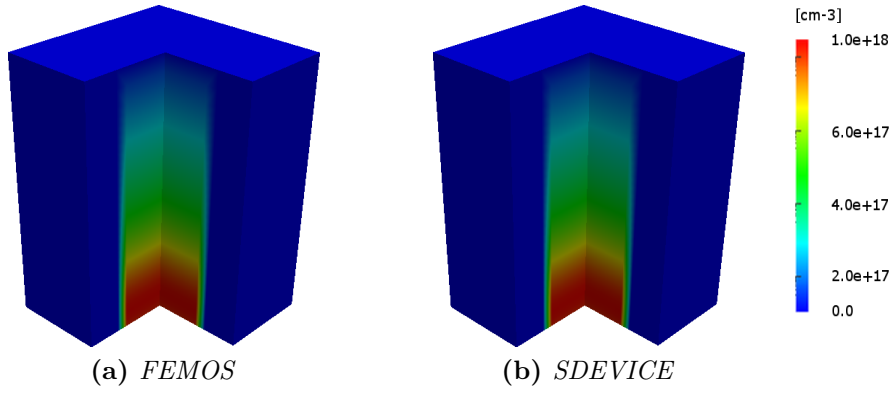


**Figure 4.18:** p-n junction in oxide 1.0[V] - Electron density.

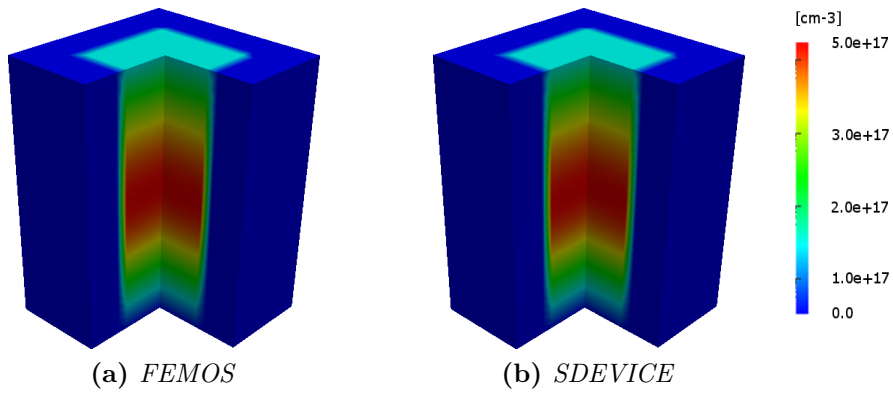


**Figure 4.19:** p-n junction in oxide 1.0[V] - Hole density.

### 3D effect of the electric field

Looking at Fig.4.14 it's clear that for low bias the electrostatic potential behaves differently in the two materials. This phenomenon could be explained if we think about the relation (1.29) between electric field and potential. In fact, as we imposed  $\nabla\varphi \cdot \mathbf{n} = 0$  on the oxide boundary no field lines of the electric field could cross that boundary. The consequence is that all the field lines could start and end only from the contact A or B. Polarization can't operate directly on the oxide and the behaviour of the the electric field inside the device is due only to the displacement effect in the junction of the silicon, which imposes the electric response in the oxide material. Fig.4.20 reports the field lines of the electric field in the case  $V_A = 0.3[V]$  comparing with the commercial software. The visible effect is a lower magnitude of the electric field in the oxide, resulting a more diffused potential.

This phenomena seems to disappear for high bias: in Fig.4.17 the influence of the contact (A) becomes much higher and the electrostatic potential tends to conform over the entire domain.

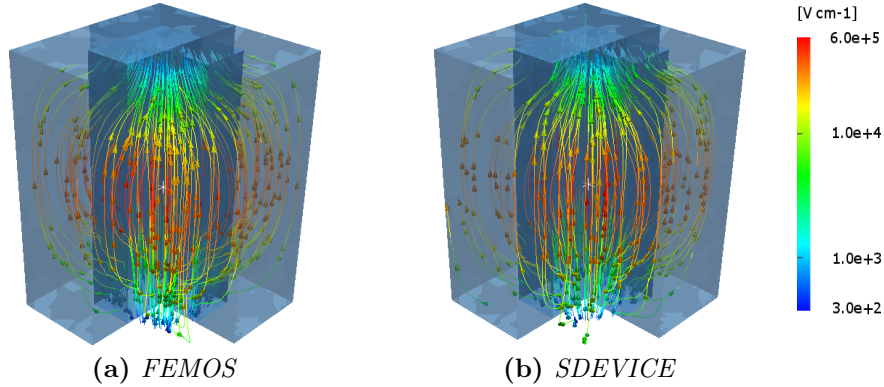


**Figure 4.20:** Test case dide p-n in oxide 0.3[V] - Electric field.

It is important to note that displacement formulation approach doesn't satisfied in a strong manner the priciple of action and reaction. This is equivalent to say that given two element  $K_i, K_j \in \mathcal{T}_h$  such that  $K_i \cap K_j = f_i$  where  $f_i \in \mathcal{F}_h$  and let be  $\mathbf{n}_i$  the outward normal vector of  $\partial K_i$  and  $\mathbf{n}_j$  the outward normal vector of  $\partial K_j$ , we ensure the following equations only in a weak way

$$\mathbf{D}|_{K_i} \cdot \mathbf{n}_i = \mathbf{D}|_{K_j} \cdot \mathbf{n}_j \quad (4.1)$$

$$\mathbf{J}_n|_{K_i} \cdot \mathbf{n}_i = \mathbf{J}_n|_{K_j} \cdot \mathbf{n}_j \quad (4.2)$$

$$\mathbf{J}_p|_{K_i} \cdot \mathbf{n}_i = \mathbf{J}_p|_{K_j} \cdot \mathbf{n}_j \quad (4.3)$$

In fact taking in consideration equation (4.1), we can state that along the interface silicon-oxide the following equality holds

$$\epsilon_{ox} \mathbf{E}|_{K_i} \cdot \mathbf{n}_i = \epsilon_{Si} \mathbf{E}|_{K_j} \cdot \mathbf{n}_j \quad \Rightarrow \quad [\mathbf{E}|_{K_i}]_y = \frac{\epsilon_{Si}}{\epsilon_{ox}} [\mathbf{E}|_{K_j}]_y \quad (4.4)$$

Accordingly with the parameters used during the simulations  $\epsilon_{Si}/\epsilon_{ox} = 2.97$ , which means that the normal component on the interface of the electric field makes a jump passing from oxide to semiconductor and vice versa. It's possible to appreciate this effect looking at Fig.4.21 which shows a plot of  $E_y$  along a line parallel to the Y-axis crossing both oxide and silicon material. For this setting  $E_y \equiv \mathbf{E} \cdot \mathbf{n}$  on the interface and the drop of magnitude is quite visible. The ratio between the two interfaces is almost 3.8 for both  $y = 0.05[\mu m]$  and  $y = 0.15[\mu m]$ . This example really shows the effect of the phenomenon we mentioned before and the consequence which the solutions could own.

Furthermore every tetrahedral interfaces of the partition are affected by this problem, which means that inside an inhomogeneous material the normal component of the electric field doesn't conserve from one element of the grid to the neighbouring ones. Even the presence of this drawback, the solutions obtained are good, but if you would satisfy equation (4.1) in a strong manner you need to move for mixed-hybrid formulation which ensures the conservation of the flux even under possible strong discontinuities of material properties.

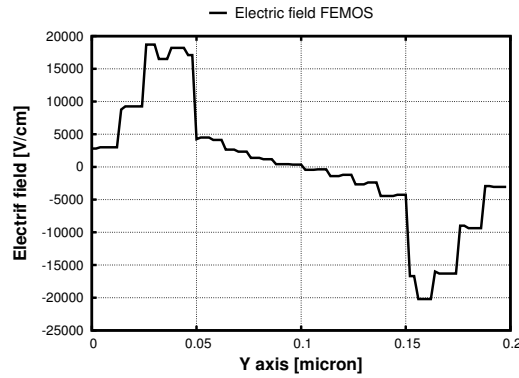


**Figure 4.21:**  $E_y$  along a line parallel to Y-axis,  $z = 0.22[\mu m]$  and  $x = 0.1[\mu m]$ .

### 4.1.3 MOSFET n-channel

The description of MOSFET device can be found in [YT09]: it is a four-terminal device with the electrodes designated as gate (G), source (S), drain (D) and substrate or bulk (B). The gate electrode is usually made of metal or heavily doped polysilicon and is separated from the substrate by a thin silicon dioxide. The surface region under the gate oxide between source and drain is called the *channel* region. Because the current in a MOSFET is transported predominantly by carriers of one polarity, the MOSFET is usually referred to as a unipolar or majority-carrier device: as a propose of test we consider a n-channel (n-MOSFET) or a p-channel (p-MOSFET). An *n-MOSFET* (p-MOSFET) consists of a p-type (n-type) silicon substrate into which two n-regions (p-regions) are the designing source and drain. The n-regions (p-regions) are doped accordingly with a gaussain profile as occuring from an implantation. Fig.4.22a and Fig.4.22b shows the geometry and the doping concentration for the n-MOSFET used throughout the course of these simulations (2739 verticies and 12338 elements). We note that the mesh has been refined where the more interesting phenomena occur: along channel, over the depletion regions and at drain/source contacts.

When no voltage is applied to the gate, no current flows between the source and drain, while if a sufficiently large positive voltage is applied to the gate, the silicon surface is inverted to n-type (p-type), which forms a conducting channel between the source and drain: applying a positive voltage to the drain (source) the electrons (holes) start to flow from source to drain and therefore a current is generated.

The explanation of the MOSFET working principle has ben clarified in Fig.4.23 where for the case of n-channel the band profile along the channel axis has been reported for two different gate bias. The voltage applied to the

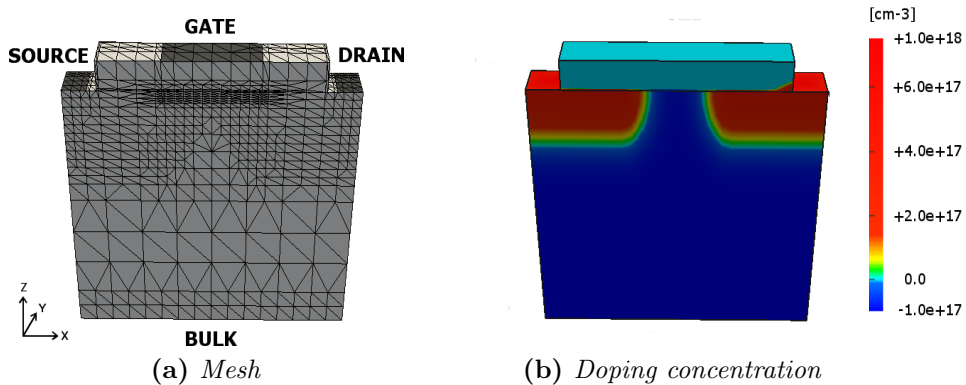


**Figure 4.22:** Geometry of the test case MOS n-channel.



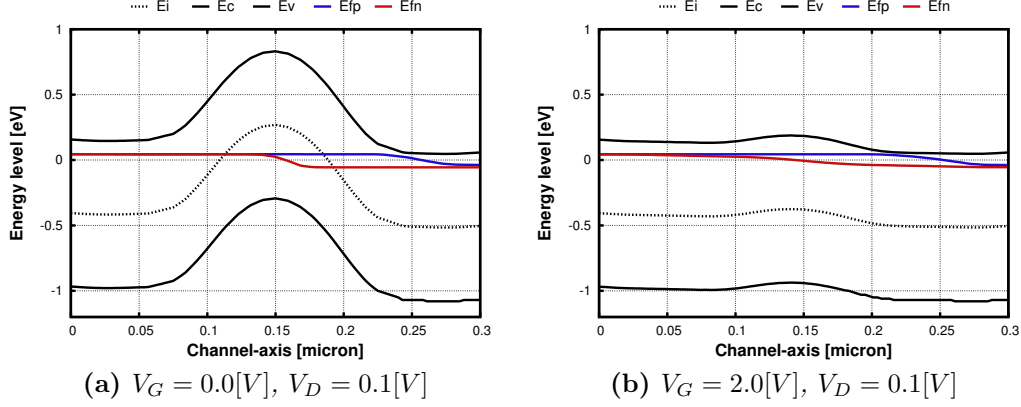


**Figure 4.23:** Energy band levels for nMOSFET along channel.

gate tends to decrease the band levels in the channel region: in this configuration a little drain voltage causes the flow of the electron as the energy barrier doesn't exist anymore. Another point of view of the phenomenon is given by Fig.4.24a which shows for an n-channel the profile of carrier concentrations in the middle of the channel cut perpendicular to the gate, for off-state and on-state: the inversion occurs when the gate voltage is higher than MOSFET threshold. Fig.4.24b shows the 3D view of the n-channel space charge after inversion.

The parameters and models used for these simulations are summarized in Tab.4.3. Fig.4.26÷4.28 shows the 3D components of the electrostatic potential, electron density and hole density between the FEMOS results and the commercial code for the off-state MOSFET ( $V_G = 0.0[V]$ ), while Fig.4.29÷4.31 for the on-state MOSFET ( $V_G = 2.0[V]$ ): the agreement is very good.

Finally Fig.4.25 reports the streamline plot of the electric field inside the device for FEMOS and the SDEVICE in the case of on-state MOSFET.

Test case	Mobility model	R/G model	$\epsilon_{Si}$	$\epsilon_{0x}$
$V_G = 0.0[V]$ , $V_D = 0.0[V]$ , $V_S = V_B = 0.0[V]$	$\mu_n = 1417$ $\mu_p = 470.5$	SRH, Auger, II	11.6	3.9
$V_G = 2.0[V]$ , $V_D = 0.1[V]$ , $V_S = V_B = 0.0[V]$	$\mu_n = 1417$ $\mu_p = 470.5$	SRH, Auger	11.6	3.9

**Table 4.3:** List of parameters.

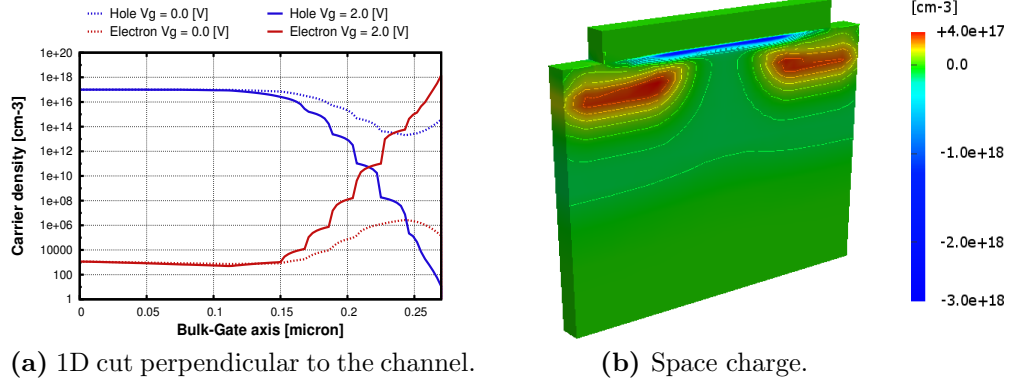


**Figure 4.24:** Channel of the nMOSFET.

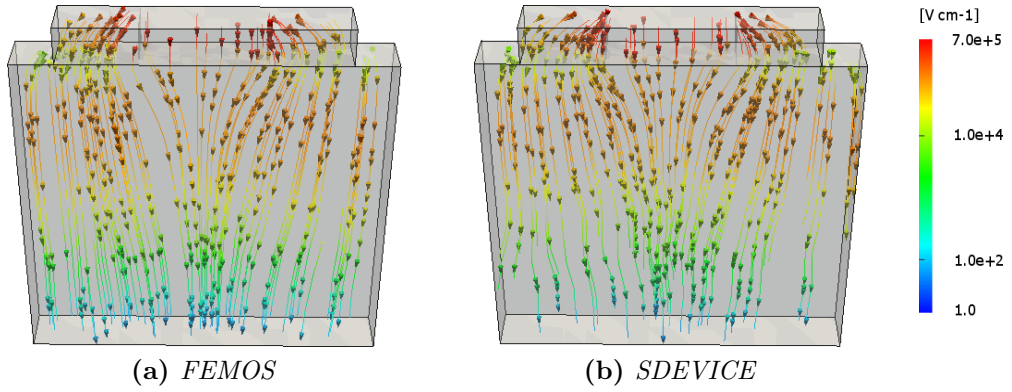


**Figure 4.25:** Electric field density -  $V_G = 2.0[V]$ .

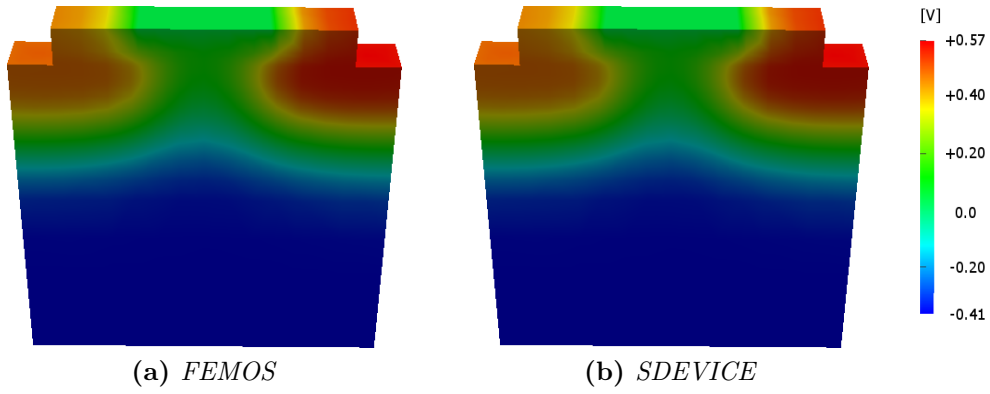


**Figure 4.26:** Electrostatic potential -  $V_G = 0.0[V]$ .

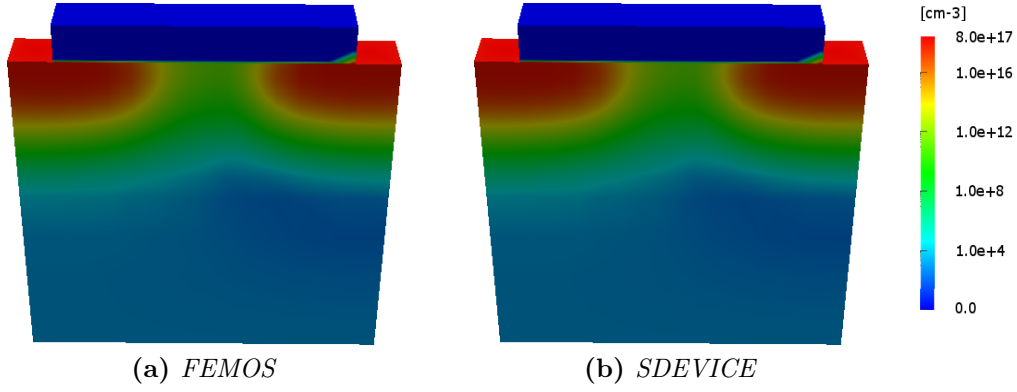


**Figure 4.27:** Electron density -  $V_G = 0.0[V]$ .

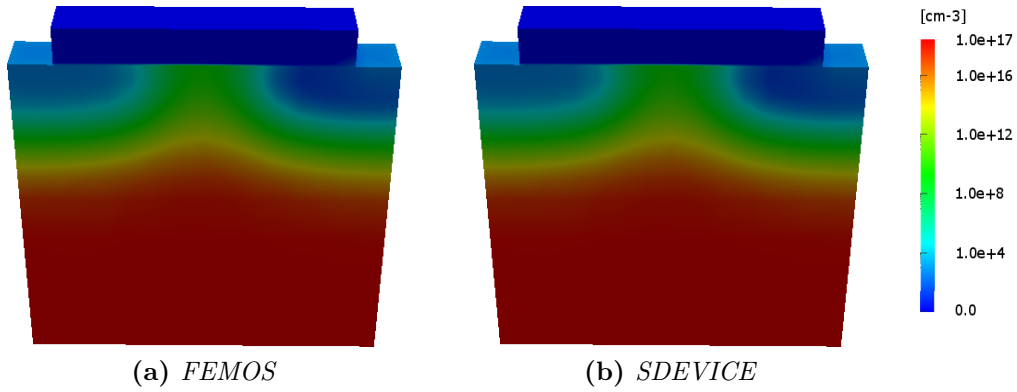


**Figure 4.28:** Electron density -  $V_G = 0.0[V]$ .

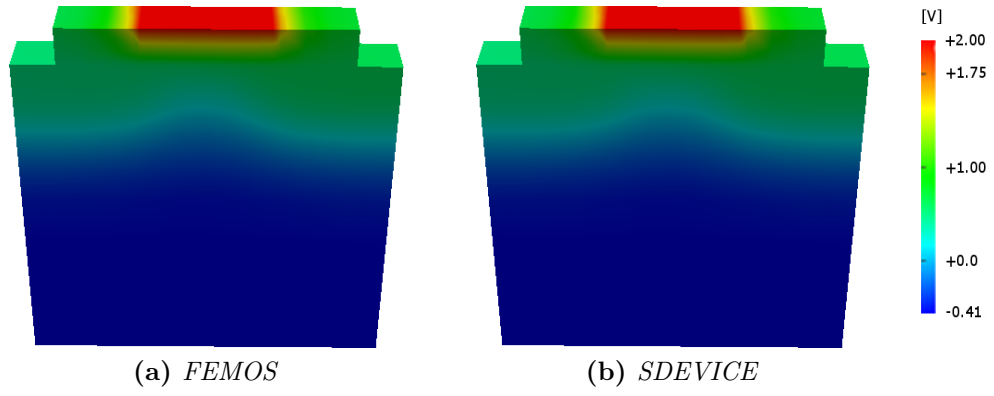


**Figure 4.29:** Electrostatic potential -  $V_G = 2.0[V]$ .

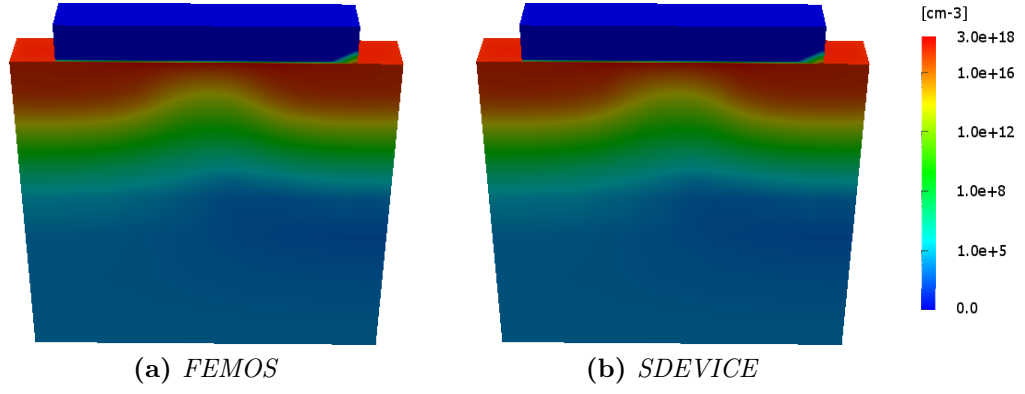


**Figure 4.30:** Electron density -  $V_G = 2.0[V]$ .

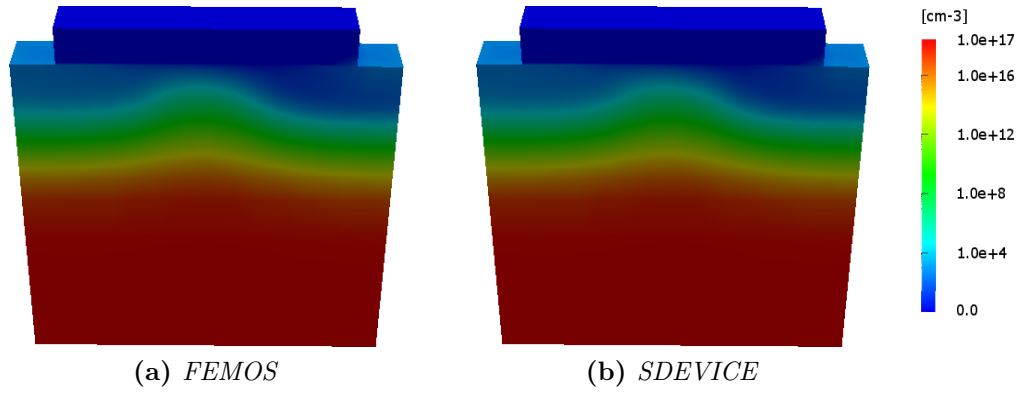


**Figure 4.31:** Electron density -  $V_G = 2.0[V]$ .

### Inverse polarization

In section 3.3.3 we pointed that the discretization scheme (EAFE) can't satisfy the discrete maximum principle in 3D simulations unless we satisfy condition (3.48). Therefore it is possible encounter negative solution and we usually have to deal with this problem when the concentration of electrons and holes become low.

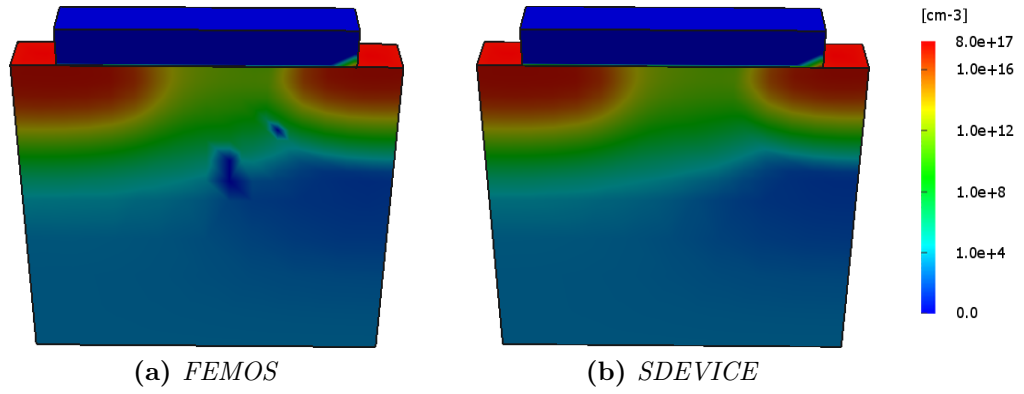
In order to hilight this possible critical situation n-channel MOSFET has put in inverse polarization by grounded all contacts except the drain which is ramped to  $0.5[V]$ : models and parameters are reported in Tab.4.4.

Fig.4.32 reports the solutions for the electron density computed with FEMOS and SDEVICE using the mesh presented in Fig.4.22b: the results are comparable, but near the drain-bulk junction the FEMOS solution presents some points with negative concentrations. Increasing drain bias the phenomenon will tend to spread over a larger area, untill it affects irremediably the computation. As we anticipated in chapter 3, the most practice technique to avoid this problem is the addition of degrees of freedom around the problematic regions. Fig.4.33a represents a finer mesh with 13000 points and 67388 elements. Using this mesh the correctness of the solution is recovered Fig.4.33b. In Fig.4.34, it's interesting notice how the satisfaction of condition (3.48) changes between the different meshes used: increasing the number of degrees of freedom over the critical region guarantees a better fulfillment of (3.48). Results suggest us that in order to treat this situation it may be useful implement a suitable a-posteriori error estimation and adaptive mesh refinement techniques.

Finally Fig.4.35 and Fig.4.36 presents the solution of electrostatic potential and hole density computed with the finer mesh and compared with the commercial tool: also for that quantity the agreement is good.

Test case	Mobility model	R/G model	$\epsilon_{Si}$	$\epsilon_{0x}$
$V_G = 0.0[V]$ , $V_D = 0.5[V]$ , $V_S = V_B = 0.0[V]$	$\mu_n = 1417$ $\mu_p = 470.5$	SRH, Auger, II	11.6	3.9

**Table 4.4:** List of parameters.



**Figure 4.32:** Negative carriers for the electron density solution.

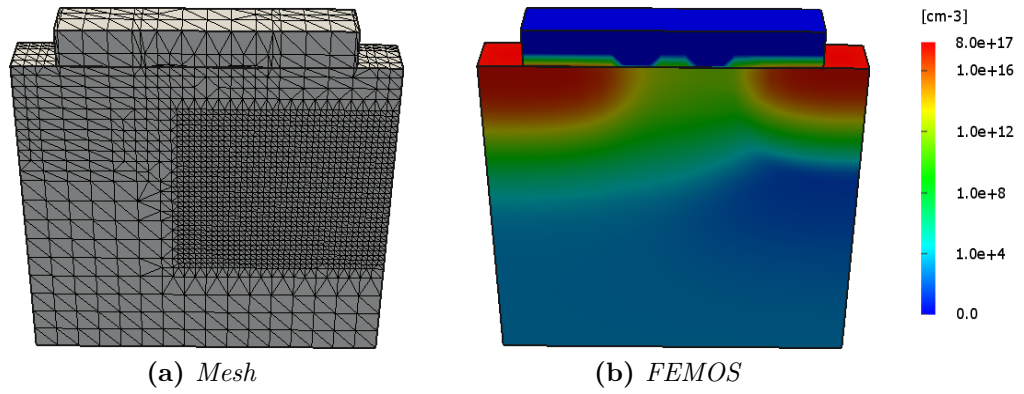


**Figure 4.33:** Electron density with finer mesh.

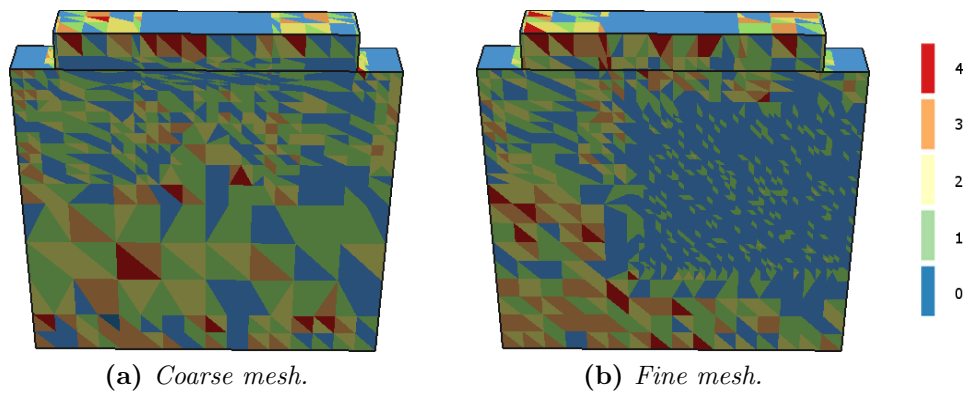


**Figure 4.34:** Satisfaction of the Zikatanov condition.

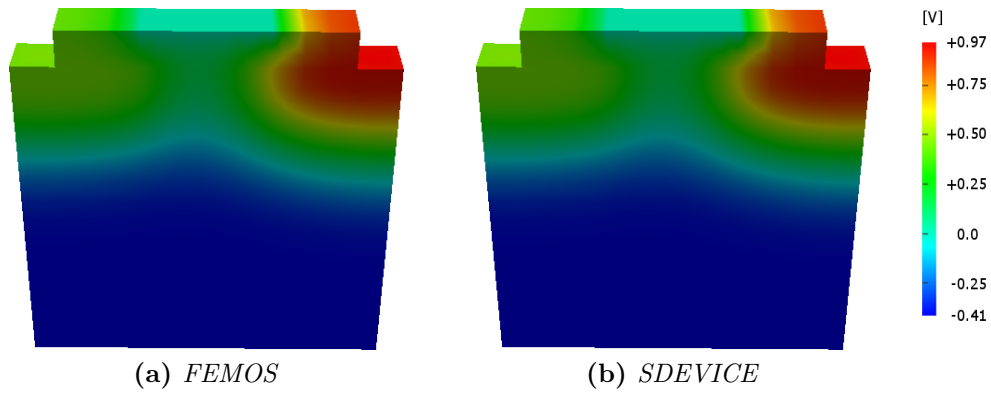


**Figure 4.35:** Electrostatic potential - Inverse polarization.

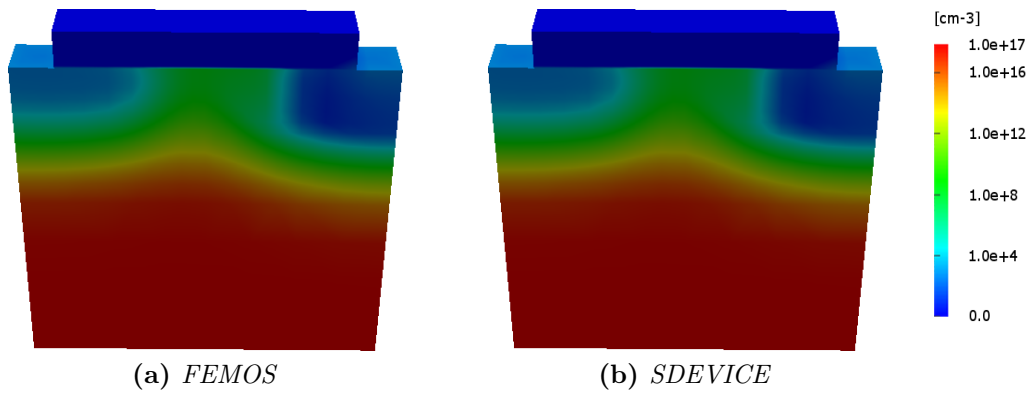


**Figure 4.36:** Hole density - Inverse polarization.

## 4.2 Calculation of the current at contacts

During the analysis of an electric device, one of the most useful information is the electrical response at terminals. In order to accomplish this target we have to compute the integral of the electron and hole current density over a generic 2D electrode. We refer here to the procedure found in [GS74] (*residue method*) for the 2D case: the analysis make is easiliy extendable to the 3D case if we consider also the work [HEML00]. Moreover we remark that the method can be succesfully applied to a wide spread of applications, including contact charges, carrier quantum probability fluxes and heat fluxes.

A contact is defined by a surface and more precisely we can consider  $\Gamma_{D,Si} = \bigcup_{c=1}^d \Gamma_c$  where  $d$  is the number of terminals on the device and  $\forall c = 1, \dots, d$ ,  $\Gamma_c$  is the  $c$ -th contact. For each contact we need to compute the total current  $I_c$  as:

$$\mathcal{I}_c = \mathcal{I}_c^n + \mathcal{I}_c^p \quad (4.5)$$

where  $\mathcal{I}_c^n$  is the contribution of the electron current and  $\mathcal{I}_c^p$  is the contribution of the hole current. For a given contact  $\Gamma_c$ , the fluxes of the current density assume the following form:

$$\mathcal{I}_c^\nu = \int_{\Gamma_c} \mathbf{J}_\nu(\nu) \cdot \mathbf{n} d\Gamma \quad \nu = \{n, p\} \quad (4.6)$$

where as usual  $\mathbf{n}$  is the unit outward normal of the domain boundary. It's well known that the evaluation of boundary integrals is a difficult task. Many difficulties in the numerical evalutaion of (4.6) arise from singularities in spatial derivatives of the approximate solution  $n_h$  or  $p_h$  near the contact edges, due to a change in the boundary condition type from Dirichlet to Neumann at the contact ends.

Consider the discretized electron continuity problem (3.34) and let be  $\eta$  the set of all vertices of the partition  $\mathcal{T}_h$ . We can split the set of total nodes in contact node  $\eta_g \in \Gamma_{D,Si}$  and the complementary part  $\eta_n \in \Gamma_{N,Si}$ . We define an *auxiliary flux*  $H_h$  on  $\Gamma_{D,Si}$  as

$$H_h = \sum_{i \in \eta_g} H_{h,i} \psi_i \quad (4.7)$$

Now given the spaces:



$$\begin{aligned}
\mathcal{V}_h &= \text{span}\{\psi_i\}_{i \in \eta_n} \\
\mathbf{V}_h &= \text{span}\{\psi_i\}_{i \in \eta_g} \\
\mathcal{S}_h &= \{u \in \mathcal{V}_h \oplus \mathbf{V}_h : u|_{\Gamma_{D,S_i}} = n_D\}
\end{aligned}$$

it's possible write a modified form of Glakerin's method which reads as:  
find  $n_h \in \mathcal{S}_h$  and  $H_h \in \mathbf{V}_h$  such that

$$(W_h, H_h)_{\Gamma_{D,S_i}} = a(W_h, n_h) - F(W_h) \quad \forall W_h \in \mathcal{V}_h \oplus \mathbf{V}_h \quad (4.8)$$

where  $a(\cdot, \cdot)$  is the bilinear form (3.34) and  $F(\cdot)$  the relative functional. Equation (4.8) splits into two subproblems:

$$0 = a(w_h, n_h) - F(w_h) \quad \forall w_h \in \mathcal{V}_h \quad (4.9)$$

$$(W_h, H_h)_{\Gamma_{D,S_i}} = a(W_h, n_h) - F(W_h) \quad \forall W_h \in \mathbf{V}_h \quad (4.10)$$

Problem (4.9) is identical to the unmodified case and can be treated as before or using a different discretization scheme. Once obtained the solution  $n_h$  problem (4.10) is fully decoupled from (4.9) and we can determines  $H_h$  as follows

$$(H_h, \psi_i)_{\Gamma_{D,S_i}} = a(\psi_i, n_h) - F(\psi_i) \quad \forall i \in \eta_g \quad (4.11)$$

[HEML00] demonstrates that  $H_h$  defines the conserved total flux along  $\Gamma_{D,S_i}$  and accordingly with the boundary condition, the following equality is obtained

$$\int_{\Gamma_{D,S_i}} H_h d\Gamma = - \int_{\Omega_{S_i}} qR d\Omega \quad (4.12)$$

On the other hand if we apply the Divergence theorem on (2.30) we can state

$$\int_{\Gamma_{D,S_i}} \mathbf{J}_n \cdot \mathbf{n} d\Gamma = \int_{\Omega} -qR d\Omega \quad (4.13)$$

Equation (4.12) and (4.13) lead us to conclude that for all contacts holds

$$\mathcal{I}_c^n = \int_{\Gamma_c} H_h d\Gamma \quad (4.14)$$

In order to compute (4.14) let be  $\eta_c$  the set of nodes of the contact  $\Gamma_c$ , the following equalities hold

$$\sum_{l \in \eta_c} \int_{\Gamma_c} H_h \psi_l d\Gamma = \int_{\Gamma_c} H_h \sum_{l \in \eta_c} \psi_l d\Gamma = \int_{\Gamma_c} H_h d\Gamma \quad (4.15)$$

Accordingly with (4.15) we can reinterpret  $(H_h, \psi_i)_{\Gamma_{D,S_i}}$  as the contribution to the flux at node  $i$  and therefore the current at contact  $c$  is given by summing over the vertices  $\eta_c$  this quantity.

Therefore the residue method is: given the system matrix  $A$  of the Drift-Diffusion equation, the solution  $n_h$  and the right hand side  $\mathbf{b}$ ,  $\forall c = 1, \dots, d$  the contribution to the total contact current is

$$\mathcal{I}_c^n = (An_h - \mathbf{b}) \cdot \mathbb{I}_c \quad (4.16)$$

where

$$[\mathbb{I}_c]_i := \begin{cases} 0 & i \notin \eta_c \\ 1 & i \in \eta_c \end{cases} \quad (4.17)$$

Obiously the result is holds also for the hole continuity equation.

### 4.2.1 Results

We shall apply the residue method and compare the calculation of the current at the contact with the result of SDEVICE, for the devices previously presented. In this section we compare also the different mobility and recombination/generation model.

#### p-n junction

First of all we are interested to reproduce the well known characteristic of the diode. Considering the device presented in section 4.1.1 we grounded the B contact and then A contact is ramped from  $-7.5[V]$  to  $2.0[V]$ . Tab.4.5 reports the parameters used in simulation. In Fig.4.37 we plot the electron and hole current at contact A. Diode breakdown voltage is appearing around  $-7.0[V]$  and it's quite aligned with the one guess by SDEVICE.

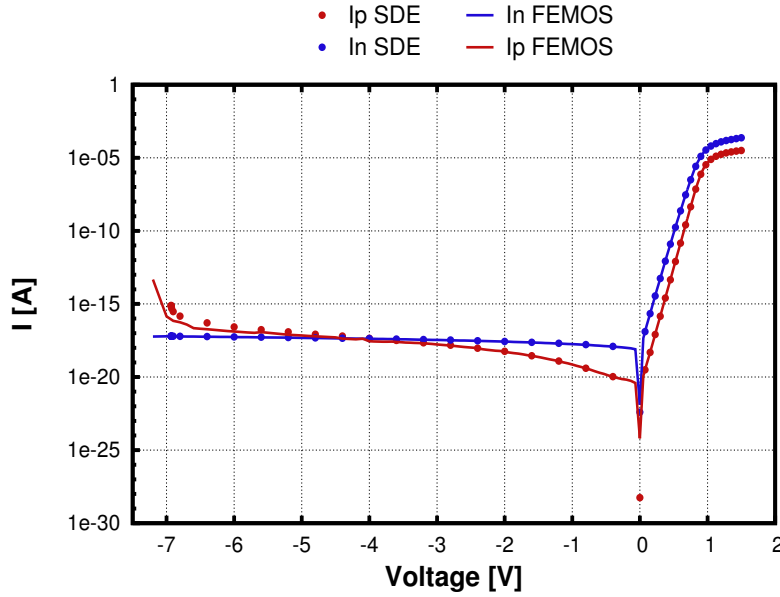
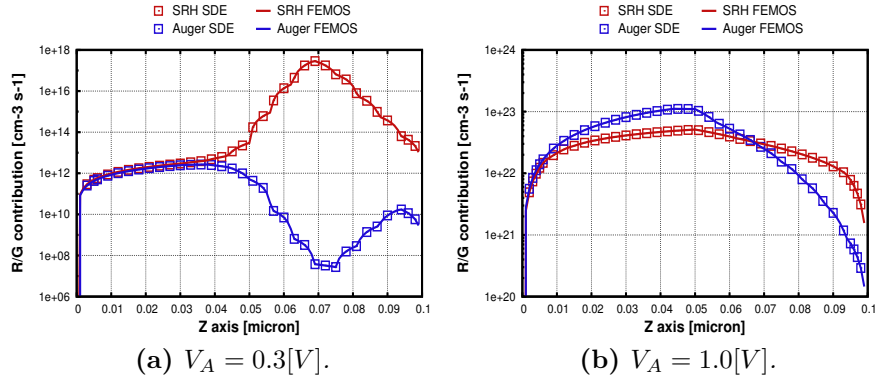


Figure 4.37: Diode characteristic.

Test case	Mobility model	R/G model	$\epsilon_{Si}$	$\epsilon_{0x}$
$V_A = -7.5 \div 1.5[V]$ , $V_B = 0.0[V]$	$\mu_n = 1417$ $\mu_p = 470.5$	SRH II, Auger	11.6	-

Table 4.5: List of parameters.

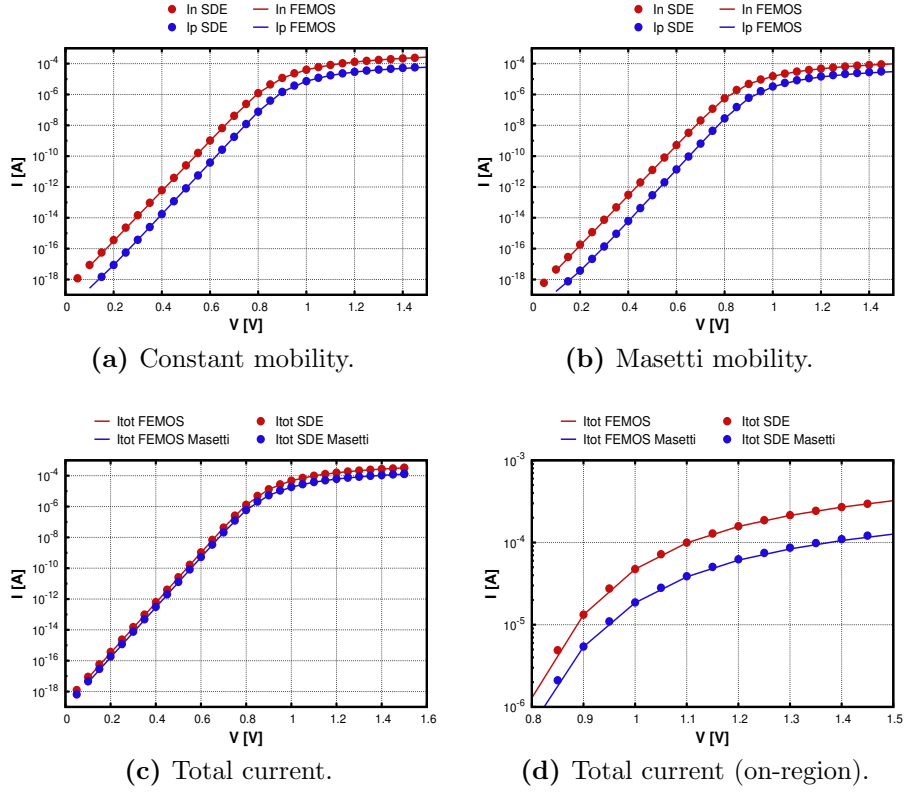
We are also interested to validate the agreement with SDEVICE about the R/G models implemented. Fig.4.38 shows the different behaviour of the SRH and Auger R/G contribution for two voltages. The plots are made along a line parallel to the Z-axis and placed at the center of the device. Notice that under the built-in voltage both SRH and Auger are not significative. Moreover Auger contribution decreases in the depletion region as it depends strictly by the carrier concentrations. The situation is very different for bias higher than the built-in: the R/G phenomena are distributed over the entire device with a large amount of producing carriers which causes the saturation of the device. The physic effect is well predicted and moreover the agreement with the commercial tool is good.



**Figure 4.38:** SRH and Auger RG contribution.

### p-n junction in oxide

We obtained correct results also for the diode surrounded by the oxide. For this test case we analyzed the influence of the Masetti mobility model to the current. In order to appreciate significative changes, the device operates only in direct polarization between  $0.0[V]$  and  $1.5[V]$ . In Fig.4.39a are shown the electron and hole current at contact A with the constant mobility model, while in Fig.4.39b we switched on the Masetti model. The effect due to the dopant concentration is clearer in Fig.4.39d, where a zoom on the operation region of the diode is made (above  $0.8[V]$ ). As you can see the total current with Masetti mobility is lower and still aligned with the SDEVICE result. The parameters of the simulation are summerized in Tab.4.6.

**Figure 4.39:** Current at contact p-n in oxide - Direct polarization.

Test case	Mobility model	R/G model	$\epsilon_{Si}$	$\epsilon_{0x}$
$V_A = 0.0 \div 1.5[V]$ , $V_B = 0.0[V]$	$\mu_n = 1417$ $\mu_p = 470.5$	SRH II, Auger	11.6	3.9
$V_A = 0.0 \div 1.5[V]$ , $V_B = 0.0[V]$	Masetti	SRH II, Auger	11.6	3.9

**Table 4.6:** List of parameters.

### MOSFET n-channel/p-channel

Finally we present the results for the nMOSFET and the pMOSFET. Fig.4.40 shows the mesh (2618 verticies and 11514 elements) and the doping profile for the p-channel MOS used during these simulations: we still use a gaussian profile for the implanted regions. In order to validate the code we tested the devices in the following situations:

1.  $I_D - V_G$  characteristic at low drain bias with several mobility models;
2.  $I_D - V_G$  characteristic for different drain bias;
3.  $I_D - V_D$  characteristic in off-state (inverse polarization).

Fig.4.41 shows the results related to the first case with the nMOSFET. The on-state is reached for gate bias over 1.0[V] and the models influence the solution as expected: Fig.4.41a well explains the correct behaviour, in fact it's visible how non-constant mobilities tend to decrease the drain current value. Fig.4.41b÷4.41d confirm the good agreement with the commercial tool between different mobility models.

Similar test is performed for the pMOSFET, but considering that a p-channel usually operates for negative values of the gate bias and in order to let move the holes and appreciate a significative contribute of current, we have to apply a positive polarization on the source terminal. The results are shown in Fig.4.42: also for the pMOSFET the mobility models operate as expected (Fig.4.42a), and the agreement with SDEVICE is still good (Fig.4.42b÷4.42d).

All values and models used are summerized in Tab.4.7 for the nMOSFET and Tab.4.8 for the pMOSFET.

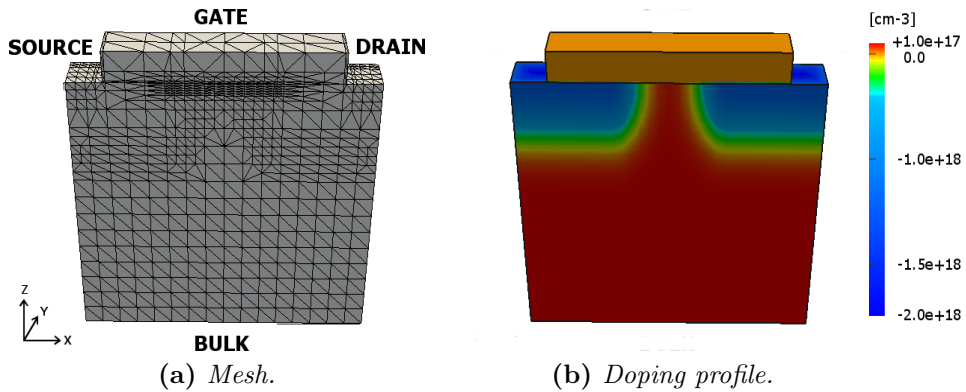
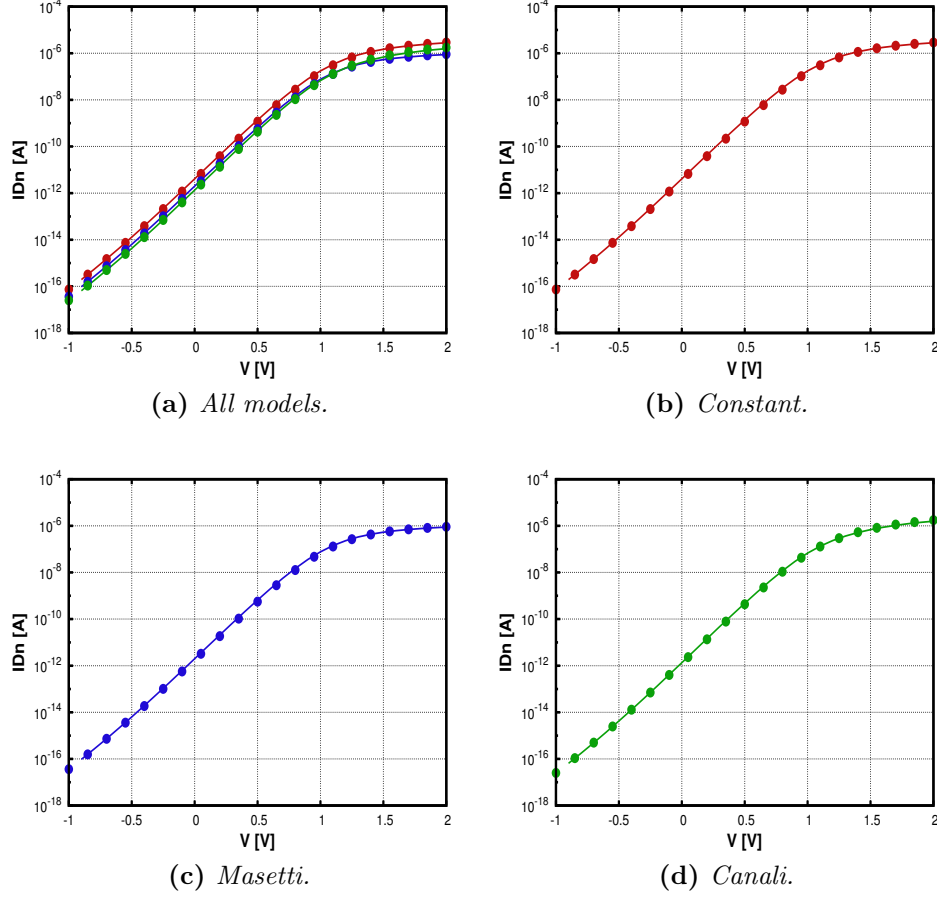
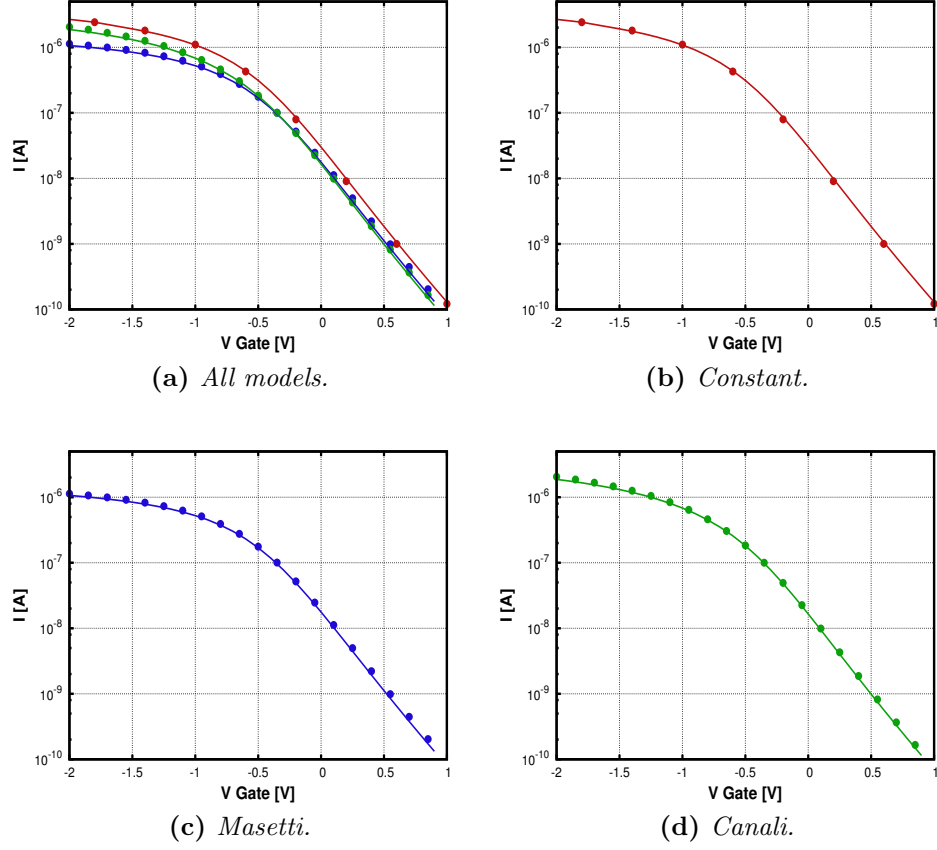


Figure 4.40: pMOSFET.

**Figure 4.41:**  $I_D - V_G$  nMOSFET characteristic - mobility models.

Test case	Mobility model	R/G model	$\epsilon_{Si}$	$\epsilon_{0x}$
$V_G = -0.5 \div 2.0[V]$ , $V_D = 0.1[V], V_S = V_B = 0.0[V]$	$\mu_n = 1417$ $\mu_p = 470.5$	SRH, Auger	11.6	3.9
$V_G = -0.5 \div 2.0[V]$ , $V_D = 0.1[V], V_S = V_B = 0.0[V]$	Masetti	SRH, Auger	11.6	3.9
$V_G = -0.5 \div 2.0[V]$ , $V_D = 0.1[V], V_S = V_B = 0.0[V]$	Canali	SRH, Auger	11.6	3.9

**Table 4.7:** List of parameters for nMOSFET.

**Figure 4.42:**  $I_S - V_G$  pMOSFET characteristic - mobility models.

Test case	Mobility model	R/G model	$\epsilon_{Si}$	$\epsilon_{0x}$
$V_G = -1.5 \div 0.5[V]$ , $V_S = 0.1[V], V_D = V_B = 0.0[V]$	$\mu_n = 1417$ $\mu_p = 470.5$	SRH, Auger	11.6	3.9
$V_G = -1.5 \div 0.5[V]$ , $V_S = 0.1[V], V_D = V_B = 0.0[V]$	Masetti	SRH, Auger	11.6	3.9
$V_G = -1.5 \div 0.5[V]$ , $V_S = 0.1[V], V_D = V_B = 0.0[V]$	Canali	SRH, Auger	11.6	3.9

**Table 4.8:** List of parameters for pMOSFET.



Fig.4.43 presents the characteristic of the nMOSFET for different values of the drain voltage. Notice that in the subthreshold region the current increases much more than the operating region: while the drain voltage increases the nMOSFET turns to the resistive behaviour. The analogous test for the pMOSFET is presented in Fig.4.44. The results are still good and notice the different operation region respect to the nMOSFET.

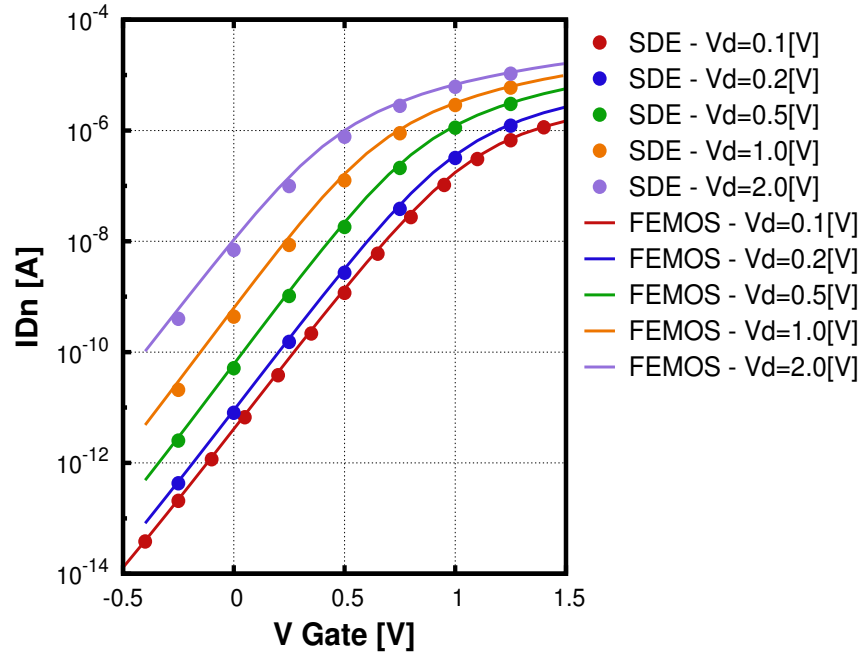
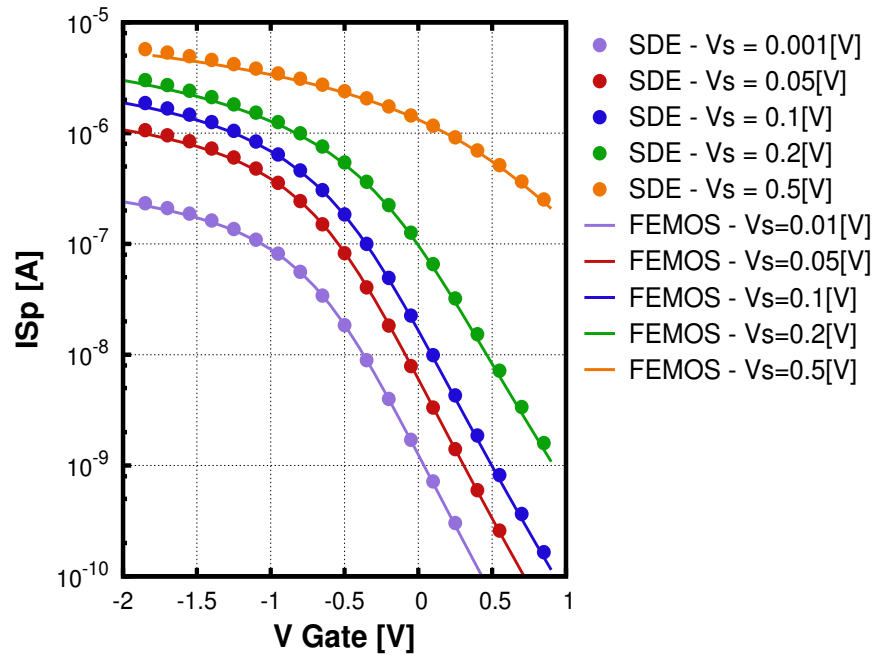
All values and models used for these simulations are summerized in 4.9 for the nMOSFET and 4.10 for the pMOSFET.

Test case	Mobility model	R/G model	$\epsilon_{Si}$	$\epsilon_{0x}$
$V_G = -0.5 \div 2.0[V]$ , $V_D = 0.1[V]$ , $V_S = V_B = 0.0[V]$	Canali	SRH, II	11.6	3.9
$V_G = -0.5 \div 2.0[V]$ , $V_D = 0.2[V]$ , $V_S = V_B = 0.0[V]$	Canali	SRH, II	11.6	3.9
$V_G = -0.5 \div 2.0[V]$ , $V_D = 0.5[V]$ , $V_S = V_B = 0.0[V]$	Canali	SRH, II	11.6	3.9
$V_G = -0.5 \div 2.0[V]$ , $V_D = 1.0[V]$ , $V_S = V_B = 0.0[V]$	Canali	SRH, II	11.6	3.9
$V_G = -0.5 \div 2.0[V]$ , $V_D = 2.0[V]$ , $V_S = V_B = 0.0[V]$	Canali	SRH, II	11.6	3.9

**Table 4.9:** List of parameters - nMOSFET.

Test case	Mobility model	R/G model	$\epsilon_{Si}$	$\epsilon_{0x}$
$V_G = -1.5 \div 0.5[V]$ , $V_S = 0.05[V]$ , $V_D = V_B = 0.0[V]$	Canali	SRH, II	11.6	3.9
$V_G = -1.5 \div 0.5[V]$ , $V_S = 0.1[V]$ , $V_D = V_B = 0.0[V]$	Canali	SRH, II	11.6	3.9
$V_G = -1.5 \div 0.5[V]$ , $V_D = 0.2[V]$ , $V_D = V_B = 0.0[V]$	Canali	SRH, II	11.6	3.9
$V_G = -1.5 \div 0.5[V]$ , $V_S = 0.5[V]$ , $V_D = V_B = 0.0[V]$	Canali	SRH, II	11.6	3.9

**Table 4.10:** List of parameters - pMOSFET.

Figure 4.43:  $I_D - V_G$  nMOSFET.Figure 4.44:  $I_S - V_G$  pMOSFET.

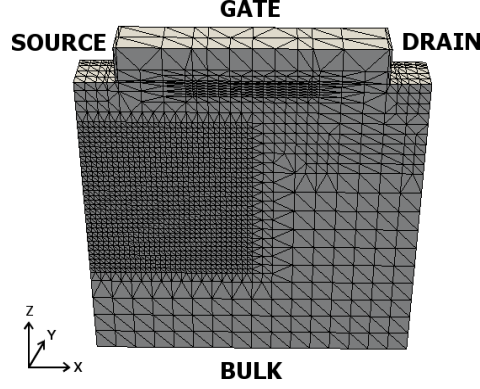


**Figure 4.45:** pMOSFET mesh.

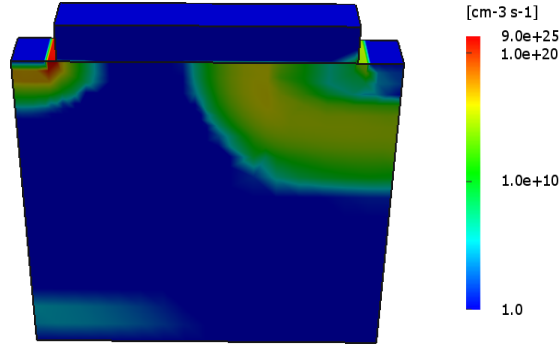
Finally we investigate the response of the devices in off-state, while increasing the drain voltage (nMOSFET) or the source voltage (pMOSFET). We are interested also to compare the effect of the impact ionization phenomenon, still computed using the Van Overstraeten - de Man model presented in section 1.2.2. In section 4.1.3 we presented what kind of problems could be affect the nMOSFET when is inverse polarized. Those considerations are still reasonable for a pMOSFET and in order to avoid possibly negative concentration, we add degrees of freedom at the source-bulk junction region. The resulting mesh is presented in Fig.4.45 (15504 verticies and 81587 elements).

Considering for a moment the nMOSFET, when all contact are grounded if we increase the drain voltage a large amount of generation is produced around the drain-bulk junction. This phenomenon is well visible in Fig.4.47, where we compare the contribution due to the Van Overstraeten - de Man model computed at  $V_D = 0.5[V]$  between FEMOS and SDEVICE. Even if the shape is quite equal the contribution seems to differ a little bit in some regions. Although this discrepancy doesn't affect the computation of the current at contact. In fact Fig.4.48 confirm the agreement with the commercial tool. Notice that under the off-state condition no channel is formed beneath the oxide layer, therefore there isn't a preferential path which electrons (or holes in the case of a pMOSFET) may follow. As a consequence carriers generated can move from both source and bulk contact.

Similar comments can be done for the pMOSFET impact ionization which is presented in Fig.4.49. Although there's a notable difference from the nMOSFET: around the source contact there is an increasing amount of generation due to the impact ionization. It's possible appreciate the conse-

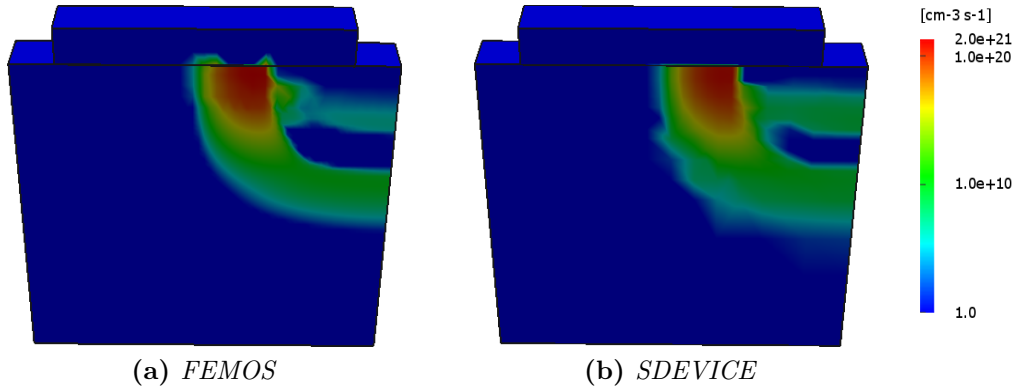
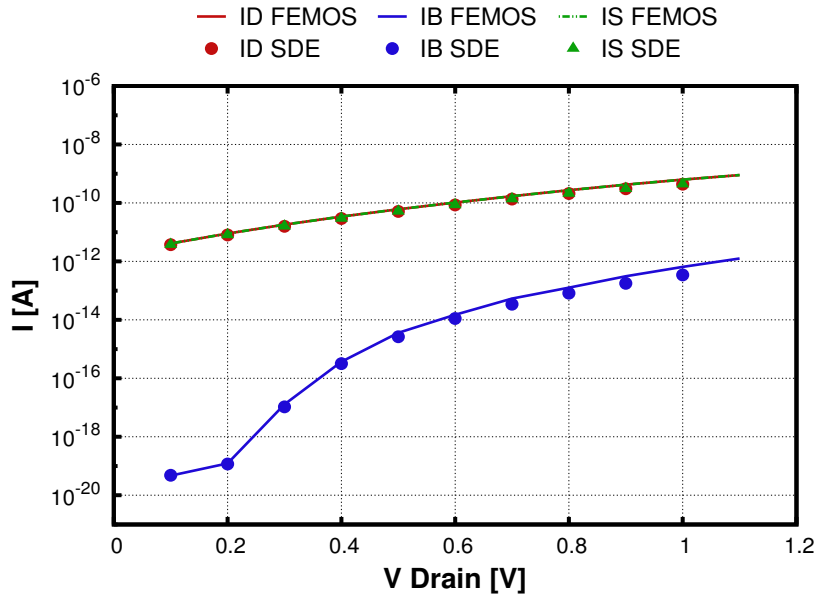
quence of this phenomenon looking at the contact current in Fig.4.50: when  $V_S > 1.0[V]$  the main current contribution flows between the source and the bulk junction rather than the source and the drain. The contribution of the impact ionization for  $V_S > 1.0[V]$  is presented in Fig.4.46.

The test case parameters are summerized in Tab.4.11 for the nMOSFET and in Tab.4.12 for the pMOSFET.

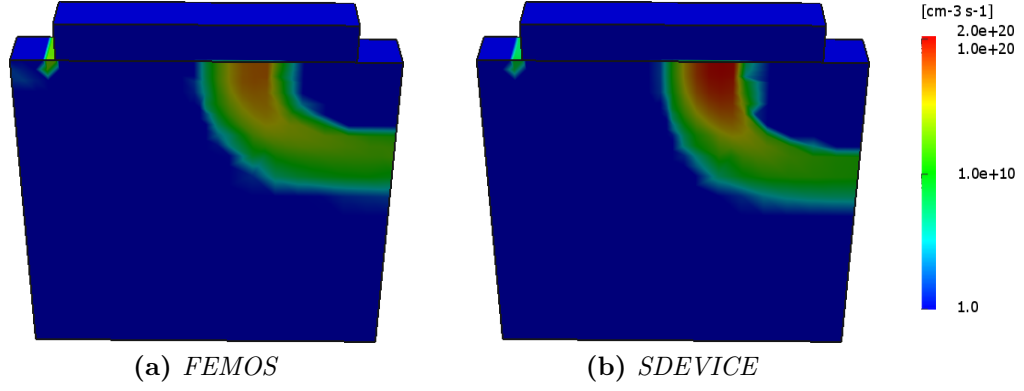
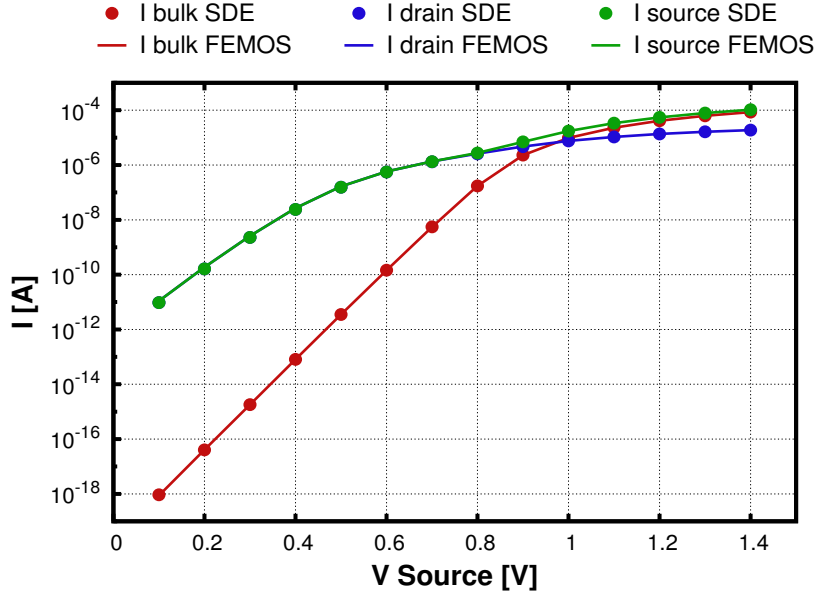


**Figure 4.46:** Contribution of the impact ionization with the Van Overstraeten - de Man model inside the pMOSFET  $V_S = 1.2[V]$ .

Test case	Mobility model	R/G model	$\epsilon_{Si}$	$\epsilon_{0x}$
$V_D = 0.0 \div 1.0[V]$ , $V_G = V_S = V_B = 0.0[V]$	$\mu_n = 1417$ $\mu_p = 470.5$	SRH Auger, II	11.6	3.9

**Table 4.11:** List of parameters - nMOSFET.**Figure 4.47:** Contribution of the impact ionization with the Van Overstraeten - de Man model inside the nMOSFET  $V_D = 0.5[V]$ .**Figure 4.48:** Inverse polarization of the nMOSFET.

Test case	Mobility model	R/G model	$\epsilon_{Si}$	$\epsilon_{0x}$
$V_S = 0.0 \div 1.5[V]$ , $V_G = V_D = V_B = 0.0[V]$	$\mu_n = 1417$ $\mu_p = 470.5$	SRH Auger, II	11.6	3.9

**Table 4.12:** List of parameters - pMOSFET.**Figure 4.49:** Contribution of the impact ionization with the Van Overstraeten - de Man model inside the pMOSFET  $V_S = 0.5[V]$ .**Figure 4.50:** Inverse polarization of the pMOSFET.

## Chapter 5

# The current calculation problem

In many physical and engineering problems the real interesting variable of the conservation law is the flux in the domain or on specific surfaces and boundaries. The study of micro and nano electronics devices doesn't except this observation, in fact most of all models are oriented to obtain a satisfactory description of the current density. We know that the primal and not mixed formulation for the continuity equation doesn't resolved the flux density. The consequence of this fact is a binding post-processing of the quantities computed in order to reconstruct the current density of electrons and holes. It's evident which this part covers a lead role in the device simulation: as we are satisfied of the impressive results of the finite element scheme, it will be reather regrettable to lost the accuracy of our simulation during the computation of the current density. About this question many academics propose different solutions and the relative literature is boundless.

In section 1.1.4 we saw that there exist three way to represent the current density inside a semiconductor device. However each one of these formulas is affected by several numerical issues. We'll investigate this features in order to propose appropriate treatments of the current density computation.

Easily we can exlude the *Slotboom equation* from our consideration. As we already highlighted this formula has relevant properties which make really simple the wellposedness of the continuity equation, however the exponential dependency by the factor  $\varphi/V_{th}$  causes unavoidable numerical instability. Therefore we don't consider at priori equation (1.36) and (1.37) as a way to compute the current density.

We'll center our analysis on the *Drif-Diffusion formula* and the *Quasi Fermi formula*. Finally we'll present two revisions of these expressions in order to fix the numerical weakness.

## 5.1 Standard approaches

Let us introduce some useful notations:  $k$  subscript refers to a quantity defined on elements, while  $h$  subscript refers to a quantity defined on vertices. As we used the discrete space  $X_h^1$  the solutions  $\varphi_h$ ,  $n_h$  and  $p_h$  are linear continuous functions. If we refer to (1.30), (1.31), (1.32) and (1.33) it's clear that in order to compute  $\mathbf{J}_n$  and  $\mathbf{J}_p$  a numerical derivative on the solutions must be done. Therefore the current densities are constant element piecewise functions ( $\mathbf{J}_{n,k}, \mathbf{J}_{p,k} \in [X_h^0]^3$ ). Thus the current density lives on a different discretized space, if we want combine the quantities, we have to compute appropriate projection of the solutions

$$n_k := \langle n_h \rangle \quad (5.1)$$

For example this operation could be the standard integral average or the harmonic average.

Another important issue is the computation of the derivatives. For this purpose we implemented a numerical derivation based on the Lagrange polynomial interpolator of the first order

$$\nabla n \simeq \nabla(\Pi_h^1 n) = \sum_{i=1}^{N_h} n_i \nabla \psi_i = \nabla_k n_h \quad (5.2)$$

Notice that the quantity so calculated lives on the appropriate space. Now we can discretize equations (1.30), (1.31), (1.32) and (1.33) as follows

$$\mathbf{J}_n^k = -q \langle n \rangle \mu_n \nabla \varphi + q D_n \langle n \rangle \nabla n \quad (5.3)$$

$$\mathbf{J}_p^k = -q \langle p \rangle \mu_p \nabla \varphi - q D_p \langle p \rangle \nabla p \quad (5.4)$$

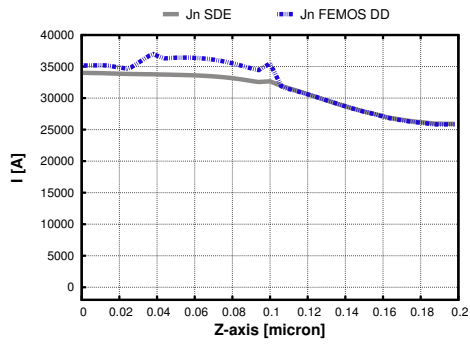
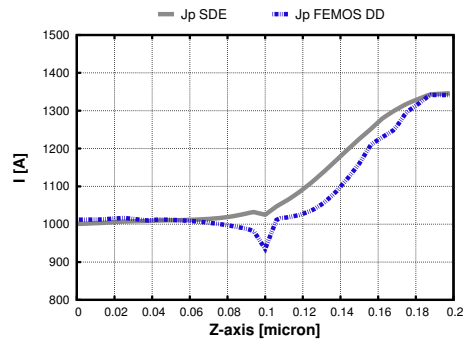
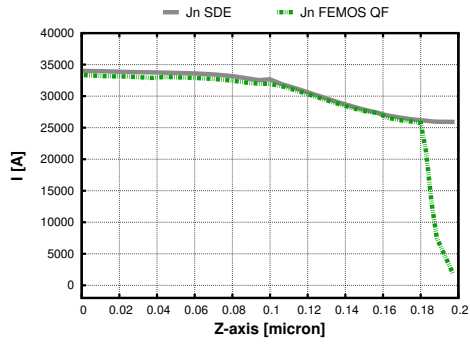
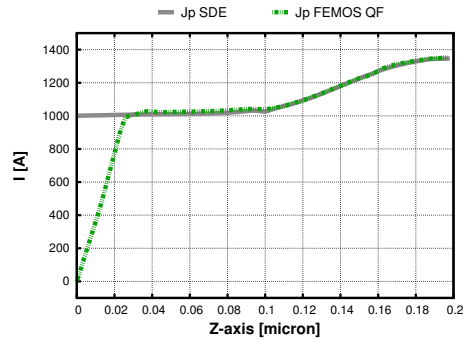
$$\mathbf{J}_n^k = -q \langle n \rangle \mu_n \nabla \varphi_n \quad (5.5)$$

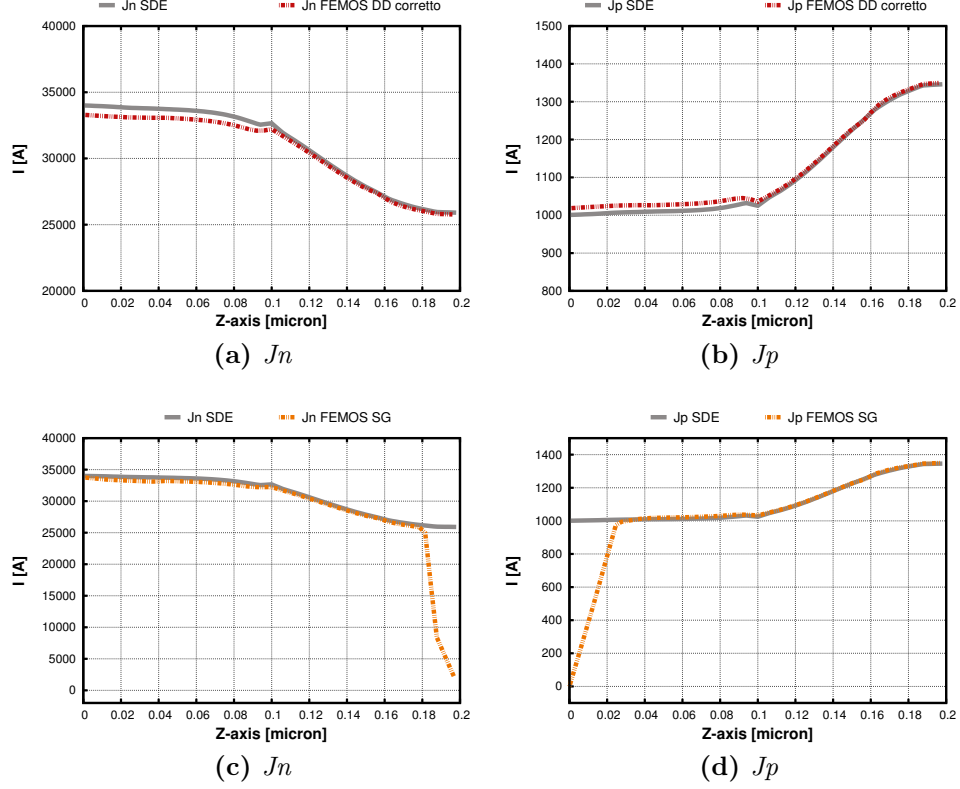
$$\mathbf{J}_p^k = -q \langle p \rangle \mu_p \nabla \varphi_p \quad (5.6)$$

Risultati:

- Problema del compenso fra apporto di drif e diffusion, infatti zona critica quando questi due contributi diventano rilevanti...instability
- Formula molto stabile tuttavia problemi agli strati limiti delle concentrazioni (problema condizione di contatto differenti comportamenti a seconda della media utilizzata)



(a)  $J_n$ (b)  $J_p$ (c)  $J_n$ (d)  $J_p$



## 5.2 Modified approaches

Luckily there's some *main stone* which offers ever a good start point whence achieve new results. Probably the most known and recognized by the inherent literature is the *Sharfetter-Gummel formula*.

## 5.3 Scharfetter-Gummel formula

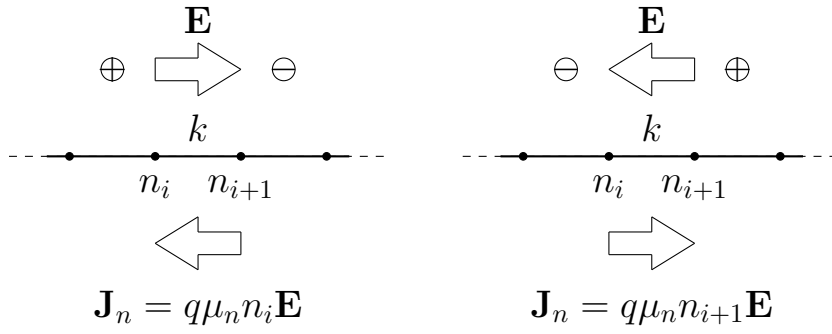
Consider the resolution of the continuity equation along a monodimensional domain. For the sake of simplicity we contemplate a uniform partition (this hypotesis is not necessary for a more generic analysis). Moreover on every nodes is defined the electrostatic potential  $\varphi$ , and on every elements the relative electrostatic field  $\mathbf{E}$ . In order to avoid redundant considerations and calculuses, we proceed with our analysis considering only the current density of electrons ( $\mathbf{J}_n$ ).

In 1969 D. Scharfetter and H.K. Gummel (two scientists of Bell Labs), introduced a formula to compute the current density in this case, given  $\varphi$  and

the density solution ( $n$ ) on every nodes. This innovative approach led for the twenty years to follow every simulation which contemplates electric-devices.

We know that the constitutive law is composed by a drift component, which depends on the electric field, and a diffusion component, which depends on the variation of the carrier density. Consider a generic element  $K$ , we define the drop in voltage  $\Delta\varphi^k = \varphi_{i+1} - \varphi_i$ . There are three possible situations which are well explain in the picture:

- $\Delta\varphi \gg 0$ , mainly drift component from right to left
- $\Delta\varphi \ll 0$ , mainly drift component from left to right
- $\Delta\varphi \simeq 0$ , mainly diffusion component



With the *Sharfetter – Gummel* formula it's possible taking into account every of these situations and solve boundary layer problems which occurs often in presence of strong drift component contribute.

$$J_n^k = q \frac{D_n}{h} \left[ n_{i+1} \mathcal{B} \left( \frac{\Delta\varphi^k}{V_{th}} \right) - n_i \mathcal{B} \left( -\frac{\Delta\varphi^k}{V_{th}} \right) \right] \quad (5.7)$$

In the latter case ( $\Delta\varphi = 0$ ) the formula became:

$$J_n^k = q D_n \frac{n_{i+1} - n_i}{h} \quad (5.8)$$

which is the correct approximation of the current density using  $\mathbb{P}_1$  basis.

Moreover many mathematics discover important properties about this method **questa parte la vorrei fare meglio**. These changes in the direction of the electric field lead to boundary layer problems. It's not possible afford these situations with a simply upwinding scheme ...

## 5.4 Extension for the 3D case

The extension of this formula for the 3D case is not trivial. We show the method for the computation of the current density of electrons (the extension for the current density of holes is quite similar). We remark the quasi fermi formula for current density:

$$\mathbf{J}_n = -q\mu_n n \nabla \varphi_n \quad (5.9)$$

where  $\varphi_n$  is the quasi fermi potential level. Let us write (5.9) in function of potential and in a canonic form:

$$\mathbf{J}_n \frac{\exp\left(\frac{\varphi_n - \varphi}{V_{th}}\right)}{q\mu_n n_i} + \nabla \varphi_n = 0 \quad (5.10)$$

We consider  $\mathbf{J}_n \in [L^2(\Omega)]^3$  and  $\varphi_n, \varphi \in H^1(\Omega)$ . We are able to multiply (5.10) with a generic function  $\mathbf{q} \in [L^2(\Omega)]^3$  and then integrate over the domain  $\Omega$ :

$$\int_{\Omega} \frac{\exp\left(\frac{\varphi_n - \varphi}{V_{th}}\right)}{q\mu_n n_i} \mathbf{J}_n \cdot \mathbf{q} \, d\Omega + \int_{\Omega} \nabla \varphi_n \cdot \mathbf{q} \, d\Omega = 0 \quad (5.11)$$

We proceed taking the usual discrete space of the constant elementwise functions:

$$V_h = \{w \in L^2(\Omega) : w|_K \in \mathbb{P}_0 \forall K \in \tau_h\} \quad (5.12)$$

Now the discrete quantities are  $\mathbf{J}_n^h \in [V_h]^3$  and  $\nabla \varphi_n^h \in V_h$ . We desire produce a system of equation on every elements for the three components of  $\mathbf{J}_n$ , this is possible with a smart choice of the test function  $\mathbf{q}_h \in [V_h]^3$ :

$$\mathbf{q}_{1,2,3}^h = \left\{ \begin{bmatrix} 1 \\ 0 \\ 0 \end{bmatrix} \begin{bmatrix} 0 \\ 1 \\ 0 \end{bmatrix} \begin{bmatrix} 0 \\ 0 \\ 1 \end{bmatrix} \right\} \quad (5.13)$$

From (5.11) we obtain the sequent system of equations defined for every element of the mesh:

$$\int_K \frac{\exp\left(\frac{\varphi_n - \varphi}{V_{th}}\right)}{q\mu_n n_i} \mathbf{J}_n^h \cdot \mathbf{q}_i^h \, dK + \int_K \nabla \varphi_n^h \cdot \mathbf{q}_i^h \, dK = 0 \quad \forall i = 1, 2, 3 \quad (5.14)$$

Operating the intagration we obtain the sequent formula for the current density components:

$$[\mathbf{J}_n]_i = -\mathbb{H}_K \left( q\mu_n n_i \exp \left( \frac{\varphi - \varphi_n}{V_{th}} \right) \right) \frac{\partial \varphi_n^h}{\partial x_i} \quad i = 1 \dots d \quad \forall K \in \tau_h \quad (5.15)$$

where  $\mathbb{H}_K(f)$  is the armonic average on the elment  $K$  of the function  $f$ .

Although resolve the armonic average with a comlete 3D integration may be expensive in calculation time and propably not necessary. One approximation of this integral would be pass from a 3D integration to 1D integration along one edge of the element  $K$ .

$$\left( \frac{\int_K f^{-1} dK}{|K|} \right)^{-1} \simeq \left( \frac{\int_{e^*} f^{-1} de}{|e^*|} \right)^{-1} \quad (5.16)$$

The approximation (5.16) is valid if we consider the correct edge.

Consider a quantity defined on the verteces:

$$\Phi := \varphi - \varphi_n \quad (5.17)$$

which is the difference between the electrostatic potential and the quasi fermi potential level. Now for every element consider two vertices:  $\mathbf{x}_m$  s.t.  $\Phi(\mathbf{x}_m) = \Phi_m := \min_K(\Phi)$  and  $\mathbf{x}_M$  s.t.  $\Phi(\mathbf{x}_M) = \Phi_M := \max_K(\Phi)$ . Obviously it exists only one edge which connects these two points and on this one we perform the 1D integration (5.16). First of all as we reduce the dimension is feasible to represent  $\sigma(\mathbf{x})$  in a easier mode as follows:

$$\sigma_n(s) = q\mu_n n_i \exp \left( \Phi_m + (\Phi_M - \Phi_m) \frac{s - s_m}{|e^*|} \right) \quad (5.18)$$

where  $s \in [s_m, s_M]$  is the parameter refered to the edge  $e^*$  s.t.  $\sigma_n(s_m) = \sigma_n(\mathbf{x}_m)$  and  $\sigma_n(s_M) = \sigma_n(\mathbf{x}_M)$ . We can easily resolve (5.16) with the substitution of variable:

$$\eta := \frac{s - s_m}{|e^*|}$$

this lead us to the sequent steps of integration:

$$\begin{aligned} \int_{e^*} \sigma_n^{-1} de &= |e^*| \int_0^1 \frac{\exp(-\Phi_m - (\Phi_M - \Phi_m)\eta)}{q\mu_n n_i} d\eta \\ &= |e^*| \frac{\exp(-\Phi_m)}{q\mu_n n_i} \frac{\exp(\Phi_m - \Phi_M) - 1}{\Phi_m - \Phi_M} \\ &= |e^*| \frac{\exp(-\Phi_m)}{q\mu_n n_i} \frac{1}{\mathbf{B}(\Phi_m - \Phi_M)} \end{aligned}$$

finally we obtain:

$$\int_K \sigma_n^{-1} dK \simeq q\mu_n n_i \exp(\Phi_m) \mathbf{B}(\Phi_m - \Phi_M) \quad (5.19)$$

Similar results may be obtained repeating the integration and considering  $s_M$  as start point:

$$\int_K \sigma_n^{-1} dK \simeq q\mu_n n_i \exp(\Phi_M) \mathbf{B}(\Phi_M - \Phi_m) \quad (5.20)$$

Numerical results (*qua sarebbe carino fare un po' di test con una parte o l'altra della formula per mettere in crisi*) shows that the best choice is e linea combination of these appozimations as follows:

$$\mathbf{J}_n^K = -q\mu_n \left[ \frac{n_{min} \mathbf{B}(-\Delta\Phi_{max}) + n_{max} \mathbf{B}(\Delta\Phi_{max})}{2} \right] \nabla \varphi_n^h \quad (5.21)$$

This approach is the natrual extension of the *Sharfetter – Gummel* formula for the 1D case, indeed it's possible demonstrate the equivalence assuming a monodimensionale domain.

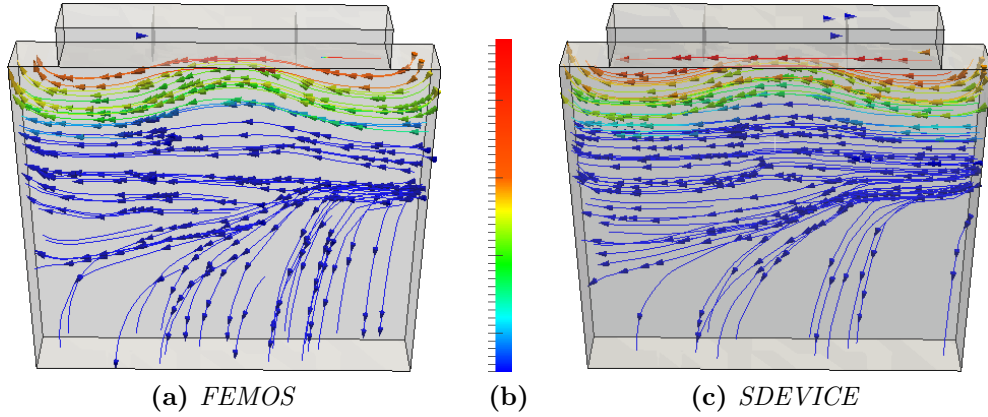


**Figure 5.1:** Electron current density  $V_{gate} = 2.0$  [V].

# Conclusions and future work

- Metodo SG vantaggi a livello computazionale, estensione naturale 3D del metodo SG 1D
- Metodo DD corretto risolve i problemi di contatto, più soggetto ad instabilità numeriche, rispetta una proprietà importante in maniera forte
- Possibilità di utilizzare questi metodi come nuovo schema di discretizzazione: problemi al contatto per il metodo SG (problema della media armonica con metodo misto). Per quanto riguarda il DD corretto bisogna pensarci.





# Bibliography

- [BCC98] R. E. Bank, W. Coughran, and L. C. Cowsar. The finite volume sharfetter-gummel method for steady convection diffusion equations. *Computing and Visualization in Science*, 1:123–136, 1998.
- [Deu74] P. Deuffhard. A modified newton method for the solution of ill-conditioned system of nonlinear equations with application to multiple shooting. *Numer. Math*, 22:289–315, 1974.
- [DF05] Carlo De Falco. *Quantum Corrected Drift-Diffusion Models and Numerical Simulation of Nanoscale Semiconductor Devices*. Dottorato di ricerca in matematica e statistica per le scienze computazionali, A.A. 2004/2005.
- [GS74] R. Gusmeroli and A. S. Spinelli. Accurate boundary integrals calculation in semiconductor device simulation. *Numer. Math*, 22:289–315, 1974.
- [HEML00] Thomas J.R. Hughes, Gerald Engel, Luca Mazzei, and Mats G. Larson. The continuous galerkin method is locally conservative. *Journal of Computational Physics*, 163:467–488, 2000.
- [IE83] Babuška I. and Osborn J. E. Generalized finite element methods: Their performance and their relation to mixed methods. *Numer. Anal.*, 20:510–536, 1983.
- [PC98] M. Putti and C. Cordes. Finite element approximation of the diffusion operator on tetrahedra. *Society for Industrial and Applied Mathematics*, 19:1154–1168, 1998.
- [PTVF07] William H. Press, Saul A. Teukolsky, William T. Vetterling, and Brian P. Flannery. *Numerical Recipes, The Art of Scientific Computing*. Cambridge University Press, New York, 2007.

- [Qua08] Alfio Quarteroni. *Modellistica Numerica per Problemi Differenziali*. Springer Italia, Milan, 2008.
- [Sal10] Sandro Salsa. *Equazioni a Derivate Parziali, metodi, modelli e applicazioni*. Springer Italia, Milan, 2010.
- [Sde13] *Sentaurus Device User Guide*. Synopsis Inc., 2013.
- [XZ99] Jinchao Xu and Ludmil Zikatanov. A monotone finite element scheme for convection-diffusion equations. *Mathematics of Computation*, 68:1429–1446, 1999.
- [YT09] Taur Yuan and H. Ning Tak. *Fundamentals of Modern VLSI Devices*. Cambridge University Press, 2009.

# Ringraziamenti